THÈSE

présentée pour obtenir le titre de

DOCTEUR DE L'ÉCOLE CENTRALE DE LYON

École Doctorale Mécanique, Énergétique, Génie Civil et Acoustique

spécialité

MÉCANIQUE

Improved vortex method for LES inflow generation and applications to channel and flat-plate flows

---

Soutenue le 12 December 2016 à l'École Centrale de Lyon

par

Baolin XIE

Devant le jury composé de :

F. BATAILLE	Université de Perpignan	Rapporteur
L.P. LU	Université de Beihang	Rapporteur
J.P. Bertoglio	LMFA, CNRS	Examinateur
A. GIAUQUE	LMFA, École Centrale de Lyon	Examinateur
L. FANG	Université de Beihang	Examinateur
L. SHAO	LMFA, CNRS	Directeur

Laboratoire de Mécanique des Fluides et d'Acoustique - UMR 5509

Acknowledgements

My sincere thanks goes to LIU YiXi for supporting me and sharing the passions, the happiness and the life with me. I love you more than i can say, my dear.

Last but not the least, I would like to thank my family: my parents, my sisters and brothers-in-law, my nieces for continuously supporting me spiritually throughout my research and my life in general. You are my substantial backup forever.

Abstract

Large eddy simulation is becoming an important numerical tool in industry recently. Resolving large scale turbulent motions directly, LES is capable to compute the aeroacoustic noise generated by the airfoil or to precisely capture the corner separation in a linear compressor cascade. The main challenge to perform a LES calculation is to prescribe a realistic unsteady inflow field. For hybrid RANS/LES approaches, inflow conditions for downstream LES region must be generated from the upstream RANS solutions.

There exist several methods to generate inflow conditions for LES. They can mainly be divided into two categories: 1) Precursor simulation; 2) Synthetic turbulence methods. Precursor simulation requires to run a separate calculation to generate a turbulent flow or a database to feed the main computation. This kind of methods can generate high quality turbulence, however it requires heavy extra computing load. Synthetic turbulence methods consist in generating a fluctuating velocity field, and within a short "adaptation distance", the field get fully developed. So main goal of synthetic turbulence methods is to decrease the required adaptation distance.

The vortex method which is a synthetic turbulence method is presented and improved here. Parameters of the improved vortex method are optimized systematically with a series of calculations in this thesis. Applications on channel and flat-plate flows show that the improved vortex method is effective in generating the LES inflow conditions. The adaptation distance required for turbulence recovery is about 6 times the half channel height for channel flow, and 21 times the boundary-layer thickness (at the inlet of vortex) for flat-plate flow. The velocity-derivative skewness is used to qualify the generated turbulence, and is introduced as a new criterion of LES calculation.

Key words: vortex method, LES, RANS, hybrid RANS/LES, inflow condition, channel flow, boundary layer, skewness.

Résumé

La simulation des grandes échelles (SGE ou LES pour large eddy simulation)
commence à être très utilisée dans l'industrie. Par résolution directe des struc-
tures turbulents de grande tailles, le calcul LES est capable de calculer le bruit
générée par la voilure ou de prédire avec précision le décollement de coin dans
une configuration très simplifiée du compresseur. L'un des problèmes les plus
importants pour effectuer un calcul LES est de fournir des conditions d'entrée
avec des champs turbulents.

Pour une approche hybride RANS/LES (RANS pour Reynolds Averaged
Navier-Stokes), les conditions d'entrée turbulentes pour un calcul LES sont générées
à l'aide des solutions fournies par le calcul RANS en amont. Il existe plusieurs
méthodes pour générer les conditions d'entrée pour LES. Elles peuvent princi-
palement être classées en deux catégories : 1) simulation avec pré-calcul ; 2)
la méthode de turbulence synthétique. La simulation avec pré-calcul consiste
à effectuer un calcul LES indépendant pour générer un champ turbulent comme
conditions d'entrée pour alimenter le calcul principal. Cette méthode peut obtenir
des turbulences de haute qualité, mais elle augmente considérablement le temps
de calcul et le stockage des données. Le champ turbulent généré par la méthode
de turbulence synthétique exige une "distance de adaptation", pendante laque-
lle le champ turbulent devient pleinement développée. L'objectif principal pour
améliorer ce genre de méthodes est donc de diminuer cette distance nécessaire.

Dans cette thèse, la méthode de vortex, qui est une approche de turbulence
synthétique, est présentée et améliorée . A travers des expérience numériques, les
paramètres de la méthode de vortex améliorée sont systématiquement optimisées.
L'application à l'écoulement en canal plan et à couche limite en plaque plane,
montrent que la méthode de vortex améliorée génère de manière efficace pour
fournir des conditions d'entrée pour LES. Dans le cas de l'écoulement en canal
plan, la distance d'adaptation nécessaire pour le rétablissement de la turbulence
est de environ 6 fois la demi-hauteur du canal. Pour le cas de l'écoulement en
plaque plane, cette distance est environ 21 fois l'épaisseur de la couche limite.
Enfin, dans le but de qualifier la turbulence obtenue par des calculs LES, nous

utilisons les coefficients de dissymétrie des dérivées des fluctuations de vitesse, et, nous les introduisons comme un nouveau critère pour la qualité de LES.

Mots clés: méthode de vortex, LES, RANS, hybride RANS/LES, condition d'entrée, canal plan, couche limite, dissymétrie.

Contents

Contents

Nomenclature

Roman Symbols

$\overline{U}$ bulk velocity, $\overline{U} \equiv \frac{1}{h}\int_0^h \langle U \rangle dy$

C_1 coefficient of vortex radius

C_2 coefficient of vortex circulation

C_3 coefficient of vortex lifetime

C_4 coefficient of enhanced random walk

C_5 coefficient of stochastic walk (model coefficient of Langevin equation)

C_D drag coefficient

c_f friction coefficient

D_{LLL} the third-order longitudinal velocity structure function

D_{LL} the second-order longitudinal velocity structure function

$E(\kappa)$ Energy spectrum

G filter function

H Heaviside step function

h half channel height

k turbulent kinetic energy, $k = \frac{1}{2}\langle u_i'^2 \rangle$

L energy-containing scale, $L \sim \frac{k^{1.5}}{\epsilon}$

l_d dissipation scale

M Mach number

P static pressure

R_{ij} two-point correlation function

Re Reynolds number

Re_λ Taylor scale Reynolds number

Re_τ friction Reynolds number

Re_θ Reynolds number (based on momentum thickness)

Re_x Reynolds number (based on axial distance)

Re_{local} local Reynolds number

S velocity-derivative skewness

S_u velocity-derivative skewness along the streamwise direction

s_{ij} rate of strain, $s_{ij} = \frac{1}{2}\left(\frac{\partial u_i}{\partial x_j} + \frac{\partial u_j}{\partial x_i}\right)$

S_{st} source term

$T(\kappa)$ transfer spectrum

U_0 centerline velocity

U_d displacement velocity of vortice

u_x, u_y, u_z velocity components in x, y, z directions, respectively

u_τ friction velocity

x, y, z Cartesian coordinates

Greek Symbols

Nomenclature

$\boldsymbol{\kappa}$ wavenumber vector

Δ grid spacing

δ boundary-layer thickness, value of y where $\langle U(x,y)\rangle = 0.99U_\infty(x)$

δ^* displacement thickness, $\delta^*(x) \equiv \int_0^\infty (1 - \frac{\langle U\rangle}{U_\infty})dy$

δ_{ij} Kronecker delta

ϵ dissipation rate, $\epsilon = \nu\langle \frac{\partial u_i}{\partial x_j}\frac{\partial u_i}{\partial x_j} + \frac{\partial u_i}{\partial x_j}\frac{\partial u_j}{\partial x_i}\rangle$

η Kolmogorov scale

Γ circulation of vortex

γ heat capacity ratio

κ wavenumber

κ_c cutoff wavenumber

λ step length of enhanced random walk (B.L. Xie)

λ_0 step length of random walk (E. Sergent)

μ dynamic viscosity

ν_t turbulent or eddy viscosity

ν kinematic viscosity

ω specific dissipation rate, $\omega = \frac{\epsilon}{C_\mu k}$

$\overline{\tau}_{ij}$ subgrid scale stress, $\overline{\tau}_{ij} = \overline{u_i u_j} - \overline{u}_i \overline{u}_j$

π constant, ratio of a circle's circumference to its diameter, $\pi \simeq 3.14$

ρ density

σ radius of vortex

τ lifetime of vortex

θ momentum thickness, $\theta(x) \equiv \int_0^\infty \frac{\langle U \rangle}{U_\infty}(1 - \frac{\langle U \rangle}{U_\infty})dy$

ξ spatial distribution of vortex

Superscripts

$\overline{q}$ filtered quantity

q'' fluctuating quantity after filter-operation

q' fluctuating quantity after ensemble average

q^+ quantity in wall unit

Subscripts

q_∞ free-stream quantity

q_{rms} root-mean-square of a quantity

Other Symbols

$\langle q \rangle$ ensemble averaged quantity

$\langle u_i' u_j' \rangle$ Reynolds stress

Acronyms

2D   Two-Dimensional

3D   Three-Dimensional

CFD   Computational Fluid Dynamics

CFL   Courant–Friedrichs–Lewy (condition)

CLPP   Couche Limite Plaque Plane [Fr] (boundary layer flat-plate)

CLVM   Couche Limite [Fr] Vortex Method

CPVM   Canal Plan [Fr] Vortex Method (canal plan: channel)

DNS   Direct Numerical Simulation

ERW enhanced random walk

IVM Improved Vortex Method

LES Large-Eddy Simulation

N-S Navier-Stokes

PO Parameter Optimization

RANS Reynolds-Averaged Navier-Stokes

RMS Root Mean Square

SEM Synthetic Eddy Method

SGS subgrid-scale

SISM Shear-Improved Smagorinsky Model

SW stochastic walk

WALE Wall-Adapting Local Eddy-viscosity

ZDES Zonal Detached Eddy Simulation

Introduction

Turbulence, being one of the most fascinating, difficult and important problems in classical physics, is frighteningly hard to understand. It is related not only to industrial use but also to our everyday life. In fact, most external and internal fluid flows we meet are turbulent. For example, flows in blood vessels or flows around vehicles, aeroplanes and buildings. Also, the flows in compressors, combustion chambers and gas turbines are highly turbulent. Hence, the research of turbulence is of great importance in meteorology, aeronautics, medicine and other industrial domains. There is no yet an exact definition of turbulence, but it has several well known characteristics:

1. irregular, chaotic, may seem to be random.

2. three-dimensional, rotational and unsteady.

3. has a large range of length and time scales.

4. diffusive.

5. dissipative. Turbulent kinetic energy transfers from large-scale eddies to small-scale eddies and finally dissipates at the smallest scale eddies.

The problem of turbulence attracts our attentions from very early days, with sketches of wild water flows made by Leonardo da Vinci [Gelb, 2009] and starry night drawn by Vincent van Gogh, as shown in Fig. 1. Early attempts to study the turbulence [Tennekes and Lumley, 1972][Lumley et al., 2007] are through experimental (e.g., experiments of Reynolds [1883]) and theoretical ways (e.g., Kolmogorov theory [Kraichnan, 1964]), which begins from the 19th century, but

Figure 1: A visualization of a hidden regularity of turbulence through Vincent van Gogh's Starry Night

until now, the problem of turbulence is not yet totally understood. The Navier-Stokes equations are the governing equations of fluid flows no matter they are laminar or turbulent. They can properly describe the behaviour of fluids and the turbulent phenomena. However, the analytical solutions of Navier-Stokes equations are limited to flows with very simple geometry and low Reynolds number.

Numerical simulations are more practicable and effective than experiments from some points of view [Rogallo and Moin, 1984]. They provide rich information of the turbulent flow field. Thanks to the great development of computer techniques in the 1970s and 1980s, it became realistic to investigate turbulence by numerically resolving the Navier-Stokes equations [Johnson et al., 2005]. But again the numerical solutions are limited to low Reynolds number turbulent flows as it demands significant computer power. To make a compromise, turbulence modelling is introduced to study turbulent flows at high Reynolds numbers and with more complex geometries.

There are three main approaches for resolving the Navier-Stokes equations: Direct Numerical Simulation (DNS), Large-Eddy Simulation (LES) and Reynolds-Averaged Navier-Stokes (RANS) method. DNS [Moin and Mahesh, 1998] aims
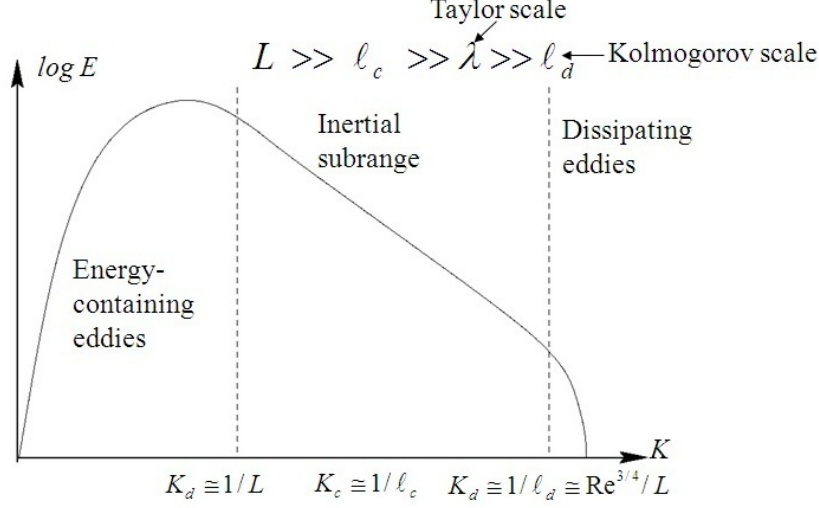
Figure 2: Energy cascade of Kolmogorov spectrum

at resolving the Navier-Stokes equations directly. From a view of energy cascade, as shown in Fig. 2, it directly simulates turbulent motions from the largest scales (energy-containing scale L, based on flow domain geometry) to the smallest scales (dissipation scale l_d or Kolmogorov scale η). Thus the computational costs are immense. It is proportional to $Re_L^{9/4}$, where Re_L is the characteristic Reynolds number. This prevents from using DNS for complex flows. To satisfy industrial needs, RANS methods [Spalart, 2000][Alfonsi, 2009] have been developed. They consist in resolving averaged Navier-Stokes equations which are closed by related turbulence model. The disadvantage is that RANS does not provide unsteady information about the flow field. An alternative is large-eddy simulation [Sagaut, 2006]. Different from DNS, turbulent motions from the largest scales until the scales of inertial subrange are directly resolved by LES [Piomelli and Chasnov, 1996]. The effect of small scale (dissipation range and part of inertial range) motions, which have a universal character according to Kolmogorov's theory [Kolmogorov, 1941], is modelled by subgrid-scale (SGS) model. Comparisons of these three different CFD methods, as can be seen in Fig. 3, are summarized as follows:

1. DNS does not need any modelling. It directly resolves all scales of turbulent motions and demands very fine spatial and temporal resolution. This results
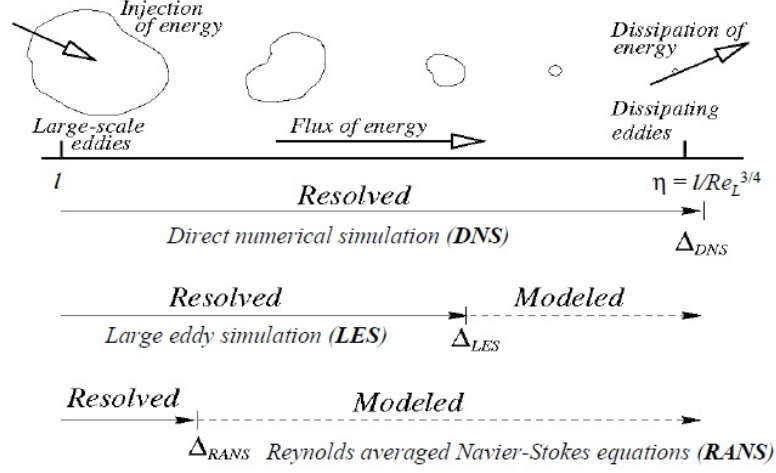
Figure 3: Comparison of DNS, LES and RANS

in huge computational costs ($\propto Re_L^{9/4}$).

2. RANS solves the averaged Navier-Stokes equations. The Reynolds stresses are modelled. It is much cheaper but cannot capture unsteady turbulent characteristics.

3. LES directly resolves large-scale turbulent motions. Small-scale motions are modelled. In this way, industrial needs could be satisfied and computational costs are reduced.

This thesis focus on large-eddy simulation and hybrid RANS-LES [Sagaut et al., 2013][Hamba, 2003]. Main work consists in studying LES inflow generation [Sagaut et al., 2003][Tabor and Baba-Ahmadi, 2010][Keating et al., 2004]. In a hybrid RANS-LES case [Mathey, 2008], one open issue is generating time dependent fluctuations from an upstream RANS solution for downstream LES. In LES, large turbulent scales are directly resolved. The scales are at least comparable to the grid scales, and subgrid scale motions are filtered out and modelled. Turbulent motions are always stochastic, spatially and temporally correlated. The unsteady turbulent motions cannot be obtained by simply imposing some kind of random fluctuations at inlet. When they are not well prescribed, LES is

known to result in dramatic errors: turbulence is badly predicted, and may lead to significant errors in the mean field. Therefore reasonable inflow conditions are of great importance for LES. Usually, requirements of LES inflow conditions are as follows:

1. Being qualified by fully developed flow database (mean velocity, Reynolds stress, skewness, spectrum, etc).

2. Turbulent fluctuations must be spatially and temporally correlated.

3. Inflow generation methods should be easy to implement and cost-effective.

There exists several methods to generate the inflow conditions for LES. They can be divided into two categories:

1. Precursor simulation. This kind of methods requires a separate calculation to generate a turbulent flow field or a database to feed the main computation at the inlet.

2. Synthetic turbulence methods. This kind of methods aims at synthesizing turbulent fluctuations according to some constraints, such as a given turbulent kinetic energy spectrum, or mean profiles of kinetic energy and dissipation rate.

Precursor simulation [Liu and Pletcher, 2006][Morgan et al., 2011] can generate high quality turbulence, but they require heavy extra computing loads. Synthetic methods [Mathey et al., 2006][Jarrin et al., 2009][Benhamadouche et al., 2006][Pamies et al., 2009] aim at obtaining a well-behaved turbulence within a short "adaptation distance". Usually, synthetic turbulence is not exact the turbulence observed in fully developed flows. It lacks spatial or temporal coherent characteristics, thus it requires an adaptation distance to become fully developed.

Among all the synthetic methods, the simplest one is to introduce white-noise type fluctuations and superpose them on a mean velocity profile [Lund et al., 1998]. But this kind of fluctuations are neither spatially nor temporally correlated, and they are not compatible with the Navier-Stokes equations, thus cannot sustain. A second sort of synthetic method is based on the spectrum

of fully developed turbulence. By using Fourier technique [Batten et al., 2004] or other decomposition approaches, turbulent fluctuations are reconstructed by a series of modes. Another method is the synthetic eddy method proposed by Jarrin et al. [2009]. This method decomposes a turbulent flow field into a finite amount of eddies. Velocity fluctuations are generated by those eddies. In addition, all input parameters can either extracted from a precursor LES or an upstream RANS calculation. This method generates stochastic fluctuations based on mean velocity and Reynolds stress profiles. Recently, [Laraufie et al., 2011] developed an interesting method for the initialization of a RANS/LES type calculation when the resolution of the near wall turbulence is turned on RANS mode using a combination of three main ingredients: a Zonal Detached Eddy Simulation (ZDES) type resolution method [Deck et al., 2011], a Synthetic Eddy Method (SEM) [Pamies et al., 2009] and a dynamic forcing approach.

The synthetic method involved in this thesis is the vortex method [Sergent, 2002]. Earliest applications of vortex method are mostly for 2D problems, e.g., simulation of a vortex sheet or flow passing bluff bodies [Rosenhead, 1931][Maull, 1980][Leonard, 1980]. Later, Sergent [2002] used vortex method to generate LES inflow conditions, i.e., a number of vortices are injected in the inlet flow plane (normal to the streamwise direction) to generate 2D velocity fluctuations (e.g., wall-normal and spanwise components on channel flows). Fluctuation on the streamwise direction is generated by using a Langevin equation.

Following the idea of Sergent [2002], Mathey et al. [2006] repeats the simulations on channel flow, and tests the method for hill flow. With this method, 2D and 3D tests on channel and pipe flows are carried out by Benhamadouche et al. [2006]. During his study, the vortex method is also applied on a backstep flow with and without heat transfer. Main idea to use the vortex method for generating LES inflow condition, as proposed by Sergent [2002], consist in using vortex field to generate velocity fluctuations. Based on averaged quantities (mean velocity profile, mean turbulent kinetic energy and dissipation rate profiles), which can be obtained by a RANS calculation or directly extracted from DNS or LES data, a turbulent fluctuating velocity field is reconstructed and superposed on the mean field, thus forming an inflow field for LES.

Compared with the original vortex method proposed by Sergent [2002], the present study will modify basic vortex parameters, especially vortex radius, which will be reformulated. Besides, more parameters will be introduced and studied by considering inhomogeneous turbulence characteristics. Meanwhile, to decrease the demanding adaptation distance, some patterns are used to control the movement of vortex on the inlet plane, in companion with vortex inversion. The comparison with fully developed turbulence obtained by LES with recycling method (e.g., periodic boundary condition in channel flow) [Montorfano et al., 2013][Stolz and Adams, 2003] shows that the improved vortex method (IVM) is more effective and practicable in different cases. The velocity-derivative skewness [Batchelor, 1953] is introduced to qualify the results. This quantity is considered as a new criterion for LES results.

Chapter 1 reviews numerical methods of fluid mechanics pertinent to present study. Different kinds of RANS and LES models are introduced. Especially the RANS k-ω, LES SISM and LES WALE models, which are involved in thesis, are given in details.

In Chapter 2, inflow conditions for LES will be presented, including the concepts and different inflow generation approaches. We will present the original vortex method of Sergent [2002] and the improved vortex method of ours. The velocity-derivative skewness will be introduced as a new LES quality criterion.

The validation of the improved vortex method on channel flows will be presented in Chapter 3. The improved vortex method's parameters will be optimized systematically. Application to a channel flow with higher Reynolds number $Re_\tau = 590$ will be presented.

In Chapter 4, we apply the improved vortex method on flat-plate boundary layer.

Conclusions and perspectives will be drawn at the end of the thesis.

Chapter 1

Numerical methods

The numerical methods, including DNS, LES and RANS as well as associated turbulence models are introduced in this chapter.

1.1 Direct Numerical Simulation

Direct numerical simulation solves the Navier-Stokes equations directly. The incompressible Navier-stokes equations consist of the continuity and momentum equations.

$$\frac{\partial u_i}{\partial x_i} = 0 \tag{1.1}$$

$$\frac{\partial u_i}{\partial t} + u_j \frac{\partial u_i}{\partial x_j} = -\frac{1}{\rho} \frac{\partial p}{\partial x_i} + \nu \frac{\partial^2 u_i}{\partial x_j \partial x_j} \tag{1.2}$$

Since there are 4 equations and 4 unknowns, no closure problem need to be treated. With initial and boundary conditions given, DNS can directly resolve all the scales of turbulent motions. The earliest DNS of homogeneous turbulence [Orszag and Patterson Jr, 1972] at $Re_\lambda = 35$ had only 32^3 grid nodes, λ being the Taylor microscale. Thanks to the rapid development of computers, modern DNS can simulate homogeneous turbulence at Reynolds number $Re_\lambda \sim O(10^3)$ with a mesh of about 4096^3 points. This helps partly confirm the Kolmogorov's hypothesis.

DNS can help get the information which is difficult to measure in experiments, such as pressure fluctuations or vorticities deep inside the flow. For example,

DNS has been used to extract Lagrange statistics [Yeung and Pope, 1989], and statistics of pressure fluctuations [Spalart, 1988], which are almost impossible to obtain by experiments. In that case, DNS is a reliable tool for academic use. Also, the results of DNS can be used as a reference to validate other numerical approaches.

For homogeneous turbulence, pseudo-spectral methods ([Orszag and Patterson Jr, 1972] and [Rogallo, 1981]) are proved accurate and applicable. Considering a cube with length l. The velocity field $\boldsymbol{u}(\boldsymbol{x}, t)$ can be represented with a finite Fourier series

$$\boldsymbol{u}(\boldsymbol{x}, t) = \sum_{\boldsymbol{\kappa}} e^{i\boldsymbol{\kappa} \cdot \boldsymbol{x}} \hat{\boldsymbol{u}}(\boldsymbol{\kappa}, t) \tag{1.3}$$

If N modes are presented in each direction, then in total N^3 wave numbers are obtained

$$\boldsymbol{\kappa} = \kappa_0 \boldsymbol{n} = \kappa_0 (\boldsymbol{e}_1 n_1 + \boldsymbol{e}_2 n_2 + \boldsymbol{e}_3 n_3) \tag{1.4}$$

$$\kappa_0 = \frac{2\pi}{l} \tag{1.5}$$

$$\kappa_{max} = \frac{1}{2} N \kappa_0 = \frac{\pi N}{l} \tag{1.6}$$

This spectral representation is equivalent to $\boldsymbol{u}(\boldsymbol{x}, t)$ in physical space on N^3 number of grids with a uniform spatial spacing

$$\Delta x = \frac{l}{N} = \frac{\pi}{\kappa_{max}} \tag{1.7}$$

The discrete Fourier transform gives a one to one mapping between the Fourier coefficient $\hat{\boldsymbol{u}}(\boldsymbol{\kappa}, t)$ and the velocity $\boldsymbol{u}(\boldsymbol{x}, t)$ on every grid node. In practical computation, fast Fourier transform can be used to transform between wavenumber space and physical space.

An example of a homogeneous isotropic turbulence DNS is given here. Considering that the energy-containing lengthscale is L and Kolmogorov scale equals to η. To accurately describe turbulent motions of the largest scales. The cube size l should be greater enough than L. On the other hand, to accurately predict the smallest scales of motions, the grid spacing Δx must be uniform in all the directions and small enough to correctly capture the smallest turbulent scale,

i.e., the Kolmogorov scale η . The number of grid nodes on one direction should satisfy

$$N_x = l/\Delta x > L/\eta \tag{1.8}$$

Giving the Kolmogorov scale $\eta = (\nu^3/\epsilon)^{1/4}$, and $\epsilon \sim u_{rms}{}^3/L$ (where u_{rms} is RMS of velocity fluctuations), then

$$L/\eta = Re^{3/4} \tag{1.9}$$

Where $Re = \frac{u_{rms}L}{\nu}$, and

$$N_x > Re^{3/4} \tag{1.10}$$

Considering a uniform spatial spacing in all directions, the total number of grids is N_x^3, therefore the grid number is proportional to $Re^{9/4}$:

$$N_x^3 > Re^{9/4} \tag{1.11}$$

For a turbulent flow with a Reynolds number $Re = 10^4$, the total number of mesh required is about 10^9.

In order to make sure the stability of the numerical calculation, the time step should satisfy the CFL condition, the number of CFL should admit

$$CFL = \frac{u'\Delta t}{\Delta x} < CFL_{max} \tag{1.12}$$

Taking the $CFL_{max} = 1$, thus

$$\Delta_t < \frac{\Delta x}{u'} \tag{1.13}$$

To capture the development of turbulence, considering that the integral timescale is about several characteristic time scales of largest vortex L/u', then the total physical time steps required should be at least $L/\Delta x \sim Re^{3/4}$.

To conclude, DNS can provide accurate description of turbulent motions at all the scales, but it demands huge computing power. Thus, for practical problems, DNS is almost impossible. And to tackle the engineering problems, the Reynolds-

Averaged Navier-Stokes approach has been developed.

1.2 Reynolds-Averaged Navier-Stokes Approach

The conception of RANS approach is to solve the statistically average N-S equations. Using Reynolds decomposition, any quantity can be decomposed into its mean part and the fluctuation. For example, the velocity $\boldsymbol{u}(\boldsymbol{x},t)$ can be expressed as

$$\boldsymbol{u}(\boldsymbol{x},t) = \langle \boldsymbol{u}(\boldsymbol{x},t) \rangle + \boldsymbol{u}'(\boldsymbol{x},t) \tag{1.14}$$

Where $\langle \rangle$ denotes ensemble averaging, superscript $'$ denotes fluctuations. Then the mean continuity equation writes:

$$\frac{\partial \langle u_i \rangle}{\partial x_i} = 0 \tag{1.15}$$

And the mean momentum equation is expressed as:

$$\frac{\partial \langle u_i \rangle}{\partial t} + \langle u_j \rangle \frac{\partial \langle u_i \rangle}{\partial x_j} = -\frac{1}{\rho} \frac{\partial \langle p \rangle}{\partial x_i} + \nu \frac{\partial^2 \langle u_i \rangle}{\partial x_j \partial x_j} - \frac{\partial \langle u_i' u_j' \rangle}{\partial x_j} \tag{1.16}$$

1.2.1 Boussinesq eddy viscosity assumption and simple RANS models

As appeared in Eq. (1.16), the Reynolds stress terms $\langle u_i' u_j' \rangle$ make the equations unclosed. In order to solve the RANS equations, the Reynolds stresses need to be modeled. The main idea is to model the Reynolds stresses based on mean velocity field. Following this idea, the Boussinesq eddy viscosity assumption [Schmitt, 2007] is proposed: the Reynolds stresses (anisotropic part) are proportional to the mean rate of strain $s_{ij} \frac{\partial \langle u_i \rangle}{\partial x_j} + \frac{\partial \langle u_j \rangle}{\partial x_i}$

$$-\langle u_i' u_j' \rangle + \frac{2}{3} k \delta_{ij} = \nu_t \left(\frac{\partial \langle u_i \rangle}{\partial x_j} + \frac{\partial \langle u_j \rangle}{\partial x_i} \right) \tag{1.17}$$

Where ν_t is turbulent or eddy viscosity. Giving this coefficient, together with Eq. (1.16), Eq. (1.15) and Eq. (1.17), the RANS equations can be closed.

Then several RANS turbulence models are introduced based on the Boussinesq assumption.

1.2.2   Uniform turbulent viscosity model

As for the uniform turbulent viscosity model, the turbulent viscosity is expressed as

$$\nu_t(x) = \frac{u_0(x)\delta(x)}{Re_T} \tag{1.18}$$

Where $u_0(x)$ and $\delta(x)$ are the characteristic velocity scale and length scale of the mean flow, Re_T is a flow-dependent constant which can be seen as a turbulent Reynolds number. The turbulent viscosity varies in the mean-flow direction. Using this model, it is necessary to define the direction of the flow, the characteristic velocity $u_0(x)$ and length $\delta(x)$. Also, the turbulent Reynolds number Re_T need to be specified. So it is extremely limited to very simple flows, such as the free shear flow. But since the turbulent viscosity varies significantly across the flow, the predicted mean velocity field is not accurate. Despite its incompleteness and limited range of applicability, this model could still provide some basic description about RANS model construction [Pope, 2001].

1.2.3   Mixing length model

The mixing length model is based on the mean free path of molecule. The mixing length l_m can be considered as diffusing particles' the mean free path. The concept of the mixing length is introduced by L. Prandtl [Bradshaw, 1974] and later is used for turbulence modeling. The velocity fluctuation u' is the product of the mixing length and the mean velocity gradient in the streamwise direction

$$u' = l_m |\frac{\partial \langle u \rangle}{\partial y}| \tag{1.19}$$

The turbulent viscosity is the product of the velocity fluctuation and the mixing length:

$$\nu_t = u' l_m = l_m^2 |\frac{\partial \langle u \rangle}{\partial y}| \tag{1.20}$$

In order to allow this model Eq. (1.20) to be applied to all flow types, several generalized forms have been proposed. Based on the mean rate of strain $\langle s_{ij} \rangle$, Smagorinsky [1963] proposed

$$\nu_t = l_m^2 (2\langle s_{ij} \rangle \langle s_{ij} \rangle)^{1/2} \tag{1.21}$$

Another form based on the mean rate of rotation $\langle \Omega_{ij} \rangle$, Baldwin and Lomax [1978] proposed

$$\nu_t = l_m^2 (2\langle \Omega_{ij} \rangle \langle \Omega_{ij} \rangle)^{1/2} \tag{1.22}$$

Even though the mixing-length model can be applicable to all turbulent flows with its generalized form, this model is not complete. The mixing length l_m has to be specified according to the geometry. For a complex flow, the specification of l_m requires a large amount of work. In order to improve the capability of the zero-equation models, several two-equation turbulence models have been proposed.

1.2.4   The k-ϵ model

Based on the Boussinesq eddy viscosity assumption, many more models are developed. Among them, The k-ϵ model [Chien, 1982][Nisizima and Yoshizawa, 1987] is one of the most popular models for RANS approach. It is a two-equation model. In this model, the Reynolds stresses are modeled by two turbulent quantities, the turbulent kinetic energy k and the dissipation rate ϵ. From these two quantities, the turbulent viscosity can be formed as

$$\nu_t = C_\mu \frac{k^2}{\epsilon} \tag{1.23}$$

Where C_μ is a constant. The turbulent viscosity should be related to the characteristic velocity and characteristic length of the flow

$$\nu_t \sim u' L \tag{1.24}$$

Here, the characteristic velocity is the root mean square of the velocity fluctuations, or the characteristic velocity of the energy-containing eddies

$$u' \sim \sqrt{k} \tag{1.25}$$

Since the energy transfer rate from the energy-containing eddies to the smallest eddies equals to ϵ, the characteristic length for the energy-containing eddies is

$$L = \frac{k^{3/2}}{\epsilon} \tag{1.26}$$

Combining Eq. (1.25), Eq. (1.26) and Eq. (1.24), the Eq. (1.23) is obtained. In the k-ϵ model, k and ϵ are calculated with their own transport equations.

$$\frac{\partial k}{\partial t} + \langle u_j \rangle \frac{\partial k}{\partial x_j} = -\langle u_i' u_j' \rangle \frac{\partial \langle u_i \rangle}{\partial x_j} - \frac{\partial}{\partial x_j} \left(\frac{\langle p' u_j' \rangle}{\rho} + \langle u_i' u_i' u_j' \rangle - \nu \frac{\partial k}{\partial x_j} \right) - \nu \langle \frac{\partial u_i'}{\partial x_j} \frac{\partial u_i'}{\partial x_j} \rangle \tag{1.27}$$

$$\begin{aligned}
\frac{\partial \epsilon}{\partial t} + \langle u_k \rangle \frac{\partial \epsilon}{\partial x_k} = &-2\nu \frac{\partial \langle u_i \rangle}{\partial x_k} \langle \frac{\partial u_i'}{\partial x_j} \frac{\partial u_k'}{\partial x_j} \rangle - 2\nu \frac{\partial \langle u_i \rangle}{\partial x_k} \langle \frac{\partial u_j'}{\partial x_i} \frac{\partial u_j'}{\partial x_k} \rangle \\
&- 2\nu \frac{\partial^2 \langle u_i \rangle}{\partial x_k \partial x_j} \langle u_k' \frac{\partial u_i'}{\partial x_j} \rangle - 2\nu \langle \frac{\partial u_i'}{\partial x_k} \frac{\partial u_i'}{\partial x_j} \frac{\partial u_k'}{\partial x_j} \rangle - \nu \frac{\partial}{\partial x_k} \langle u_k' \frac{\partial u_i'}{\partial x_j} \frac{\partial u_i'}{\partial x_j} \rangle \\
&- 2\nu \frac{\partial}{\partial x_k} \langle \frac{\partial p'}{\partial x_j} \frac{\partial u_k'}{\partial x_j} \rangle - 2\nu^2 \langle \frac{\partial^2 u_i'}{\partial x_k \partial x_j} \frac{\partial^2 u_i'}{\partial x_k \partial x_j} \rangle - \nu \frac{\partial^2 \epsilon}{\partial x_i \partial x_i}
\end{aligned} \tag{1.28}$$

In the transport equation for k. Using Eq. (1.17), the production term is modeled as

$$P = -\langle u_i' u_j' \rangle \frac{\partial \langle u_i \rangle}{\partial x_j} = 2\nu_t \langle S_{ij} \rangle \frac{\partial \langle u_i \rangle}{\partial x_j} \tag{1.29}$$

Following the gradient-diffusion hypothesis, with an eddy diffusivity defined as ν_t/σ_k, the diffusion term (second term on the right side of Eq. (1.27)) is modeled as

$$\boldsymbol{T'} = -\frac{\partial}{\partial x_j} \left(\frac{\langle p' u_j' \rangle}{\rho} + \langle u_i' u_i' u_j' \rangle - \nu \frac{\partial k}{\partial x_j} \right) = \frac{\nu_t}{\sigma_k} \frac{k}{x_k} \tag{1.30}$$

Where σ_k is the turbulent Prandle number, usually taken as a order of unit.

Last term of Eq. (1.27) is dissipation rate, its governing equation is the transport equation Eq. (1.28). The mechanism behind the dissipation of turbulent

energy is very complex. Usually, the modeling of dissipation rate follows a similar way as the modeling of transport equation of the turbulent kinematic energy. A transport equation for dissipation rate is built with a production term, a diffusion term and a dissipation term. In total, the closure equations for the k-ϵ model are

$$\frac{\partial k}{\partial t} + \langle u_j \rangle \frac{\partial k}{\partial x_j} = 2\nu_t \langle S_{ij} \rangle \frac{\partial \langle u_i \rangle}{\partial x_j} - \frac{\partial}{\partial x_j}[(\nu + \frac{\nu_t}{\sigma_k})\frac{\partial k}{\partial x_j}] - \epsilon \qquad (1.31)$$

$$\frac{\partial \epsilon}{\partial t} + \langle u_j \rangle \frac{\partial \epsilon}{\partial x_j} = C_{\epsilon 1} \frac{\epsilon}{k}[2\nu_t \langle S_{ij} \rangle \frac{\partial \langle u_i \rangle}{\partial x_j}] - \frac{\partial}{\partial x_j}[(\nu + \frac{\nu_t}{\sigma_\epsilon})\frac{\partial \epsilon}{\partial x_j}] - C_{\epsilon 2}\frac{\epsilon^2}{k} \qquad (1.32)$$

The standard values for all the constants, according to Launder and Spalding [1974], are

$$C_\mu = 0.09, C_{\epsilon 1} = 1.44, C_{\epsilon 2} = 1.92, \sigma_k = 1.0, \sigma_\epsilon = 1.3 \qquad (1.33)$$

The determination of those parameters comes from the study of different turbulent flows, such as the homogeneous shear flow, decaying turbulence and near-wall flows. More details can be found in [Wilcox et al., 1998].

1.2.5 The k-ω model

The k-ω model developed by Wilcox [1988] is introduced here. This is the model used during this thesis. Differing from the k-ϵ model, the second turbulent variable is specific dissipation rate ω, thus the two transport equations for k-ω model [Wilcox, 1988] are

$$\frac{\partial k}{\partial t} + \langle u_j \rangle \frac{\partial k}{\partial x_j} = \langle \tau_{ij} \rangle \frac{\partial \langle u_i \rangle}{\partial x_j} - \beta^* k\omega + \frac{\partial}{\partial x_j}[(\nu + \sigma^* \nu_t)\frac{\partial k}{\partial x_j}] \qquad (1.34)$$

$$\frac{\partial \omega}{\partial t} + \langle u_j \rangle \frac{\partial \omega}{\partial x_j} = \alpha \frac{\omega}{k} \langle \tau_{ij} \rangle \frac{\partial \langle u_i \rangle}{\partial x_j} - \beta \omega^2 + \frac{\partial}{\partial x_j}[(\nu + \sigma \nu_t)\frac{\partial \omega}{\partial x_j}] \qquad (1.35)$$

Where all the constants are given as

$$\alpha = \frac{5}{9}, \beta = \frac{3}{40}, \beta^* = 0.09, \sigma = 0.5, \sigma^* = 0.5 \qquad (1.36)$$

And related to the k-ϵ model, $\beta^* = C_\mu$. The main difference from the k-ϵ model is that, as described by Wilcox et al. [1998], for boundary-layer flows, the k-ω model is superior both in its treatment of the viscous near-wall region, and in its accounting for the effects of streamwise pressure gradients. There exists still a problem, when dealing with non-turbulent free-stream boundaries, a non-zero boundary condition of ω is required. This is non-physical, and the calculated flow is sensitive to the value specified [Wilcox, 2008].

1.3   Large Eddy Simulation

Large-eddy simulation is an intermediate approach between DNS and RANS method. It requires less computing power than DNS and provides better accuracy and more turbulent information than RANS. In large-eddy simulation, the large turbulent motions which contribute mainly to the momentum and energy transfer are computed directly. While effects of the small turbulent motions are modeled. Since the characteristics of small scales are considered being homogeneous, and less affected by the boundary conditions, so their effects may be represented by simple models.

Early work on LES was motivated by meteorology applications [Smagorinsky, 1963][Deardorff, 1974]. Later, LES was developed for the study on isotropic turbulence [Kraichnan, 1976][Chasnov, 1991] and on fully developed turbulent channel flow [Deardorff, 1970][Schumann, 1975][Moin and Kim, 1982][Piomelli et al., 1988]. Further work has been done by Akselvoll and Moin [1996] and Haworth and Jansen [2000] to apply LES to flows in complex geometries in engineering applications. An overview of the development of LES and its applications can be seen in [Galperin, 1993]. Until now. as more accurate models were developed and also owing to the progress of computational resources, LES is applied not only to well documented test cases, but also to more complex flows in industry [Gao et al., 2015].

1.3.1 Filtered N-S equations

To decompose the large scale motions from the small scale motions, a filtering operation is applied in LES. Filtered variables represent the large scale turbulent motions. A filtered velocity is defined by

$$\overline{\boldsymbol{u}}(\boldsymbol{x},t) = \int_D G(\boldsymbol{x},\boldsymbol{r};\Delta)\boldsymbol{u}(\boldsymbol{x}-\boldsymbol{r},t)d\boldsymbol{r} \tag{1.37}$$

Where D is the entire flow domain, G is the filter function and Δ is the filter size (usually taken as the grid size in numerical simulation). The filter function satisfies the normalization condition

$$\int G(\boldsymbol{x},\boldsymbol{r};\Delta)d\boldsymbol{r} = 1 \tag{1.38}$$

The velocity field is decomposed into two parts

$$\boldsymbol{u}(\boldsymbol{x},t) = \overline{\boldsymbol{u}}(\boldsymbol{x},t) + \boldsymbol{u}''(\boldsymbol{x},t) \tag{1.39}$$

Where $\boldsymbol{u}''(\boldsymbol{x},t)$ represents the small scale motions or sub-grid scale motions. The effects of the filtering process are more clearly shown in wavenumber space. Taking the example of the filtering in one dimension, the Fourier transform of the filtered velocity is

$$\hat{\overline{u}}(\kappa) \equiv \mathscr{F}\{\overline{u(x)}\} = \hat{G}(\kappa)\hat{u}(\kappa) \tag{1.40}$$

Where the transfer function $\hat{G}(\kappa)$ is the Fourier transform of the filter function(multiplied by 2π)

$$\hat{G}(\kappa) \equiv \int_{-\infty}^{+\infty} G(r)e^{-i\kappa r}dr = 2\pi\mathscr{F}\{G(r)\} \tag{1.41}$$

Various filters and their transfer functions are given in Tab. 1.1. Taking the example of the sharp spectral filter, Where H is the Heaviside step function and κ_c denotes the cutoff wavenumber

$$\kappa_c \equiv \frac{\pi}{\Delta} \tag{1.42}$$

Filter Name	Filter function	Transfer function
General	$G(r)$	$\hat{G}(\kappa) \equiv \int_{-\infty}^{+\infty} G(r)e^{-i\kappa r}dr = 2\pi\mathscr{F}\{G(r)\}$
Box	$\frac{1}{\Delta}H(\frac{1}{2}\Delta - |r|)$	$\frac{sin(\frac{1}{2}\kappa\Delta)}{\frac{1}{2}\kappa\Delta}$
Gaussian	$(\frac{6}{\pi\Delta^2})^{1/2}exp(-\frac{6r^2}{\Delta^2})$	$exp(-\frac{\kappa^2\Delta^2}{24})$
Sharp spectral	$\frac{sin(\pi r/\Delta)}{\pi r}$	$H(\kappa_c - |\kappa|)$

Table 1.1: Filter function and transfer function for one dimension filters

Fourier modes beyond the cutoff wavenumber κ_c are annihilated.

By applying the filtering operation to the governing equations of incompressible flow, one can obtain the filtered N-S equations

$$\frac{\partial \overline{u}_i}{\partial x_i} = 0 \tag{1.43}$$

$$\frac{\partial \overline{u}_i}{\partial t} + \frac{\partial \overline{u_i u_j}}{\partial x_j} = -\frac{1}{\rho}\frac{\partial \overline{p}}{\partial x_i} + \nu\frac{\partial^2 \overline{u}_i}{\partial x_j \partial x_j} \tag{1.44}$$

Where the term $\overline{u_i u_j}$ can be decomposed into

$$\overline{u_i u_j} = \overline{u}_i \overline{u}_j + (\overline{u_i u_j} - \overline{u}_i \overline{u}_j) \tag{1.45}$$

Thus Eq. (1.44) can be expressed as

$$\frac{\partial \overline{u}_i}{\partial t} + \frac{\partial \overline{u}_i \overline{u}_j}{\partial x_j} = -\frac{1}{\rho}\frac{\partial \overline{p}}{\partial x_i} + \nu\frac{\partial^2 \overline{u}_i}{\partial x_j \partial x_j} - \frac{\partial(\overline{\tau}_{ij}}{\partial x_j} \tag{1.46}$$

Where $\overline{\tau}_{ij}$ are the subgrid scale (SGS) stresses:

$$\overline{\tau}_{ij} = \overline{u_i u_j} - \overline{u}_i \overline{u}_j \tag{1.47}$$

The SGS stresses are to be modeled by SGS models

1.3.2 Subgrid-scale models

Many SGS models have been developed by researchers, such as the Smagorinsky model [Smagorinsky, 1963], the mixed model [Bardina et al., 1980] and the dynamic model [Lilly, 1992][Meneveau et al., 1996]. To be succinct, only the SISM model developed in LMFA [Lévêque et al., 2007]and the WALE model [Nicoud and Ducros, 1999] which are involved in this thesis will be introduced.

1.3.2.1 The SISM model

The Shear-Improved Smagorinsky Model (SISM) proposed by Lévêque et al. [2007] is used in this thesis. This model is developed based on scale-by-scale energy budget in turbulent shear flows. The Smagorinsky eddy-viscosity ν_t is modeled as:

$$\nu_t = (C_s\Delta)^2(|\overline{S}| - |\langle\overline{S}\rangle|) \tag{1.48}$$

Here, $C_s = 0.18$ is the standard Smagorinsky constant, Δ is the local grid spacing, $|\overline{S}|$ is the magnitude of the instantaneous resolved rate-of-strain tensor and $|\langle\overline{S}\rangle|$ is the magnitude of the mean shear.

Two types of interactions representing two basic mechanisms [Shao et al., 1998][Shao et al., 1999] are encompassed in this model. First, the interactions between the mean velocity gradient and the resolved fluctuating velocity which is the rapid part of the SGS dissipation; second, the interactions between the resolved fluctuating velocities which is the slow part of the SGS dissipation. The SISM model is physically sound and can achieve calculation for complex non-homogeneous turbulent flows [Cahuzac et al., 2011][Gao, 2014].

1.3.2.2 The WALE model

The Wall-Adapting Local Eddy-viscosity (WALE) model is proposed by Nicoud and Ducros [1999]. This model is based on the square of the velocity gradient tensor, it takes account of the effects of both the strain and rotation rate of the smallest resolved turbulent fluctuations.

In the WALE model, the Smagorinsky eddy viscosity is modeled as

$$\nu_t = (C_w \Delta) \frac{|G_{ij}^a|^{6/2}}{(S_{ij} S_{ij})^{5/2} + |G_{ij}^a|^{5/2}} \tag{1.49}$$

Where $C_w \sim 0.5$, Δ is the grid spacing based on the cube root of the control volume, and G_{ij}^a is the traceless part of $G_{ij} = 1/2(g_{ik} g_{kj} + g_{jk} g_{ki})$ and $g_{ij} = \partial \overline{u_i} / \partial x_j$.

Like the SISM model, a proper y^3 near-wall scaling can be achieved by this model without requiring dynamic procedure, as well as to handle transition for more complex turbulent flows.

1.3.3   Numerical scheme

All numerical simulations performed in this thesis have been carried out with an in-house solver $Turb'Flow$ which is developed in LMFA. This solver is aimed at computing complex flows, especially flows in turbomachine. A vertex-centered finite-volume discretization on structured multi-block grids is used. The inviscid fluxes are interpolated with a 4-point centered scheme and the viscous fluxes are interpolated with a 2-point centered scheme. A 4th order artificial viscosity is used, as inspired by [Jameson, 1982], to avoid spurious grid-to-grid oscillation in computing compressible flows.

The present thesis computes two basic flows, i.e., channel flow with two different Reynolds numbers, and a flat-plate flow. The computation conditions are given below.

For channel flow at $Re_\tau = 395$, a three-step Runge-Kutta scheme is used for time marching, with a global constant time step of $1 \times 10^{-7}s$. Considering the minimum grid size of $1.3 \times 10^{-5}m$, the reference velocity of $0.59m/s$, this yields a maximum CFL number less then 1.

For channel flow at $Re_\tau = 590$, the global constant time step is 5×10^{-8}. Considering the minimum grid size of $8.5 \times 10^{-6}m$, the reference velocity of $0.59m/s$, this yields a maximum CFL number less then 1.

A local time step is used for the RANS calculations carried on channel flow which yields a maximum CLF number of 1.

For flat-boundary flow calculations, a three-step Runge-Kutta scheme with a global constant time step of $4 \times 10^{-8}s$ is used for temporal discretization. Considering the minimum grid size of $9 \times 10^{-6}m$, the reference velocity of $70m/s$, this results a maximum CFL number less then 1.

Chapter 2

LES inflow conditions and vortex method

Fig. 2.1 illustrates a LES of corner separation in a linear compressor cascade [Gao et al., 2015]. This simulation consists of two parts: the main calculation domain is the compressor cascade channel; the upstream domain is used to generate a fully developed turbulent boundary layer to feed the main calculation. This feeding scheme can provide a good turbulent boundary layer as inlet condition for the compressor cascade computation. However, a flat-plate simulation must conduct simultaneously with the compressor cascade simulation. The flat-plate computation must start from a uniform inlet to accommodate the entire turbulent transition and development processes. This takes almost 1/3 of the total computing power. Therefore, an effective approach to generate LES inflow conditions
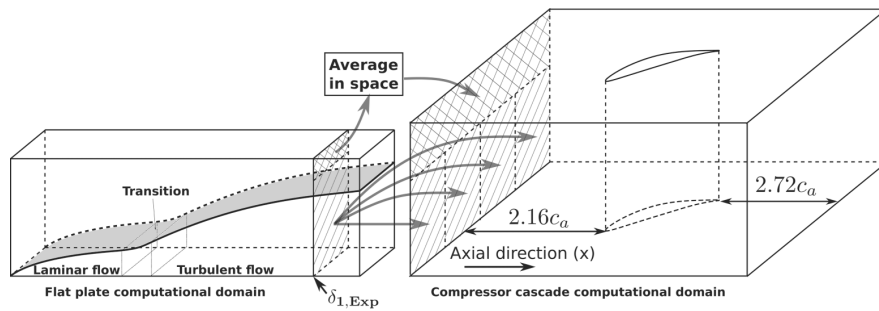

Figure 2.1: A LES case of studying corner separation in a cascade

is desired to reduce the computing power.

In this chapter, a brief literature review of the existing methods for LES inflow generation will be presented. Then the improved vortex method for LES inflow generation developed during this thesis will be introduced in detail. Finally the velocity-derivative skewness [Batchelor, 1953][Tavoularis et al., 1978] is reviewed. This quantity is for the first time, as believed by the author of this thesis, considered as a new criterion for qualifying LES results.

2.1 Inflow conditions for LES

Available LES inflow generation approaches are reviewed by Tabor and Baba-Ahmadi [2010]. In general, the methods for generating unsteady turbulent inflow conditions for LES can be classified into two groups: the precursor simulation methods [Keating et al., 2004] and the synthetic turbulence methods [Laraufie et al., 2011].

The precursor simulation methods require a precursor calculation of a needed type flow to generate turbulent fluctuations to feed the main computation at its inlet. The advantage of this kind of method is that inflow conditions for the main computation are taken from a fully developed turbulent flow. Thus they possess almost all the required turbulence characteristics, especially temporal and spatial correlated structures. The energy cascade is well established. This kind of fully developed turbulent flow can be obtained in many ways, for example using a periodic cube of turbulence, a cyclic channel flow or a long flat-plate to generate a fully developed turbulent boundary layer. Although the precursor simulation methods can give high quality turbulent flow fields, but the computational costs are extremely high, especially for cases at high Reynolds numbers.

The drawback of the precursor simulation methods motivates the synthetic turbulence methods. The strategy is to superimpose fluctuations on a given mean velocity profile. The simplest synthetic method is to add white-noise random components to the mean velocity [Lund et al., 1998], with an amplitude determined by the turbulence intensity level. But the white noise components has few characteristics of turbulence, they are totally uncorrelated in time and in space. Advanced techniques have been developed then. The Fourier type techniques [Lee et al.,

1992][Batten et al., 2004] consider rebuilding the turbulent fluctuations by linear sine and cosine functions, with coefficients representing the energy contained in each mode. Jarrin et al. [2009] developed a synthetic eddy method to generate fluctuations with artificial eddies. This approach superposes a large amount of random eddies, with their statistical properties being controlled. It can provide a flow field with demanded Reynolds stresses and other required turbulent characteristics. In this thesis, another synthetic method, the vertex method of [Sergent, 2002] will be improved and investigated.

2.2 Vortex method

Earliest attempt to simulate a flow with vortex method is carried out by Rosenhead [1931], who simulates the motion of a 2D vortex sheet by following the movement of a system of point vortices. Later this kind of method is developed by Maull [1980] and Leonard [1980]. Their applications are usually for 2D problems, especially the roll-up of a vortex sheet and flow passing bluff bodies. Until recently, The vortex method is used by Sergent [2002] to generate inflow conditions for LES. As a synthetic turbulence method, the main idea of the vortex method is to generate velocity fluctuations with artificial eddies based on mean statistic profiles. The mean statistics can be easily obtained by a RANS calculation or directly extracted from LES or DNS database. Then, the velocity fluctuations are added to the mean velocity profile. This approach can be easily applied to rather complex geometries [Mathey, 2008]. Following Sergent [2002], the generated velocity fluctuations possess some spatial and temporal correlations, since it continuously supplied by a injected vortex field. With this method, the anisotropy of the near wall flow can be taken into account if vortex parameters, e.g. radius, are given according to local turbulence quantities [Mathey et al., 2006]. The adaptation distance to establish realistic statistics can be short, 12 times half channel height for reestablishment according to results of [Benhamadouche et al., 2006]. So, the vortex method can be potentially a relative cost-effective way to generate a turbulent inflow condition for LES, which interests this thesis to study and improve this method.

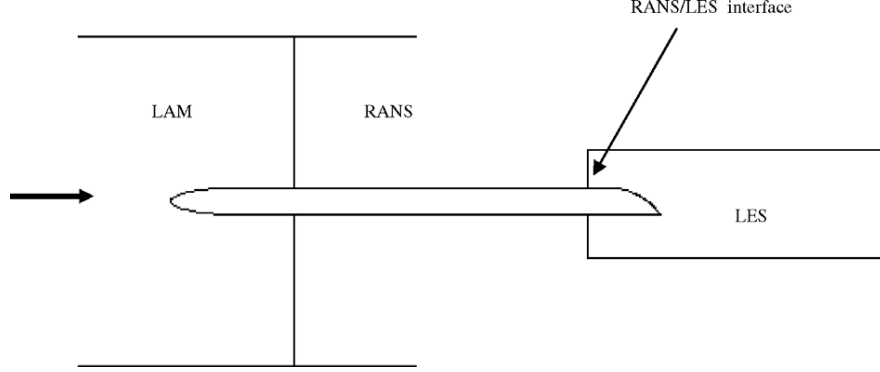Secondly, this method is a hybrid RANS/LES method [Labourasse and Sagaut,

Figure 2.2: A case of hybrid RANS/LES to study the noise at the trailing-edge of an airfoil

2002][Mathey, 2008]. In a multi-domain RANS/LES shown in Fig. 2.2, the region of interest is calculated with LES while the rest part is calculated with RANS. Averaging technique can be used at the interface where the flows pass into the RANS zone from LES zone. But unsteady inflow conditions need to be specified at the interface from RANS to LES. This is exactly what vortex method can do: the upstream RANS provides mean statistics, such as $\langle U \rangle$, u'_{rms}, ϵ, where $\langle U \rangle$ is the mean velocity, u'_{rms} is the RMS of the fluctuating velocity and ϵ is the mean dissipation rate. The vortex method can generate appropriate fluctuating velocity field based on the given mean profiles. Then the fluctuations are added to the mean field to form inflow conditions for the downstream LES calculation.

2.2.1 Methodology

According to Sergent [2002]Benhamadouche et al. [2006], the vortex method uses vortices to generate velocity fluctuations. Theoretically, it is based on the Lagrangian form of the 2D vorticity equation:

$$\frac{\partial \omega}{\partial t} + (\boldsymbol{u} \cdot \nabla)\omega = \nu \nabla^2 \omega \tag{2.1}$$

with

$$\boldsymbol{u} = \nabla \times \boldsymbol{\psi} + \nabla \phi \tag{2.2}$$

Where ψ is the 2D stream function and ϕ is the velocity potential. Taking the curl of Eq. (2.2), one obtains:

$$\omega = -\nabla^2 \psi \tag{2.3}$$

With Eq. (2.2) and Eq. (2.3), Using the Biot-Savart law, the relation between the vorticity and the velocity generated is obtained:

$$\boldsymbol{u}(\boldsymbol{x}) = -\frac{1}{2\pi} \iint_{R^2} \frac{(\boldsymbol{x} - \boldsymbol{x}') \times \omega(\boldsymbol{x}') \cdot \boldsymbol{z}}{|\boldsymbol{x} - \boldsymbol{x}'|^2} d\boldsymbol{x}' \tag{2.4}$$

Where z is the direction of the vorticity vector.

In practice, the entire vorticity field is represented with a number of vortices. Each vortice has its own circulation Γ_i and spatial distribution ξ_i. Given the number of the vortices N and the area of the inlet section S, the amount of vorticity at a position $\boldsymbol{x}$ is expressed as

$$\omega(\boldsymbol{x}, t) = \sum_{i=1}^{i=N} \Gamma_i(\boldsymbol{x}_i(t)) \xi_i(\boldsymbol{x} - \boldsymbol{x}_i(t)) \tag{2.5}$$

Where $\boldsymbol{x}_i(t)$ is the location of vortex center and it can be changed by displacement. ξ is the modified gaussian shape spatial distribution:

$$\xi(\boldsymbol{x}) = \frac{1}{2\pi\sigma^2} e^{-\frac{|\boldsymbol{x}|^2}{2\sigma^2}} (2e^{-\frac{|\boldsymbol{x}|^2}{2\sigma^2}} - 1) \tag{2.6}$$

Where σ is the radius of vortex.

Using Eq. (2.5) and Eq. (2.6) in Eq. (2.4), for a 2D vorticity field with their axes being along the streamwise direction (here, noted as $\boldsymbol{z}$), the generated velocity fluctuation is given by:

$$\boldsymbol{u}(\boldsymbol{x}) = \frac{1}{2\pi} \sum_{i=1}^{N} \Gamma_i \frac{(\boldsymbol{x}_i - \boldsymbol{x}) \times \boldsymbol{z}}{|\boldsymbol{x}_i - \boldsymbol{x}|^2} (1 - e^{-\frac{|\boldsymbol{x}_i - \boldsymbol{x}|^2}{2\sigma_i^2}}) e^{-\frac{|\boldsymbol{x}_i - \boldsymbol{x}|^2}{2\sigma_i^2}} \tag{2.7}$$

Considering an example of 1 vortice, the module of $\boldsymbol{u}(\boldsymbol{x})$ is
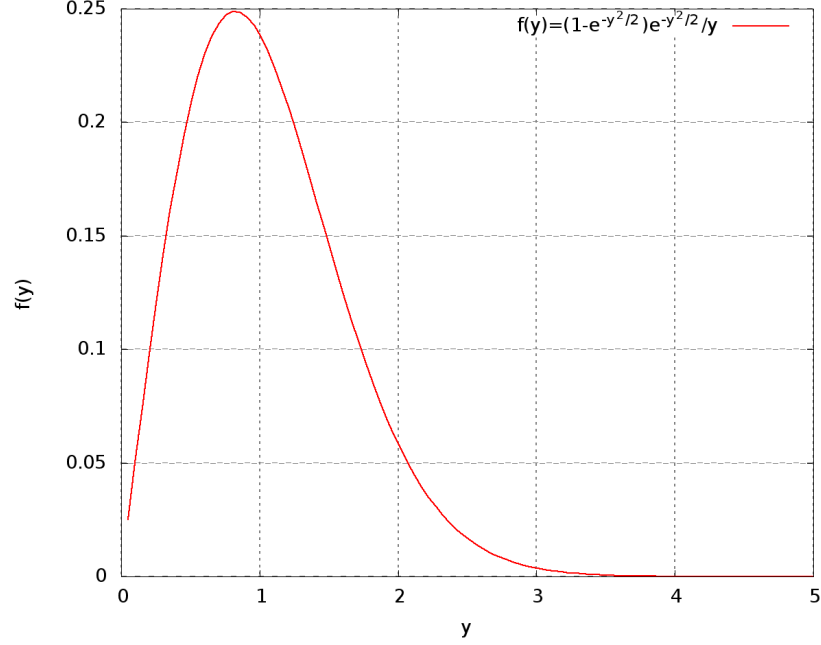
Figure 2.3: Function $f(y) = \frac{1}{y}(1 - e^{-\frac{y^2}{2}})e^{-\frac{y^2}{2}}$

$$|\boldsymbol{u}(\boldsymbol{x})| = |\frac{1}{2\pi}\Gamma_1 \frac{(\boldsymbol{x}_1 - \boldsymbol{x}) \times \boldsymbol{z}}{|\boldsymbol{x}_1 - \boldsymbol{x}|^2}(1 - e^{-\frac{|\boldsymbol{x}_1 - \boldsymbol{x}|^2}{2\sigma_1^2}})e^{-\frac{|\boldsymbol{x}_1 - \boldsymbol{x}|^2}{2\sigma_1^2}}| \tag{2.8}$$

$$= \frac{1}{2\pi}\frac{\Gamma_1}{|\boldsymbol{x}_1 - \boldsymbol{x}|}|(1 - e^{-\frac{|\boldsymbol{x}_1 - \boldsymbol{x}|^2}{2\sigma_1^2}})e^{-\frac{|\boldsymbol{x}_1 - \boldsymbol{x}|^2}{2\sigma_1^2}}| = \frac{\Gamma_1}{2\pi\sigma_1}|f(y)|$$

Where $y = \frac{|\boldsymbol{x}_1 - \boldsymbol{x}|}{\sigma_1}$ gives the ratio between the distance to the center of vortex and the vortex radius, while $f(y)$, shown in Fig. 2.3, is defined as

$$f(y) = \frac{1}{y}(1 - e^{-\frac{y^2}{2}})e^{-\frac{y^2}{2}} \tag{2.9}$$

The peak value of $f(y)$ is about 0.25 at $y = 0.82$. So for very small vortex (e.g., $\sigma = 0.0001$), exceed fluctuations can be generated where near the center of vortex (e.g., $f(0.82) = 0.25$). The resulted fluctuation is $\frac{\Gamma_1}{8\pi\sigma_1} \sim O(10^3)$ if $\Gamma_i \sim O(1)$. Noticing that Γ is independent of σ.

The root mean square velocity fluctuations induced by one vortex is

$$u_i'^2 = \frac{1}{S} \int \int_{R^2} u^2(\boldsymbol{x}) ds \qquad (2.10)$$

For a 2D-vorticity field formed by N vortices, the integration in Eq. (2.10) gives

$$u_i'^2 = \frac{N\Gamma^2(2\ln 3 - 3\ln 2)}{4\pi S} \qquad (2.11)$$

Based on isotropic hypothesis $u'^2 = v'^2 = w'^2 = \frac{2}{3}k$, and only two components are within this 2D plane, thus we have

$$u_i'^2 = \frac{4k}{3} \qquad (2.12)$$

Then the circulation can be obtained

$$\Gamma = 4\sqrt{\frac{\pi S k}{3N(2\ln 3 - 3\ln 2)}} \qquad (2.13)$$

The procedure for applying vortex method of Sergent [2002] in a numerical simulation is illustrated in Fig. 2.4. First, the vortex positions are initialized randomly on a 2D plane. Values of vortex radii and circulations are then specified for each vortex. After initialization, for every time step, every vortex "walks" randomly on the 2D plane and for each period τ, vortices inverse randomly. When a vortex inverses, it is considered as a new one, thus τ is also named the lifetime of vortex. Next, since vortex locations and rotation senses (correspond with the sign of Γ [Sergent, 2002]) change, we need to compute the new values of radii and circulations and then the generated velocity fluctuations. At last, the fluctuations generated by those vortices are added to the mean velocity profile and involve in the LES computation.

Regarding wall flows, ghost vortices will be used in order to let the velocity be zero on the wall and grow gradually. Details about the use of ghost vortices are explained in [Sergent, 2002][Benhamadouche et al., 2006]. So the velocity fluctuations are calculated with both the real and the ghost vortices.

The idea of original vortex method of Sergent [2002] consists in constructing
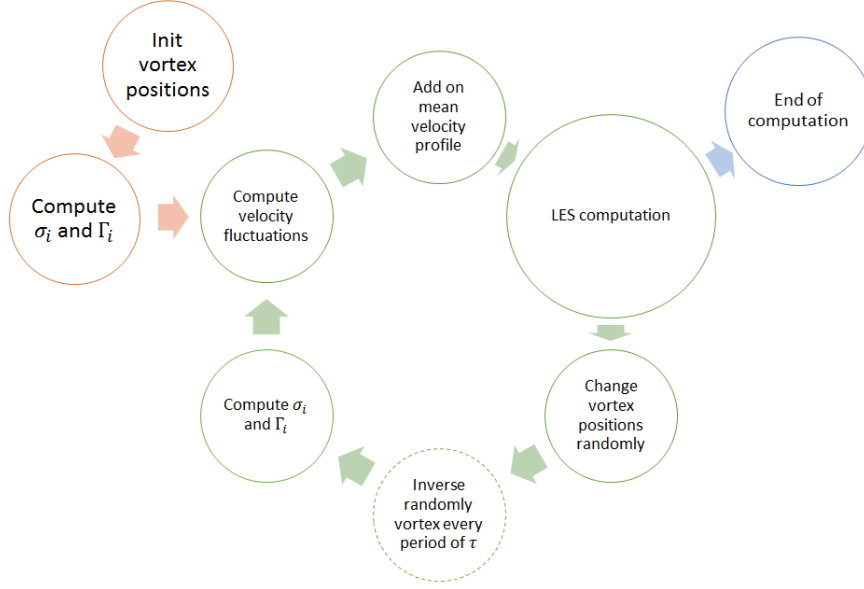
Figure 2.4: Flowchart of vortex method ([Sergent, 2002])

a fluctuating velocity field which correspond well with the RMS profiles of fully developed flows at the inlet plane. Vortices with axe along the streamwise direction are used to generate a 2D velocity fluctuations, while fluctuations along the streamwise direction are generated by the Langevin equation. In order to obtain an appropriate unsteady flow field, several parameters have been studied by Sergent [2002]:

i. Vortex radius σ

ii. Number of vortices N

iii. Random displacement's velocity U_d

iv. Vortex lifetime τ, vortice may inverse for each τ

v. Circulation type based on rate of dissipation or velocity fluctuations

Through a series test cases and comparison of the generated fluctuations RMS profiles with the DNS data, Sergent [2002] suggests that the most important parameters are the vortex radius σ and the velocity magnitude of vortex's random

displacement U_d. However, no quantitative criteria have been given. In this original vortex method, the vortex radius is defined as either a constant or by a adhoc linear function of wall distance. The displacement velocity of vortex is also prescribed as a constant. Little work has been conducted to investigate the influences of those parameters on the development of turbulence through the streamwise direction. With this original vortex method, a long adaptation distance is required along streamwise direction to reestablish high quality turbulence downstream. An example of channel flow test case indicated that 5 times the half channel height was far from enough [Sergent, 2002]. Following Sergent's method, Benhamadouche et al. [2006] perform a test on channel flow with $Re_\tau = 395$ where $Re_\tau = \frac{u_\tau h}{\nu}$ and h is the half channel height. Results of RMS profiles show that the turbulence tends to establish from around $x/h = 12$.

2.2.2 Improvement of the vortex method

For synthetic turbulence methods, the adaptation distance is always necessary. The fluctuating velocity field generated by synthetic turbulence methods is not spatially or temporally correlated as real turbulence. It requires an adaptation distance to develop into or nearly to a fully developed turbulent field. This demands additional computational costs. So, reducing the adaptation distance is of great significance. This motivates the work involved in this thesis.

The original vortex method of Sergent [2002] uses random vortices (vortex axes are along the streamwise direction) to generate 2D (spanwise and wall-normal) fluctuations, while the streamwise direction fluctuations are forced by a separate equation, thereby being uncorrelated with other components. Different from the original vortex method which aims at prescribing a fluctuating velocity field, of which the RMS profiles are expected to match the DNS data (fully developed flow field), the improved vortex method focuses on the development of downstream turbulence rather than paying too much attention to the fluctuations generated on the inlet plane. Although the velocity field downstream depends a lot on the inlet synthetic turbulent field, the development of turbulence can be accelerated with some techniques. Based on the original vortex method of [Sergent, 2002], several parameters are introduced to accelerate the establishment of turbulence,
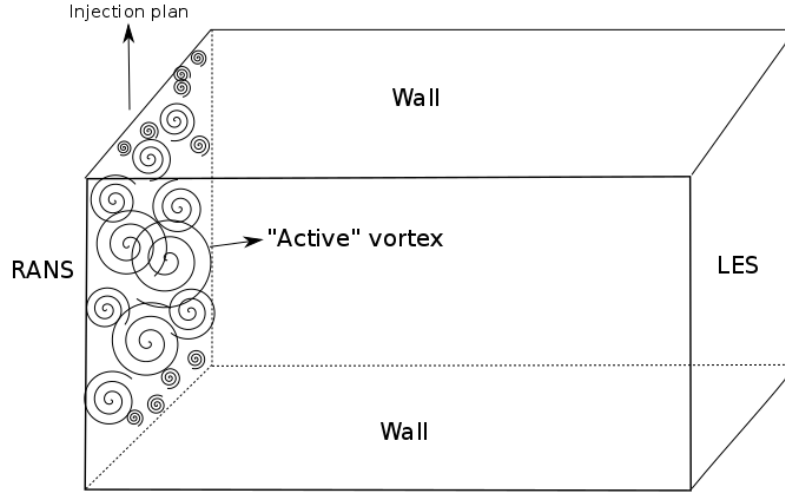
Figure 2.5: Illustration of the improved vortex method

expecting to achieve a shorter adaptation distance.

In the improved vortex method, the basic parameters keep the same. In order to make the vortex method more generally applicable and take into account of anisotropy of the near wall flow, local parameters are considered. Vortex parameters are determined according to local mean turbulent kinetic energy and mean dissipation rate which can come from RANS calculation.

From a point of view of physic, the vortices can be seen as the source of perturbations on the mean velocity field. The fluctuations generated and their reactions with the mean velocity field determine the development of turbulence downstream. Thus the displacement and inverse of vortices are of great importance during this process. A grid turbulence generator [Comte-Bellot and Corrsin, 1966][Sumer et al., 2003] is compared here to understand this principle. Every vortex can be considered as generated by an active grid which can move and rotate in either clockwise or anticlockwise direction. Besides, inspired by forcing turbulence of [Eswaran and Pope, 1988] and [Alvelius, 1999], resulted turbulence is strongly influenced by the forcing methods. The forcing scheme can be compared with the displacement of vortex. Here, some patterns are introduced to
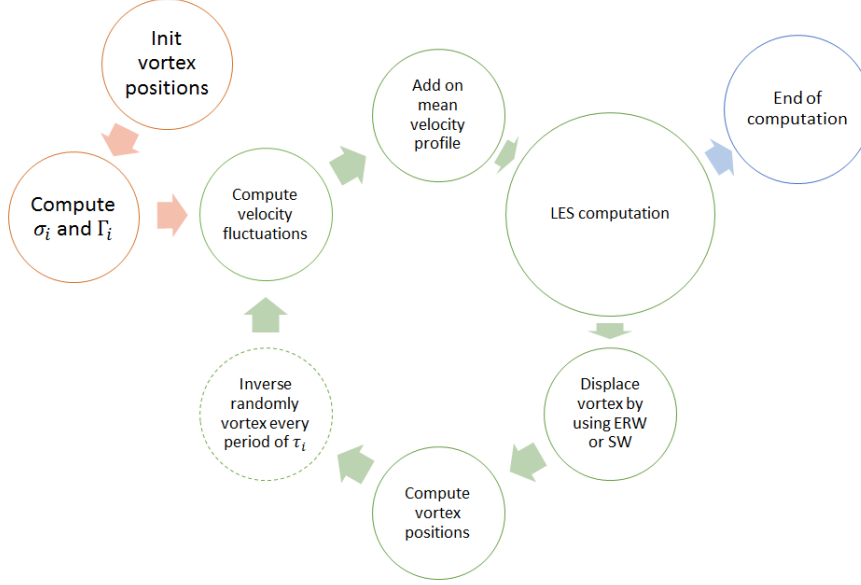
Figure 2.6: Flowchart of the improved vortex method (bxie)

control the displacement of vortices on the inlet plane. A local turbulent time
scale τ is taken for the lifetime. The illustration of the improved vortex method
is shown in Fig. 2.5. Flowchart of applying the improved vortex method is a little
different from the original one, as shown in Fig. 2.6. We use either enhanced
random walk (ERW) or stochastic walk (SW) to displace vortices. When vortices
move to new positions, we do not re-compute vortex radii and circulations. Vor-
tices with different sizes radii can present different features of displacement thus
influence the generated fluctuations and this will be explained in detail in 2.2.2.4.
The parameters of the improved vortex method are

   i. Radius σ.

  ii. Circulation Γ.

 iii. Lifetime τ.

 iv. Displacement, pattern of which can either be ERW or SW.
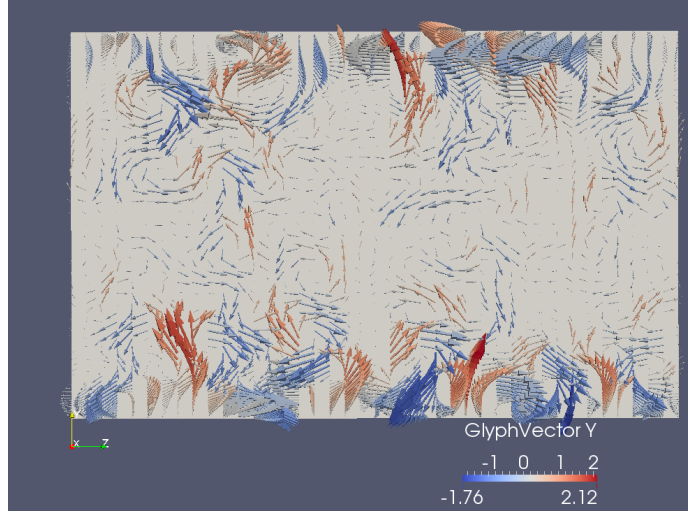
Figure 2.7: 2D instantaneous velocity field obtained with $\sigma = 0.1$, case of channel flow with $Re_\tau = 395$

2.2.2.1 Radius σ

Vortex radius σ in Eq. (2.7) corresponds to the size of the vortex. Sergent [2002] has studied the sensitivity of the method to different values of σ. A series of adhoc values of σ is studied (i.e., all vortices share the same adhoc value of σ while this value vary from different tests or follow a adhoc linear function of wall distance). Results show that the size of vortex has a non-negligible influence on the position of the peak of the generated fluctuations. The bigger the radius, the further away from the wall the peak locates.

Following Sergent's setup for the value of σ, [Benhamadouche et al., 2006] perform some 2D and 3D tests with channel and pipe flows and apply the vortex method on a backstep flow. The value imposed for σ is 0.1, resulting instantaneous velocity fluctuations at inlet plan on channel flow is given by Fig. 2.7

In order to make the vortex method generally applicable, Mathey et al. [2006] proposed a local vortex size which is specified through a turbulent mixing length hypothesis. σ is calculated from a known profile of the mean turbulent kinetic

energy and mean dissipation rate at the inlet:

$$\sigma = \frac{C_\mu^{0.75}}{2} \frac{k^{3/2}}{\epsilon} \tag{2.14}$$

Where $C_\mu = 0.09$. In order to ensure that the vortex always belongs to resolved scales, the minimum value of σ is bounded by the local grid size Δ, i.e., $\sigma > \Delta$.

The formulation of vortex radius given by Mathey et al. [2006] is based on a energy-containing lengthscale L ($L = \frac{k^{3/2}}{\epsilon}$) which can characterize large eddies. Since radius size is specified locally, i.e., it is determined by local turbulent kinetic energy and dissipation rate, anisotropic characteristics could be taken into account. While the treatment of small size vortex (bounded by the local grid scale) is quite adhoc.

Inspired by Mathey et al. [2006], the radius size σ should be comparable to a lengthscale $L = \frac{k^{3/2}}{\epsilon}$, e.g., energy-containing scale or integral scale, which can characterize large eddies:

$$\sigma \sim \frac{k^{3/2}}{\epsilon} \tag{2.15}$$

From a view of energy cascade, eddies of these sizes are responsible for energy containing and transferring. The form of Eq. (2.14) is tested in this thesis. First test is without any adhoc treatment of the small size vortices. Following Eq. (2.14), very small size vortices (σ may be inferior then local grid size) can be injected. Test shows that when treating inhomogeneous turbulence near wall, numerical stability problem appears. This is due to the very small size vortices created near wall. When σ is very small, according to Eq. (2.7), exceed fluctuations can be generated on some grid points which are very close to vortex center, as shown in Fig. 2.8. In consequence, the calculation stops after some time due to the numerical instability cause by these exceed velocities.

Although Mathey et al. [2006] has provided an adhoc way to bound the size of vortices. But this kind of adhoc treatment is not adopted by this thesis, thus a new formulation of vortex radius is introduced here.

Considering homogeneous isotropic turbulence, the ratios of the smallest eddy scales (i.e., Kolmogorov scale $\eta \equiv (\nu^3/\epsilon)^{1/4}$) to large eddy scales (i.e., energy-containing scale $L \equiv \frac{k^{3/2}}{\epsilon}$) can be determined from the definition of the Kol-
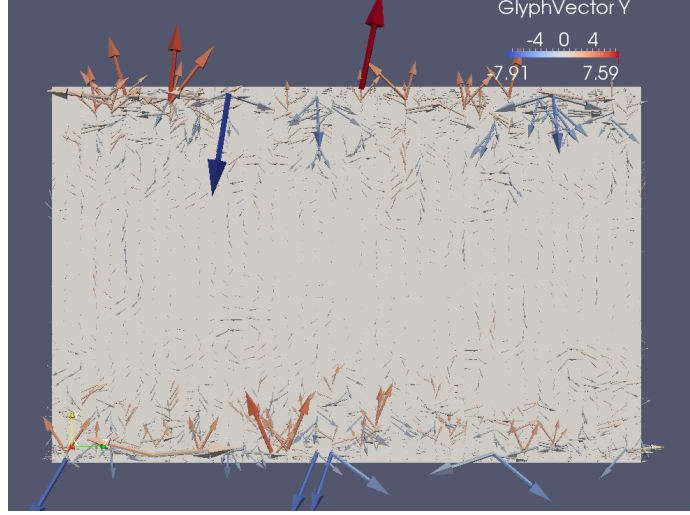
Figure 2.8: 2D instantaneous velocity field obtained with $\sigma = \frac{C_\mu^{0.75}}{2}\frac{k^{3/2}}{\epsilon}$, case of channel flow with $Re_\tau = 395$

mogorov scales and from the scaling

$$\epsilon \sim u_L^3/L \tag{2.16}$$

Where u_L is the velocity characterizing large eddy scales.

Thus, we have

$$\eta/L \sim Re_L^{-3/4} \tag{2.17}$$

Where $Re_L = \frac{u_L L}{\nu}$ is the characteristic Reynolds number.

So we propose another formulation for the radius σ which is related to the Kolmogorov scale η by introducing a local Reynolds number $Re_{local}^{3/4}$ which is determined by flow itself.

$$\sigma = C_1 Re_{local}^{3/4}(\nu^3/\epsilon)^{1/4} \tag{2.18}$$

Where C_1 is a coefficient which needs to be optimized.

The dimensionless form (practical for programming and result analysing) in wall unit is

$$\sigma^+ = C_1(\nu^+/\epsilon^+)^{1/4} \tag{2.19}$$

Where ν^+ is unit if the characteristic viscosity for normalization is chosen as the
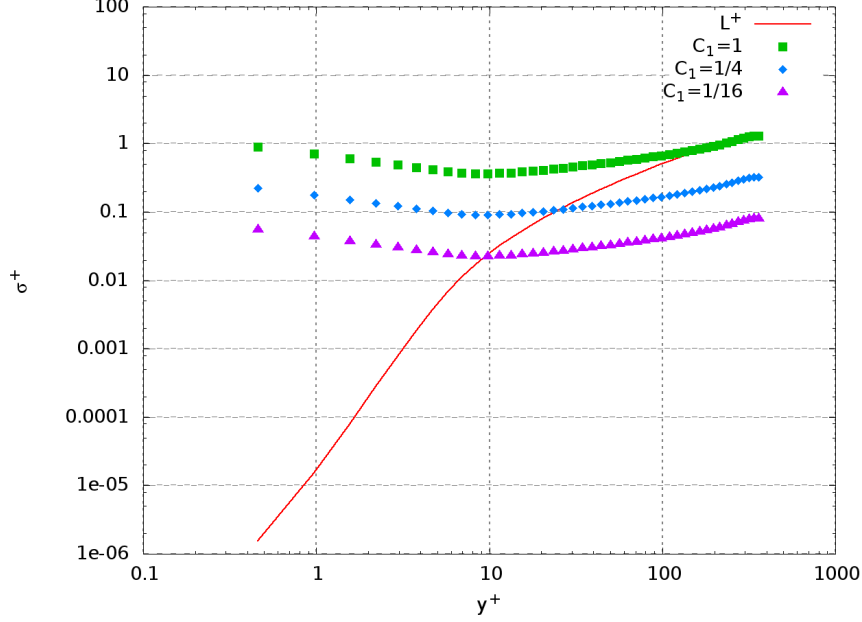
Figure 2.9: Comparison between σ^+ and L^+, case of channel flow with $Re_\tau = 395$

viscosity of flow itself.

A problem appears when using Eq. (2.18) to specify vortex radius σ, as we have to determine coefficient C_1 in Eq. (2.18). In this thesis, a practical way is proposed to determine this coefficient. Taking an example of channel flow with $Re_{local} = Re_\tau = 395$. The radius σ is specified as

$$\sigma = C_1 Re_\tau^{3/4} (\nu^3/\epsilon)^{1/4} \tag{2.20}$$

With given mean turbulent kinetic energy and dissipation rate (e.g., from a RANS calculation), curve of $L^+ = \frac{k^{+3/2}}{\epsilon^+}$ can be drawn. Then curves of Eq. (2.19) with different values of C_1 can be drawn as well, as shown in Fig. 2.9. Considering the range of interest between $y^+ = 10$ and $y^+ = 100$, curve with $C_1 = 1/4$ agrees best with the one of L^+. C_1 is then preliminarily valued around $1/4$. In advance, radius with different C_1 in a suitable range will be tested with a series calculations. Further details and results can be seen in section 3.1.3.3. It should be noticed that the Eq. (2.18) is flow depending. In practical, the value of C_1 could be determined by the method introduced here.
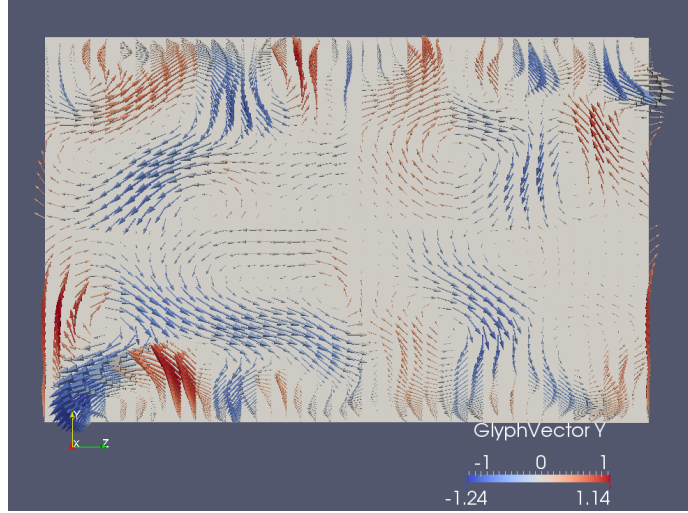
Figure 2.10: 2D instantaneous velocity field obtained with $\sigma^+ = C_1(\nu^+/\epsilon^+)^{1/4}$, case of channel flow with $Re_\tau = 395$

There are several advantages to use Eq. (2.18) to specify vortex radius σ. First, this formulation can be applied to different type of flows, as a local Reynolds number which depends on flow itself is involved, making the method more generally applicable. According to the turbulent energy cascade, when the dissipation rate is large, the vortices are considered to be small. Eq. (2.18) is in accord with this idea. Second, no adhoc treatments need to be done when using Eq. (2.18) to specify σ (applications on channel flows are shown in Chapter 3 and flat-plate flows in Chapter 4). Considering the displacement of vortex introduced later in subsection 2.2.2.4, vortex displacement is directly related to its radius size, so vortices with large and small sizes are all of great interest.

2.2.2.2 Circulation Γ

The circulation is directly linked to the intensity of the generated fluctuations. The formulation follows Sergent [2002] with the isotropic hypothesis

$$\Gamma_0 = 4\sqrt{\frac{\pi S k}{3N(2\ln 3 - 3\ln 2)}} \tag{2.21}$$

Here, in order to control the intensity of the fluctuations generated, a coefficient C_2 is introduced and needs to be calibrated with test cases.

$$\Gamma = C_2\Gamma_0 = 4C_2\sqrt{\frac{\pi Sk}{3N(2\ln 3 - 3\ln 2)}} \tag{2.22}$$

The intensity of generated fluctuations should be compatible with the mean turbulent kinetic energy which comes from the RANS calculation, otherwise stability problem may occur during the numerical simulation. Results can be seen in subsection 3.1.3.3.

$$v'_{rms} \simeq w'_{rms} \sim \sqrt{k} \tag{2.23}$$

2.2.2.3   Lifetime τ

For every period τ, a vortex changes randomly its rotating sense. When a vortex inverses, its lifetime is over and the vortex with an inverse sense is considered as new spawn one. Thus, this time interval τ is also named the lifetime of a vortex. Through Eq. (2.7), it can be seen that inverse of a vortex equals to changing the sign of its circulation. In original vortex method, the lifetime of vortex is specified with some adhoc value. In the improved vortex method, τ is based on a local turbulent timescale

$$\tau = C_3\frac{k}{\epsilon} \tag{2.24}$$

Here, a coefficient C_3 is introduced and needs to be adjusted with test cases. Details about tests can be seen in subsection 3.1.3.3.

2.2.2.4   Vortex displacement

Two patterns for vortex displacement are introduced and studied here

a.) Enhanced random walk.

b.) Stochastic walk controlled by Langevin equation.

In the original vortex method, the vortices "walk" at each time step to mimic the Brownian motion. But it is observed that most vortices just oscillate around

their initial positions with very small amplitudes. The amplitudes can be eval-
uated by their displacement velocities on the inlet plane and the time interval
during which they hold the displacement direction. This can be explained by
Fig. 2.11. According to the set by Sergent [2002], the displacement velocity scale
on the inlet plane equals the magnitude of the bulk velocity $\overline{U}$, and the time
interval is the time step dt of the calculation, thus the step length λ_0 of this kind
of random walk is

$$\lambda_0 \sim \overline{U} dt \tag{2.25}$$

However, with this kind of random displacement, vortices are not active
enough to perturb the mean velocity field. In addition, to insure the efficiency
of the method, the number of vortices is limited. Therefore, in order to make
these vortices active enough, some new patterns are introduced here to control
the displacement of vortices.

Enhanced random walk

The first pattern for the displacement of vortices is the enhanced random walk
(ERW). The enhanced random walk forces the vortices to walk on the inlet plane
with a typical step length λ. For every distance λ walked, the vortices change
randomly their directions, and walks for another distance λ, as shown in Fig. 2.11.
When vortices reach a wall or other boundaries, it will bounce back. The step
length λ is based on the vortex radius ($\simeq 0.1\lambda$ according to tests results of Chapter
3), and much larger than that of Sergent's random walk λ_0:

$$\lambda \sim 0.1\sigma \gg \lambda_0 \tag{2.26}$$

The characteristic velocity scale for displacement equals to the magnitude of
local bulk velocity at inlet. With the pattern of ERW, vortices can move anywhere
on the inlet plane. The active level of a vortex is represented by the step length
λ. Noticing that vortices with larger radii correspond with larger step lengths as
well, which are more active. This is compatible with the dynamic characteristic of
fluid. The radius specified by Eq. (2.18) and with no adhoc treatment make sense
here. To study the influence of the step length on the development of turbulence
along the streamwise direction, a coefficient C_4 is introduced and to be tuned
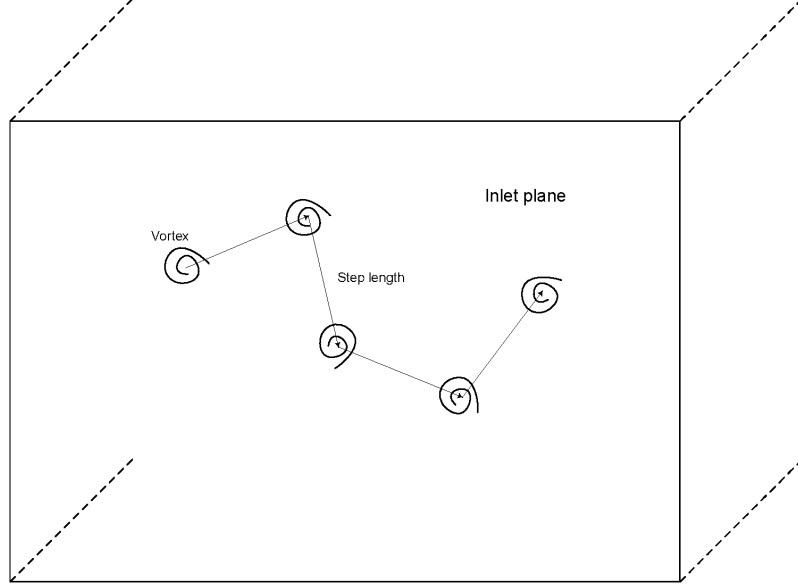
Figure 2.11: Schematic of enhanced random walk

with test cases. Results of tests can be seen in subsection 3.1.3.3.

$$\lambda = C_4 \sigma \tag{2.27}$$

Stochastic walk

The generated fluctuating velocity field are usually lack of temporal correlation. Temporal correlation of generated fluctuations may be forced by displacement of vortices. This motivates the use of Langevin equation. This kind of vortex displacement is also named the stochastic walk (SW). With random walk, the vortices move along a random direction with a specific velocity scale. While in stochastic walk, the velocity vector of displacement is governed by the Langevin equation [Pope, 2001]

$$\vec{U}(t + \Delta t) = \vec{U}(t) - \frac{\Delta t}{T_L}\vec{U}(t) + \frac{2\gamma^2 \Delta t^{1/2}}{T_L} \Xi(t) \tag{2.28}$$

While the velocity variance γ is given by

$$\gamma^2 = \frac{2}{3}k \tag{2.29}$$

The integral timescale T_L of the process is given by

$$T_L^{-1} = \frac{C_5\epsilon}{2\gamma^2} = \frac{3}{4}C_5\frac{\epsilon}{k} \tag{2.30}$$

And $\Xi(t)$ is a standardized Gaussian random variable which is independent of itself at different times. With the coefficients expressed in forms above, the Langevin equation becomes

$$\vec{U}(t + \Delta t) = (1 - \frac{3}{4}C_5\frac{\epsilon}{k}\Delta t)\vec{U}(t) + (C_5\epsilon\Delta t)^{1/2}\Xi(t) \tag{2.31}$$

The velocity vector for vortex displacement consists of two parts: a totally random part and a determined part (velocity vector at the last time step). The initial values in Eq. (2.31) are considered having less influence on the velocity vector after enough long time. Then the displacement will be only determined by the coefficient C_5 which needs to be calibrated by test cases. Results about tests can be seen in subsection 3.1.3.3.

All the parameters of the improved vortex method are summarized in Tab. 2.1. Further systematic parameter optimization study will be carried out with computations on channel flows ($Re_\tau = 395$) in Chapter 3.

2.3   The LES quality and the velocity-derivative skewness

No matter using the precursor methods or synthetic turbulence methods to generate inflow conditions for LES, the obtained flow field needs to be qualified before being introduced as inflow of the main computation. So the next question comes out, what are the appropriate criteria to qualify the turbulent flow field obtained by these methods? In general, there are two ways for examining: a priori way and a posteriori way. Several statistic quantities are used to examine LES results,

Parameter	Formula	Description
Radius σ	$\sigma = C_1 Re_{local}^{3/4}(\nu^3/\epsilon)^{1/4}$	Based on energy-containing scale, related to local dissipation rate
Circulation Γ	$\Gamma = C_2 \Gamma_0$	Γ_0 ([Sergent, 2002]), isotropic hypothesis
lifetime τ	$\tau = C_3 \frac{k}{\epsilon}$	Local turbulent timescale
Displacement Pattern 1	$\lambda = C_4 \sigma$	Enhanced random walk
Displacement Pattern 2	The model coefficient C_5	Stochastic walk

Table 2.1: Parameters of the improved vortex method

and they will be reviewed shortly here. Those quantities can describe the features of turbulence from different views. As is described by the energy cascade, the energy transferred from the large scale turbulent motions to the small ones successively. When the turbulence is fully developed, the energy transferred to the small scales motions is balanced with the dissipation. Related to the LES, it is equals to the dissipation presented by the SGS stress model. The key point of LES is whether the SGS stress model can accurately quantify the dissipation effect of unresolved scales motions or not. To describe this equilibrium between the energy transferred from large scales and dissipation of the resolved scales, the velocity-derivative skewness is introduced. Because in the framework of isotropic homogeneous turbulence, this quantity is related to the energy transfer between different scales. Results of experiments and DNS showing that this quantity can be potentially used to as a criterion to qualify LES.

2.3.1   General examinations of the LES performance

An a priori test uses experimental or DNS data to measure directly the accuracy of a modeling assumption. While in an a posteriori test, the model is used to perform a calculation for a well known turbulent flow. Then some statistic quantities(e.g. $\langle u_i \rangle$ and $\langle u_i' u_j' \rangle$) are calculated and are compared with reference data which usually come from a DNS. Vremen et al. [1997] proposed that several quantities can be considered as criteria to quantify the quality of LES: the evolution of total kinetic energy, turbulent and molecular dissipation, backscatter and energy spectra, etc. These parameters are summarized in Tab. 2.2.

The decay of the total kinetic energy is caused mainly by the SGS dissipation, as is modeled by SGS stress model. A small part is due to the molecular dissipation which is not comparable to the SGS dissipation. Non eddy viscosity models can have mechanisms to produce backscatter of energy from subgrid to resolved scales, thus the backscatter need to be calculated [Bertoglio, 1985]. The vorticity can be used to visualize the large scale roller structure of the flows. As with mixing layer, the positive spanwise vorticity is related to the transition to turbulence. The turbulent stress tensor accounts for the transfer of kinetic energy from resolved scale to subgrid scales. The momentum thickness is an important quan-

Quantity	Formula
Total kinetic energy k	$\int \overline{u}_i \overline{u}_i d\boldsymbol{x}$
Dissipation due to SGS stress ϵ_{SGS}	$\int -\rho \overline{\tau}_{ij} \overline{S}_{ij} d\boldsymbol{x}$
Backscatter	$\int min(-\rho \overline{\tau}_{ij} \overline{S}_{ij}, 0) d\boldsymbol{x}$
Energy spectrum	$E(\kappa)$
Vorticity	$\overline{\omega}_i$
Momentum thickness	-
Averaged statistics	$\langle u_i \rangle$, $\langle u'_i u'_j \rangle$, etc

Table 2.2: Quantities for qualifying LES result

tity for the boundary layer. It can be used to quantify the spreading of the mean velocity profile. Statistic quantities like $\langle u'_i u'_j \rangle$ are related to the fluctuations.

2.3.2 Energy transfer in LES

An important issue in LES is to correctly simulate the transfer of kinetic energy between the filtered or the resolved motions and the residual or the unresolved motions. The filtered kinetic energy $\overline{E}$ is obtained by filtering the kinetic energy filed as

$$\overline{E} \equiv \frac{1}{2}\overline{\boldsymbol{u} \cdot \boldsymbol{u}} \tag{2.32}$$

This quantity can be decomposed as

$$\overline{E} = E_f + E_r \tag{2.33}$$

Where E_f is the kinetic energy of the filtered velocity field, and E_r is the residual kinetic energy

$$E_f = \frac{1}{2}\overline{\boldsymbol{u}} \cdot \overline{\boldsymbol{u}} \tag{2.34}$$

The conservation equation for E_f is

$$\frac{\partial E_f}{\partial t} + \overline{u}_i \frac{E_f}{\partial x_i} - \frac{\partial}{\partial x_i}[\overline{u}_j(2\nu\overline{S}_{ij} - \tau_{ij}^r - \frac{\overline{p}}{\rho}\delta_{ij})] = -\epsilon_f - P_r \tag{2.35}$$

Where τ_{ij}^r is the anisotropic part of the SGS stress tensor, and ϵ_f, P_r are defined as

$$\epsilon_f = 2\nu\overline{S}_{ij}\overline{S}_{ij} \tag{2.36}$$

$$P_r = -\tau_{ij}^r\overline{S}_{ij} \tag{2.37}$$

The terms on the left side of Eq. (2.35) represent transport, and the sink terms on the right side are of most interest. The sink $-\epsilon_f$ represents the viscous dissipation due to the filtered velocity field. This term is relatively small for a high Reynolds number flow with a fine enough (much larger than the Kolmogorov scale$\sim 2\eta$) filter width. The term P_r is the rate of production of the residual kinetic energy. This term appears as a sink $(-P_r)$ in the equation for E_f and as a source $(+P_r)$ in the equation for E_r. It represents the rate of transfer of energy from the filtered motions to the residual motions. At high Reynolds number, with the filter in the inertial subrange, the filtered velocity field equals nearly all of the kinetic energy

$$\langle E_f \rangle \simeq \langle E \rangle \tag{2.38}$$

The dominant sink in the equation of for $\langle E_f \rangle$ is $\langle P_r \rangle$, since $\langle -\epsilon_f \rangle$ is negligible comparable with $\langle P_r \rangle$, thus, the sink term $\langle P_f \rangle$ equals nearly to the dissipation of kinetic energy ϵ

$$\langle P_f \rangle \simeq \epsilon \tag{2.39}$$

Even though, locally there can be backscatter, when transfer of energy is from the residual motions the the filtered velocity field. But globally, the transfer of energy is mostly from the large scales to the small scales. This is the main aim of any eddy viscosity type SGS model.

2.3.3 Introduction of the velocity-derivative skewness in isotropic homogeneous turbulence

2.3.3.1 The velocity-derivative skewness and the Karman-Howarth equation

For incompressible flow, the time derivative of two-point correlation $R_{ij}(\boldsymbol{r}, t)$ can be derived from N-S equations of velocity fluctuations.

$$\frac{\partial R_{ij}(\boldsymbol{r}, t)}{\partial t} = T_{ij}(\boldsymbol{r}, t) + P_{ij}(\boldsymbol{r}, t) + 2\nu \frac{\partial^2 R_{ij}(\boldsymbol{r}, t)}{\partial r_k \partial r_k} \tag{2.40}$$

With,

$$T_{ij}(\boldsymbol{r}, t) = \frac{\partial}{\partial r_k} (\langle u_i(\boldsymbol{x}, t) u_k(\boldsymbol{x}, t) u_j(\boldsymbol{x} + \boldsymbol{r}, t)\rangle - \langle u_i(\boldsymbol{x}, t) u_k(\boldsymbol{x} + \boldsymbol{r}, t) u_j(\boldsymbol{x} + \boldsymbol{r}, t)\rangle) \tag{2.41}$$

$$P_{ij}(\boldsymbol{r}, t) = \frac{1}{\rho} \left(\frac{\partial \langle p(\boldsymbol{x}, t) u_j(\boldsymbol{x} + \boldsymbol{r}, t)\rangle}{\partial r_i} - \frac{\partial \langle p(\boldsymbol{x} + \boldsymbol{r}, t) u_i(\boldsymbol{x}, t)\rangle}{\partial r_j} \right) \tag{2.42}$$

For isotropic turbulence, the pressure-gradient term in the equation for time derivative of $R_{ij}(\boldsymbol{r}, t)$ is zero. The convective term $T_{ij}(\boldsymbol{r}, t)$ involves two-point triple velocity correlations, such as

$$S_{ijk}(\boldsymbol{r}, t) = u_i(\boldsymbol{x}, t) u_j(\boldsymbol{x}, t) u_k(\boldsymbol{x} + \boldsymbol{r}, t) \tag{2.43}$$

In isotropic turbulence $S_{ijk}(\boldsymbol{r}, t)$ is uniquely determined by its longitudinal correlation

$$k(r, t) = S_{111}(\boldsymbol{e}_1 r, t)/u^3 = \langle u_1(\boldsymbol{x}, t)^2 u_1(\boldsymbol{x} + \boldsymbol{e}_1 r, t)\rangle / u^3 \tag{2.44}$$

Since $k(r, t)$ is an odd function of r, and because of continuity equation, $k'(0, t) = 0$, so its series expansion

$$k(r, t) = k'''(0, t) r^3/3! + k^V(0, t) r^5/5! + \cdots \tag{2.45}$$

The quantity $k'''(0, t)$, who determines $k(r, t)$ to leading order can be re-expressed as

$$u^3 k'''(0, t) = \langle (\frac{\partial u_1}{\partial x_1})^3 \rangle = S(\frac{\epsilon}{15\nu}) \tag{2.46}$$

Where

$$S \equiv \langle (\frac{\partial u_1}{\partial x_1})^3 \rangle / \langle (\frac{\partial u_1}{\partial x_1})^2 \rangle^{3/2} \tag{2.47}$$

S is the velocity-derivative skewness. Thus, there is a connection among this skewness and the transfer of energy between different scales which is involved in the energy cascade. In homogeneous isotropic turbulence, the skewness represents the rate of production of vorticity through vortex stretching, and the non-zero value arises from the non-linearity of the Navier-Stokes equations.

2.3.3.2 Further interpretation between velocity-derivative skewness and inter-scale energy transfer

Following Batchelor [1953]Lumley et al. [2007]Tavoularis et al. [1978] and Bos et al. [2012], the relation among velocity-derivative skewness and transfer of energy between different scales can be derived, details are presented in the 5.

Another form for the velocity-derivative skewness is

$$\lim_{r \to 0} S(r) = \frac{\langle (\partial u/\partial x)^3 \rangle}{\langle (\partial u/\partial x)^2 \rangle^{3/2}} \tag{2.48}$$

Using Eq.(20),Eq.(21) and Eq.(22), we have

$$\lim_{r \to 0} S(r) = \frac{\langle (\partial u/\partial x)^3 \rangle}{\langle (\partial u/\partial x)^2 \rangle^{3/2}} = -\frac{15^{3/2}}{35\sqrt{2}} \frac{\int \kappa^2 T(\kappa) d\kappa}{[\int \kappa^2 E(\kappa) d\kappa]^3} \tag{2.49}$$

The Eq. (2.49) shows that the velocity-derivative skewness is directly related to the inter-scale energy transfer and dissipation mechanism. Considering the situation when energy transfer and dissipation is balanced, we have

$$\int \kappa^2 T(\kappa) d\kappa \simeq \int 2\nu \kappa^4 E(\kappa) d\kappa \tag{2.50}$$

So that

$$\lim_{r \to 0} S(r) \simeq -\frac{15^{3/2}\sqrt{2}\nu}{35} \frac{\int \kappa^4 E(\kappa) d\kappa}{[\int \kappa^2 E(\kappa) d\kappa]^{3/2}} \tag{2.51}$$

Since $E(\kappa)$ depends on Reynolds number, thus, the velocity-derivative skewness becomes a function of the Reynolds number. For a turbulence flow at a certain
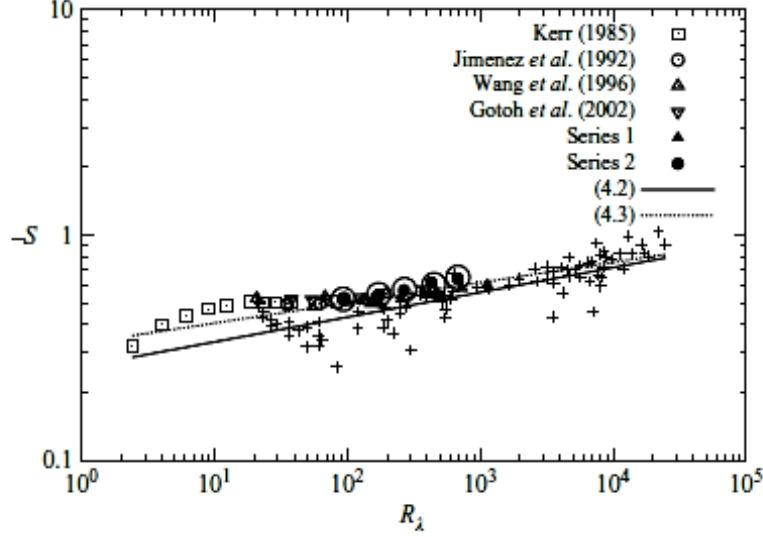
Figure 2.12: The velocity-derivative Skewness. + is from [Sreenivasan and Antonia, 1997]; Series 1 and 2 are from [Ishihara et al., 2007]; (4.2) comes from [Hill, 2002] and (4.3) comes from [Gylfason et al., 2004]

Reynolds number, when the process of energy cascade is established or when turbulence is fully developed, the transfer of energy from large scale to small scale is balanced to the dissipation rate at the smallest scale (Kolmogorov scale η), the velocity-derivative skewness should be non-zero, negative at certain level. Thus it may be seen as a criterion for determining if turbulence is fully developed.

2.3.4   The DNS and experimental data about the skewness

Experiment of Comte-Bellot and Craya [1965] gives a value of S_u (velocity-derivative skewness along streamwise direction) between -0.3 to -0.4 throughout the channel, except of -0.8 near the wall.

Measurements of the velocity-derivative skewness in homogeneous isotropic turbulence by Burattini et al. [2008] show that skewness is constant with the Reynolds number.

Based on the data at $Re_\lambda > 400$ (Re_λ is the Taylor scale Reynolds number)

of [Antonia et al., 1981], Hill [2002] proposed

$$S \sim -0.5(Re_\lambda/400)^{0.11} \simeq -0.26Re_\lambda^{0.11} \tag{2.52}$$

and according to experimental data of [Gylfason et al., 2004]

$$S \sim -0.33Re_\lambda^{0.09} \tag{2.53}$$

The DNS results of [Ishihara et al., 2007] show

$$S \sim -(0.32 \mp 0.02)Re_\lambda^{0.11\pm0.03} \tag{2.54}$$

Their results are shown in Fig. 2.12

Chapter 3

Validation on channel flow

In this chapter, the improved vortex method will be tested with a channel flow at a Reynolds number $Re_\tau = 395$, and then validate against a channel flow with a higher Reynolds number $Re_\tau = 590$. At first, a periodic LES calculation (with periodic boundary conditions) is carried out to provide reference data for the spatial evolving calculation with improved vortex method. Since the improved vortex method is a hybrid RANS/LES method, a RANS calculation is also conducted on the same channel to provide inlet mean profiles (mean velocity, mean turbulent kinetic energy and dissipation rate). Both the LES and RANS results will be used to optimize the parameters for the improved vortex method ($Re_\tau = 395$). Then the improved vortex method with optimized parameters will be applied to a channel flow with higher Reynolds number ($Re_\tau = 590$). Concerning the results, mean velocity and Reynolds stress profiles will be presented, as well as the friction coefficient throughout the channel. The relation between the development of turbulence and the velocity-derivative skewness along the streamwise direction will be analysed.

3.1 Parameter optimization

3.1.1 The channel flow periodic LES at $Re_\tau = 395$

The calculation is performed in a channel of $2\pi h \times 2h \times \pi h$ using a grid of $49 \times 89 \times 41$ points. Here, $h = 0.01m$ is the half channel height. The mesh is
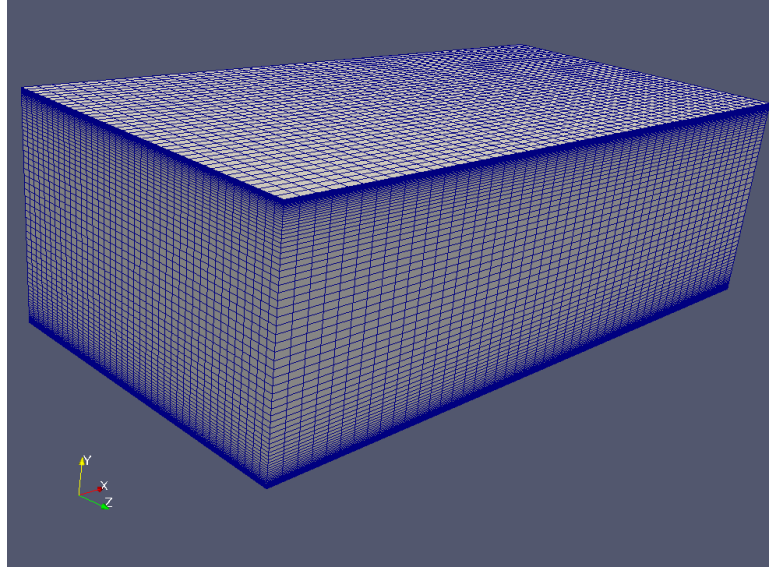
Figure 3.1: Mesh of calculation on channel flow at $Re_\tau = 395$

uniform in the streamwise direction (x-direction) and in the spanwise direction (z-direction), and follow a *tanh* form distribution in the wall-normal direction (y-direction), as shown in Fig. 3.1. The grid resolutions in wall units are $\Delta x^+ = 52$, $\Delta y^+ = 0.5$, $\Delta z^+ = 31$ in the streamwise, wall-normal and spanwise direction, respectively.

3.1.1.1 Initial and boundary conditions

The flow field is initialed with a Poiseuille velocity profile

$$u_x = U_0(1 - (y/h)^2) \tag{3.1}$$

$$u_y = u_z = 0 \tag{3.2}$$

with $U_0 = 20u_\tau$, $P = \rho U_0^2/(\gamma M^2)$ ($M = 0.2$ to accelerate the calculation), $\rho = 1.214 kg/m^3$, $\mu = 1.81 \times 10^{-5} kg/m/s$ and $u_\tau = 0.59 m/s$. These correspond to a Reynolds number $Re_\tau = 395$. According to [Moser et al., 1999], we have $U_0/u_\tau \sim 20$ at center of channel.

Periodic conditions are used in the streamwise and spanwise directions. The top and bottom sides of the channel are set as non-slip adiabatic walls.

To force the transition to turbulence, random perturbations are added to the flow field in all the three directions with an amplitude $0.02U_0(1 - (y/h)^2)$.

A source term S_{st} is added to the momentum equation in the x-direction in order to compensate the pressure drop caused by friction on the wall:

$$S_{st} = \frac{\rho u_\tau^2}{h} \tag{3.3}$$

3.1.1.2 Results

All results are normalized with the friction velocity u_τ and the half channel height h. The DNS results of Moin and Mahesh [1998] are compared to validate the reference periodic LES calculation.

Quality check of LES results

The LES convergence is checked with the help of probes. Two probes are placed at $y^+ = 7.7$ and $y^+ = 38.3$ to capture instantaneous velocities.

The instantaneous velocities recorded by the probe ($y^+ = 7.7$) with WALE model are shown in Fig. 3.2. The turbulent transition occurs around $t^+ = 4$ ($t^+ = \frac{u_\tau t}{h}$), and the flow field reaches fully turbulent state at about $t^+ = 6$. The collection of statistics is between $t^+ = 6.20$ and $t^+ = 14.75$. Considering the homogeneity in streamwise and in spanwise directions, there are in total 153600 samples collected within this time period.

Mean velocity profiles

The friction velocity u_τ is computed for each LES. The results are compared with the DNS friction velocity u_τ, as listed in Tab. 3.1. The WALE model shows a better prediction of u_τ than the SISM model. It slightly overestimate u_τ by 0.9%, while a 13.2% underestimation is reported by the SISM model.

The comparison of mean velocity profiles is shown in Fig. 3.3. Results are normalized by their computed friction velocities respectively. Both the LES achieve good agreements with the DNS results. In particular, the viscous sublayer is very
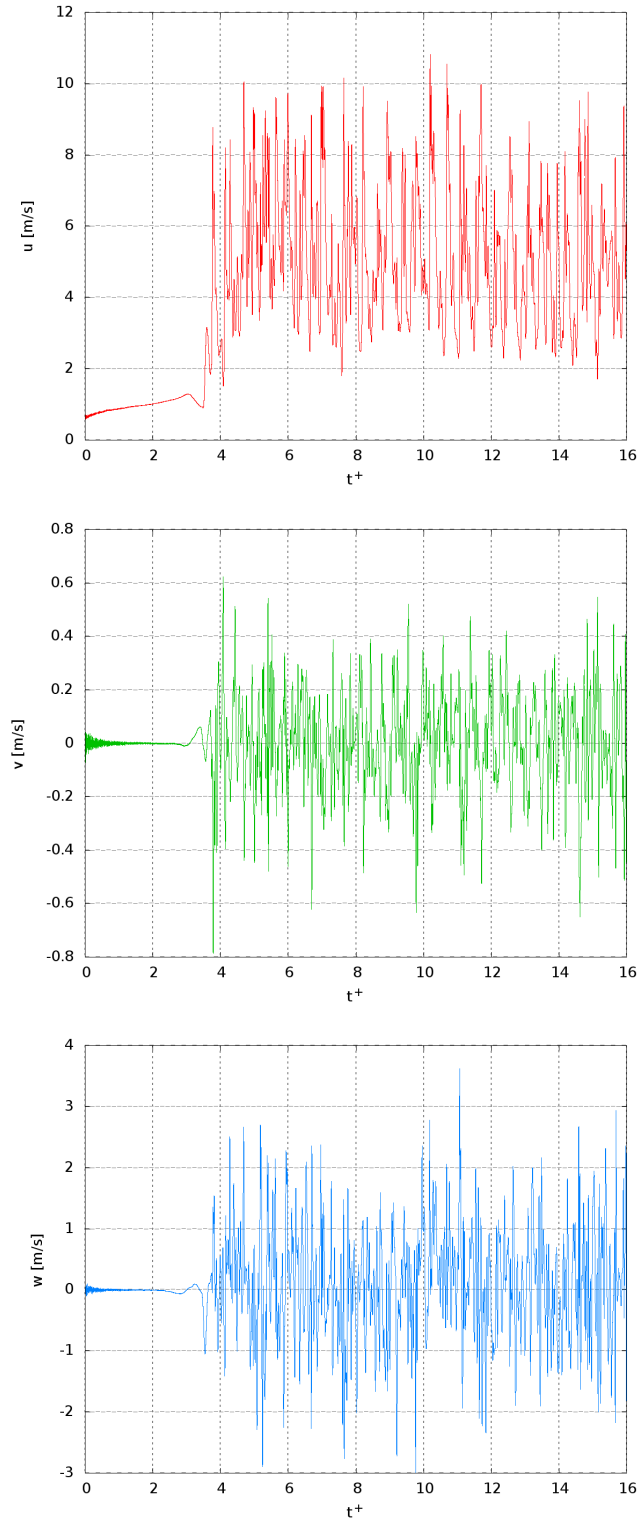
Figure 3.2: Velocity recorded by the probe at $y^+ = 7.7$ with the WALE model

54

	DNS	WALE	SISM
	0.590 m/s	0.595 m/s	0.512 m/s

Table 3.1: Friction velocity
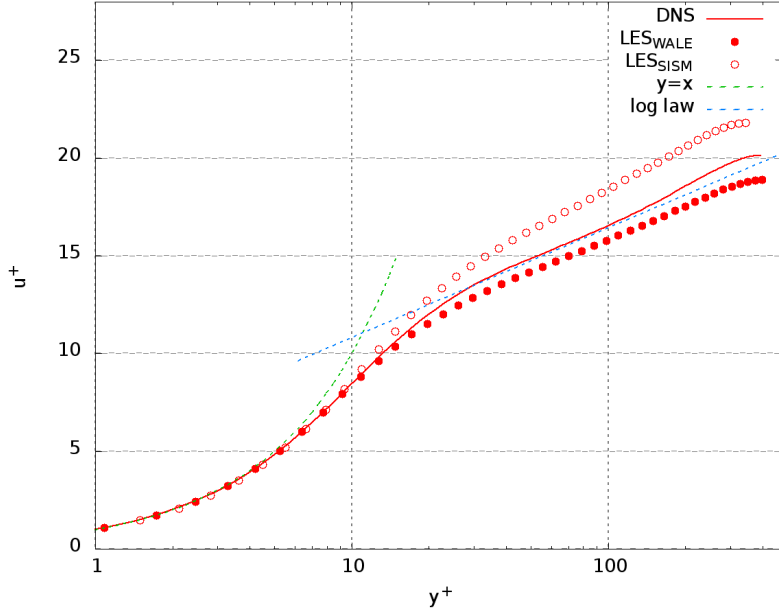
Figure 3.3: Comparison of mean velocity profiles

well captured by both LES. Discrepancies are seen in the log-law region. The WALE model gives a 5.5% underestimation of the mean velocity at the channel center, while this value is overestimated by 10.3% in the SISM results. This may be due to the underestimation of the friction velocity.

Reynolds stresses

A comparison of velocity fluctuations between the LES and DNS results is plotted in Fig. 3.4. The DNS inner peak of $\langle u'u' \rangle$ locates at $y^+ = 14.7$ with a peak value of about 7.5. The WALE model predicts the inner peak of $\langle u'u' \rangle$ at almost the same location, but with a 14.6% overestimation of the peak value. The inner peak of $\langle u'u' \rangle$ simulated by the SISM model lies further from the wall (at $y^+ = 18.4$)
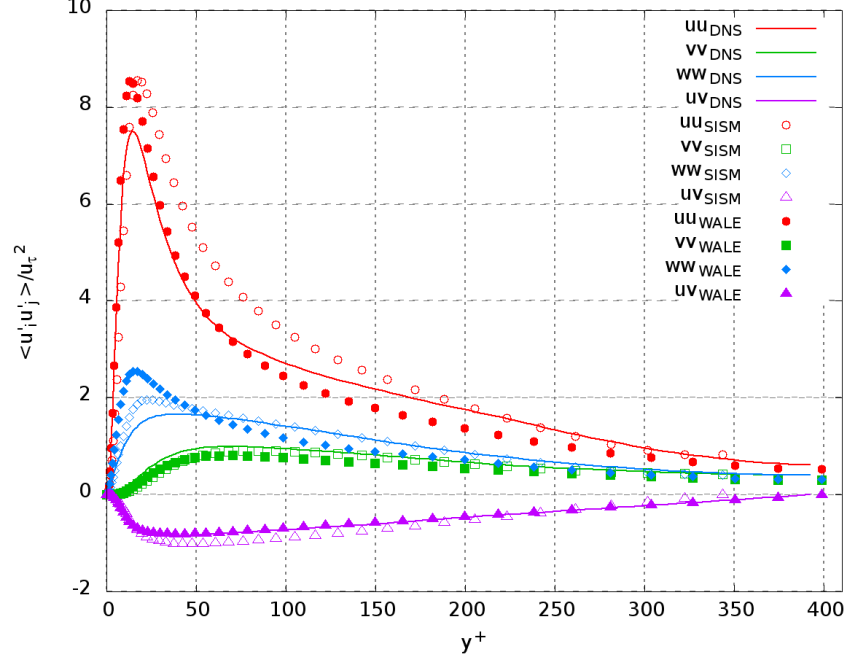
Figure 3.4: Comparison of Reynolds stresses

than the DNS, and its peak value is overestimated by 14.5%. Concerning the spanwise Reynolds stress $\langle w'w' \rangle$, the DNS shows a peak value of about 1.6 at $y^+ = 29.7$. Both the LES overestimate the peak value. The SISM model gives a better prediction in terms of the peak value and the peak location (18.7% overestimation at $y^+ = 22.0$) than the WALE model (62.5% overestimation at $y^+ = 15.6$). The profiles of $\langle v'v' \rangle$ and $\langle u'v' \rangle$ with the WALE model and SISM model both agree well with the DNS results. The inner peak of $\langle v'v' \rangle$ locates at $y^+ = 52.3$ and the extreme value of $\langle u'v' \rangle$ lies at about $y^+ = 27.2$. The LES underestimates $\langle v'v' \rangle$ by less then 10%. The WALE results agrees better with the DNS $\langle u'v' \rangle$ profile.

3.1.2 The channel flow RANS at $Re_\tau = 395$

The improved vortex method is a hybrid RANS/LES method, which requires profiles of mean velocity, turbulent kinetic energy and dissipation rate. Although these mean profiles can also be directly extracted from LES or DNS reference
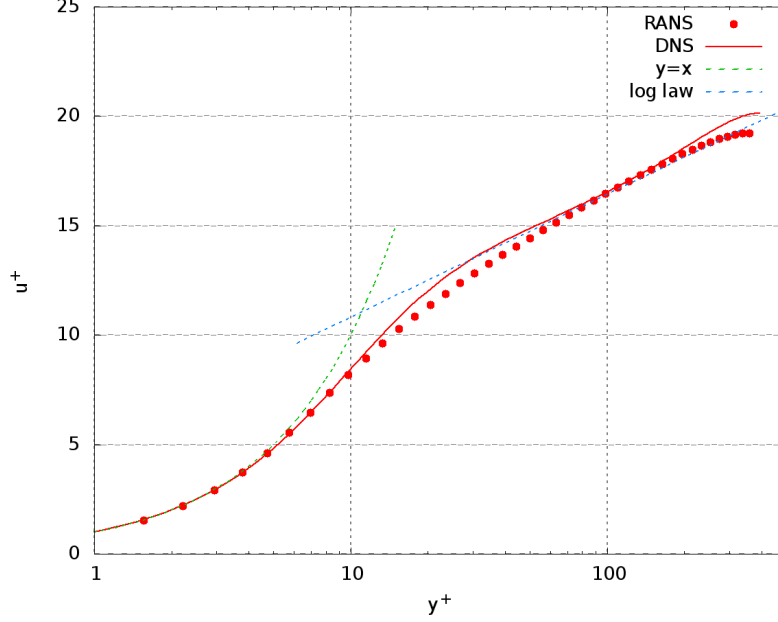
Figure 3.5: Mean velocity of RANS k-ω model with a reference DNS result

database, but RANS method can achieve a fast prediction. A RANS simulation is conducted here on the same channel used for the periodic LES. The standard *Wilcox k-ω* model is employed to close the RANS equations.

3.1.2.1 Results

All results are normalized in wall units (RANS $u_\tau = 0.535 m/s$, $h = 0.01 m$). The mean velocity obtained with the RANS is shown in Fig. 3.5, in comparison with the DNS results. The RANS results show a very good agreement with the DNS mean velocity profile. The mean kinetic energy profile of RANS is plotted with those of the DNS and LES, as shown in Fig. 3.6. The RANS underestimates the mean kinetic energy, compared with the periodic LES and the DNS. The peak value of k for RANS is about 2.6, locating at $y^+ = 33.5$. The LES shows a peak of 5.3 at $y^+ = 19.2$ and the DNS shows a peak of 4.6 at $y^+ = 17.0$. Although significant discrepancy is observed for RANS results, it provides correct trend of the k profile. Fig. 3.7 gives the profile of mean dissipation rate ϵ (normalized form $\epsilon^+ = \frac{\epsilon}{u_\tau^3/h}$). The profile shows a peak of 70 at $y^+ = 10$.
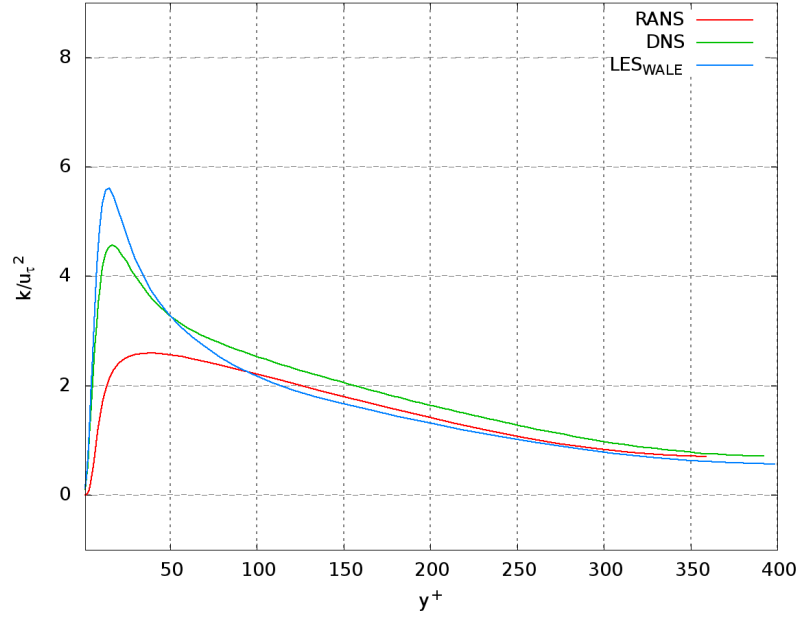
Figure 3.6: Mean kinetic energy of RANS k-ω model with a reference LES and DNS result
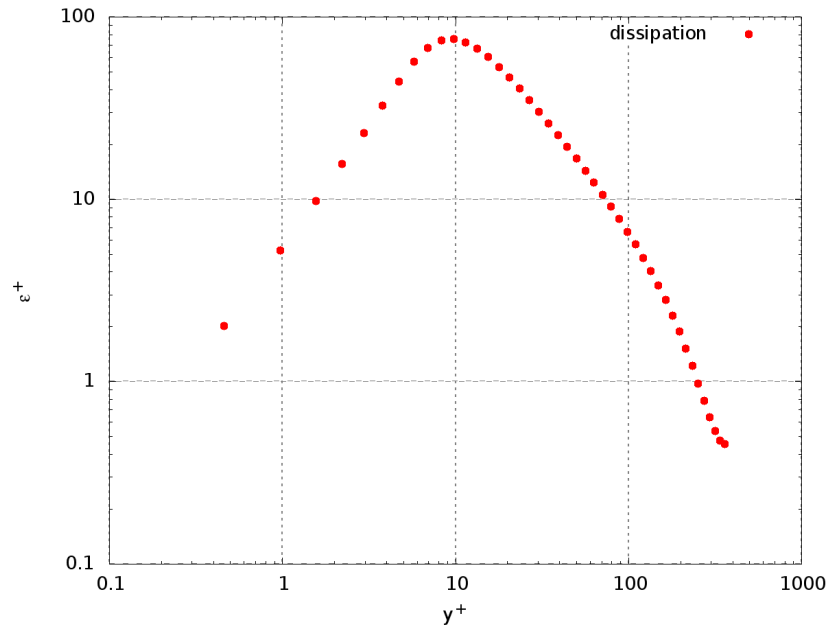
Figure 3.7: Mean dissipation rate ϵ of RANS k-ω model $\epsilon = C_\mu k\omega$ [Wilcox, 1988]

3.1.3 Parametric optimization of the improved vortex method

It's necessary to optimize the parameters of the improved vortex method, since they may vary for different flow types as vortex parameters are specified with local turbulent quantities. This subsection will present the parameter optimizing process of the parameters with a channel flow at a Reynolds number $Re_\tau = 395$.

3.1.3.1 Numerical methods

All the numerical tests in this subsection use the same numerical scheme, channel mesh as the set of the previous reference periodic LES at $Re_\tau = 395$. The SGS model used here and after is the WALE model.

Initial condition and Boundary condition

The calculation is initialized with the previous RANS results. The vortex method is used at inlet to generate an unsteady boundary condition. The mixed non-reflection pressure outlet condition is employed on the outlet boundary. A periodic boundary condition is applied to the spanswise boundaries. The end-walls on the top and bottom sides of the channel are set as non-slip adiabatic walls.

3.1.3.2 Parameters for the improved vortex method

A series of tests is carried out to optimize the parameters introduced in Tab. 2.1. By tuning the parameters of the improved vortex method, different kinds of unsteady fluctuations can be generated, this will result in different outlet flows. The values tested for the improved vortex method's parameters are summarized in Tab. 3.2. The pattern for vortex displacement can either be an enhanced random walk or a stochastic walk. The two types of vortex displacement are tested independently. The number of vortices injected at the inlet is 800, with image vortex to treat wall boundary condition [Sergent, 2002]. According to Sergent [2002], sensitivity of the method converges as the number of vortices increases. While too many vortices will slowdown the calculation. According to this thesis' work, a number of vortices around 1000 is recommended to generate an appropriate fluctuating velocity field.

Test cases	Radius σ C_1	Circulation Γ C_2	Lifetime τ C_3	Dispalcement ERW C_4	SW C_5
PO1	1	1	1	-	-
PO2	1/2	1	1	-	-
PO3	1/4	1	1	-	-
PO3+	1/16	1	1	-	-
PO4	1/4	1.2	1	-	-
PO5	1/4	1.6	1	-	-
PO6	1/4	1.2	0.1	1/16	-
PO7	1/4	1.2	10	1/16	-
PO8	1/4	1.2	100	1/16	-
PO9	1/4	1.2	1	1/8	-
PO10	1/4	1.2	1	1/16	-
PO11	1/4	1.2	1	1/32	-
PO12	1/4	1.2	10	-	1
PO13	1/4	1.2	10	-	5
PO14	1/4	1.2	10	-	50

Table 3.2: Simulation list of parameter optimization

The parameter optimization is carried out as follows. The radius and the circulation are studied first. Fixing the optimized coefficients for radius and circulation, the next studies on the enhanced random walk and lifetime are carried out at the same time. At last, the pattern of stochastic walk is tested with the optimized radius, circulation and lifetime. The value chosen for C_5 in test PO13 correspond to the reference value in [Pope, 2001].

3.1.3.3   Results and discussions

As a synthetic turbulence approach, the improved vortex method generates velocity fluctuations based on mean profiles ($\langle \vec{u} \rangle$, k, ϵ). The mean profiles are obtained from the previous RANS simulation, while 2D fluctuations at the inlet plane are generated by the present improved vortex method with 800 vortices.
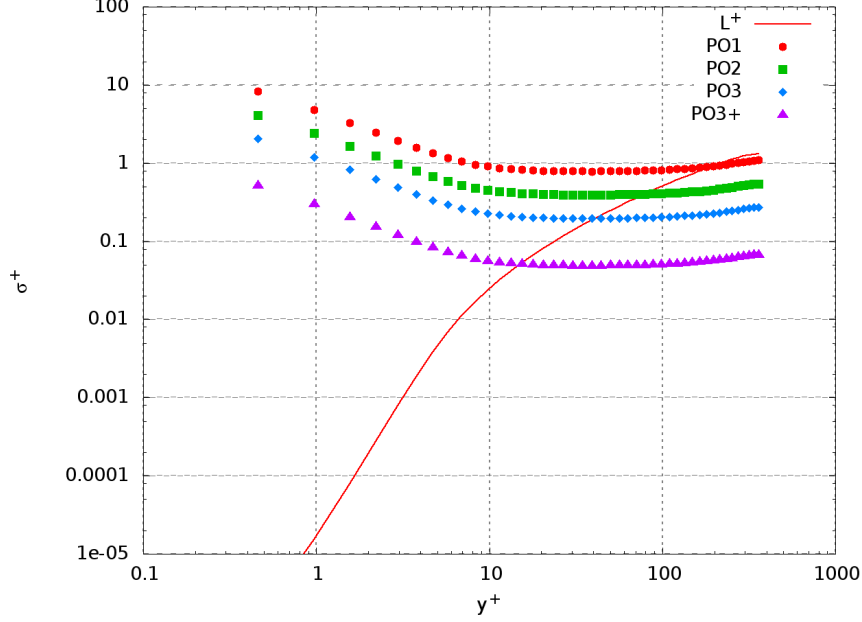
Figure 3.8: Comparison of radius σ^+ of PO1, PO2, PO3 and PO3+ with energy-containing scale L^+

The optimizing process and the related results will be presented and discussed.

Radius

The test cases concerning the vortex radius are PO1, PO2, PO3 and PO3+ in Tab. 3.2. The radius coefficient C_1 reduces gradually from PO1 to PO3+, suggesting that the vortex radius decrease from PO1 to PO3+, as shown in Fig. 3.8. Compared with the curve of energy-containing scale L^+, radius of PO3 agrees better with L^+ in the range of interest ($y^+ = 10$ to $y^+ = 100$). The inlet mean velocity profile is the same for all cases, as plotted in Fig. 3.9, which comes directly from the previous RANS results.

While their velocity fluctuations prescribed by the different vortex radius are different at inlet, which are shown in Fig. 3.10 and Fig. 3.11. The improved vortex method only generates 2D perturbations within the inlet plane, therefore the streamwise Reynolds normal stresses $\langle u'u' \rangle$ and the shear stresses $\langle u'v' \rangle$ are 0. The profiles of the other two Reynolds normal stresses are clearly visible.
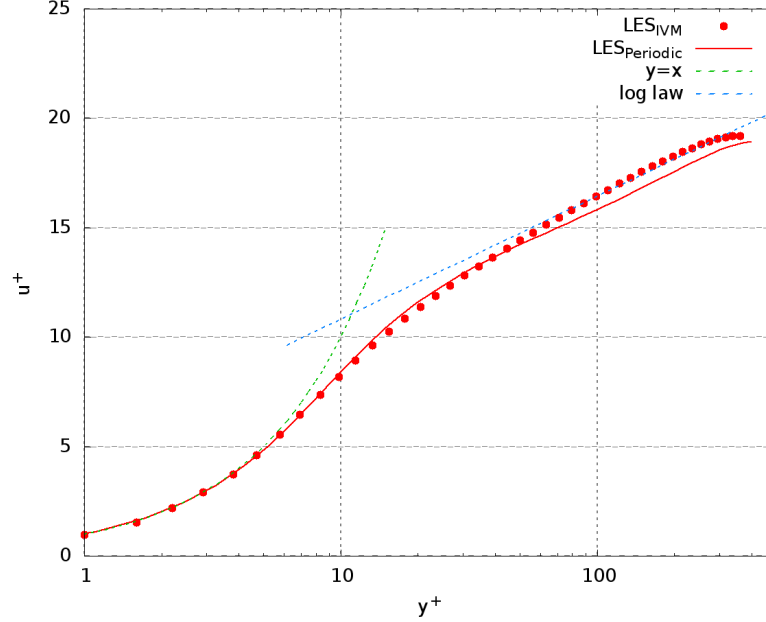
Figure 3.9: Mean velocity profiles at inlet $x/h = 0$: symbol, LES with improved vortex method (IVM); line, reference periodic LES

For PO1, only the Reynolds normal stresses $\langle w'w' \rangle$ have a visible peak with a comparable amplitude to that of the reference periodic LES. But the peak location is far from the reference periodic LES results. Halving the vortex radius (PO2), the $\langle w'w' \rangle$ peak increase in amplitude and the peak location moves towards the wall. A $\langle v'v' \rangle$ hump appears, and shows a similar extreme value with the reference periodic LES results. By further reducing the vortex radius (PO3 and PO3+), the $\langle w'w' \rangle$ peak location gets even closer to the reference periodic LES, while its peak value grows to nearly twice (PO3) of the reference periodic LES one. A similar trend is observed for the Reynolds normal stress $\langle v'v' \rangle$. This agrees with the results of Sergent [2002] that the radius σ has a notable influence on the position of the peak of the fluctuations; the bigger the vortices, the further away from the wall the peak locates.

Fig. 3.12 plots the evolution of friction coefficient c_f for all the three cases. The coefficient of friction c_f gives an indicator of how well-developed the mean
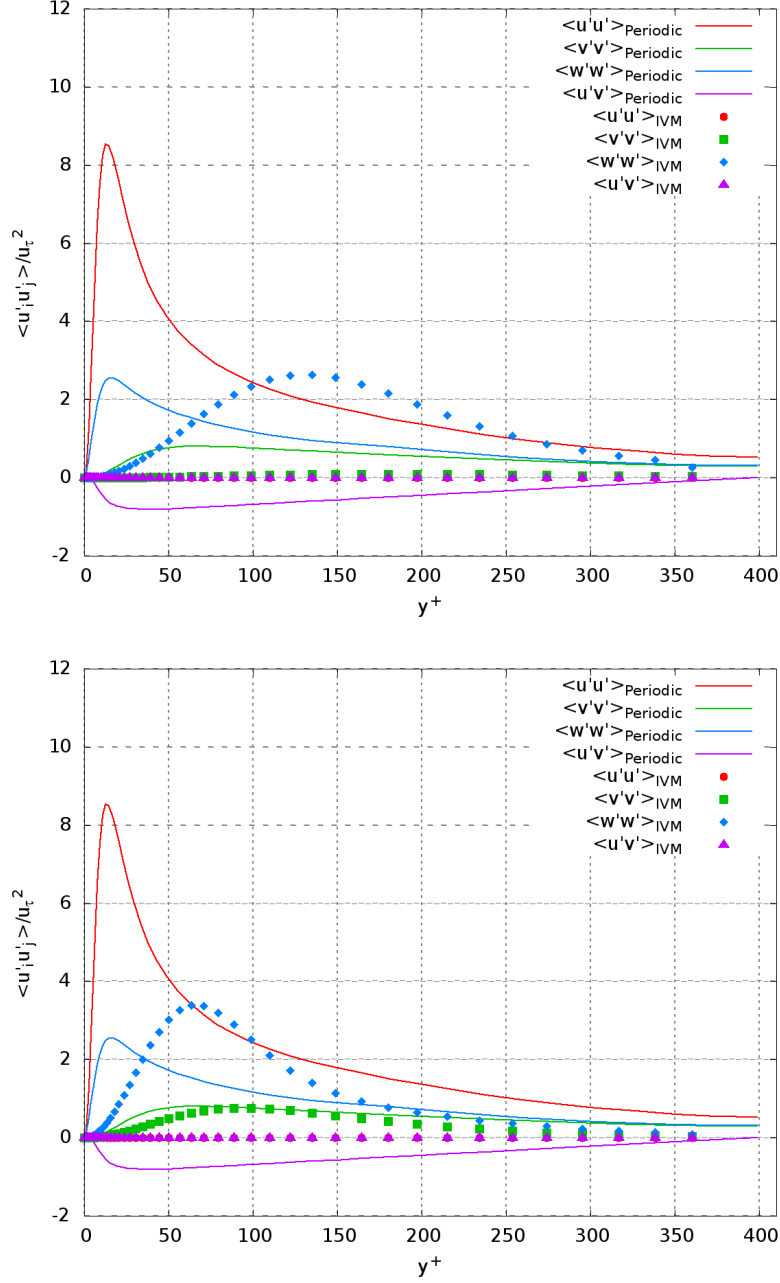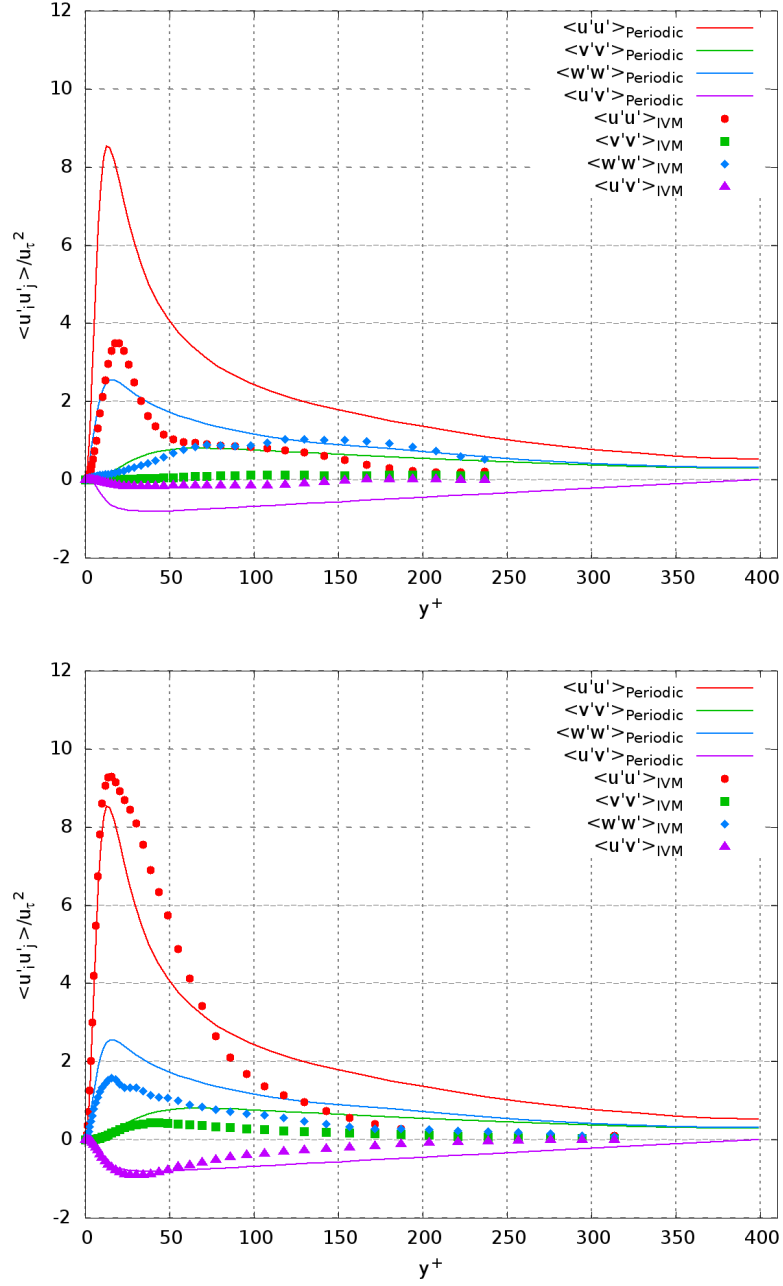
Figure 3.10: Reynolds stresses at inlet $x/h = 0$ of PO1 (top) and PO2 (bottom): symbol, LES with improved vortex method; line, reference periodic LES
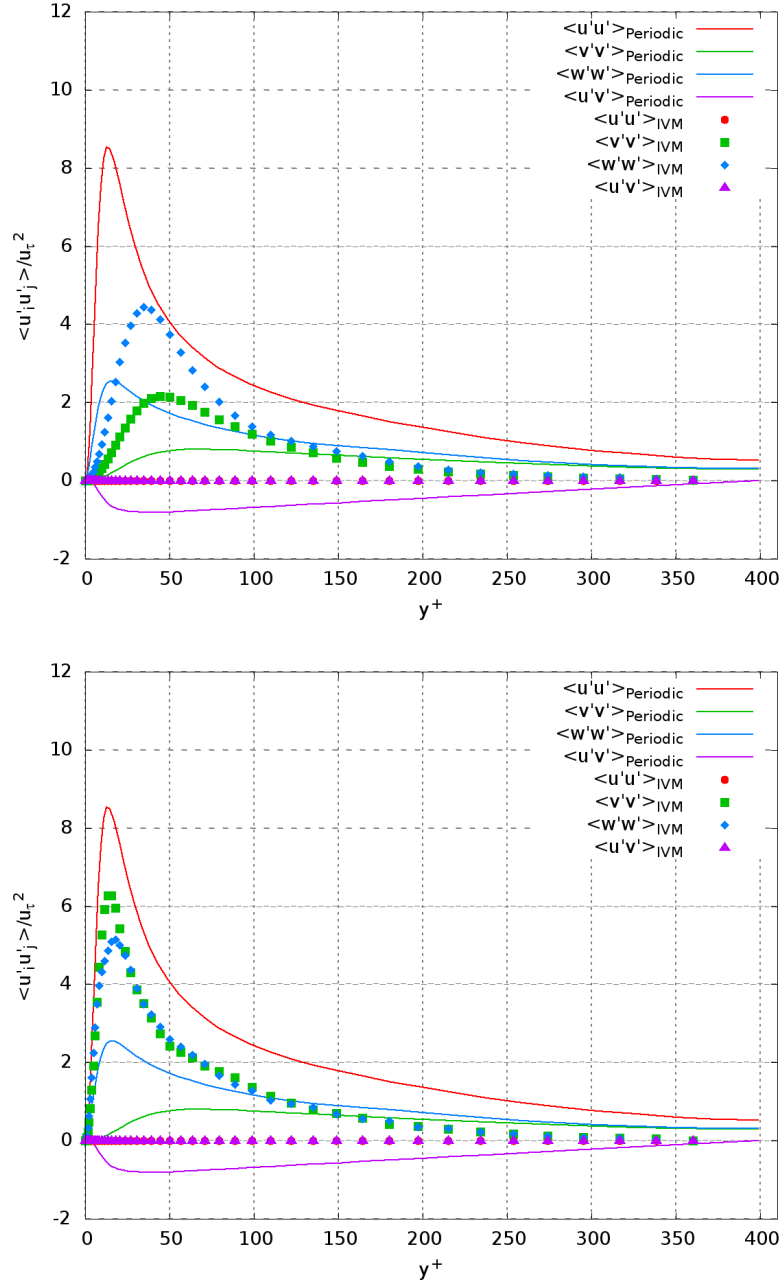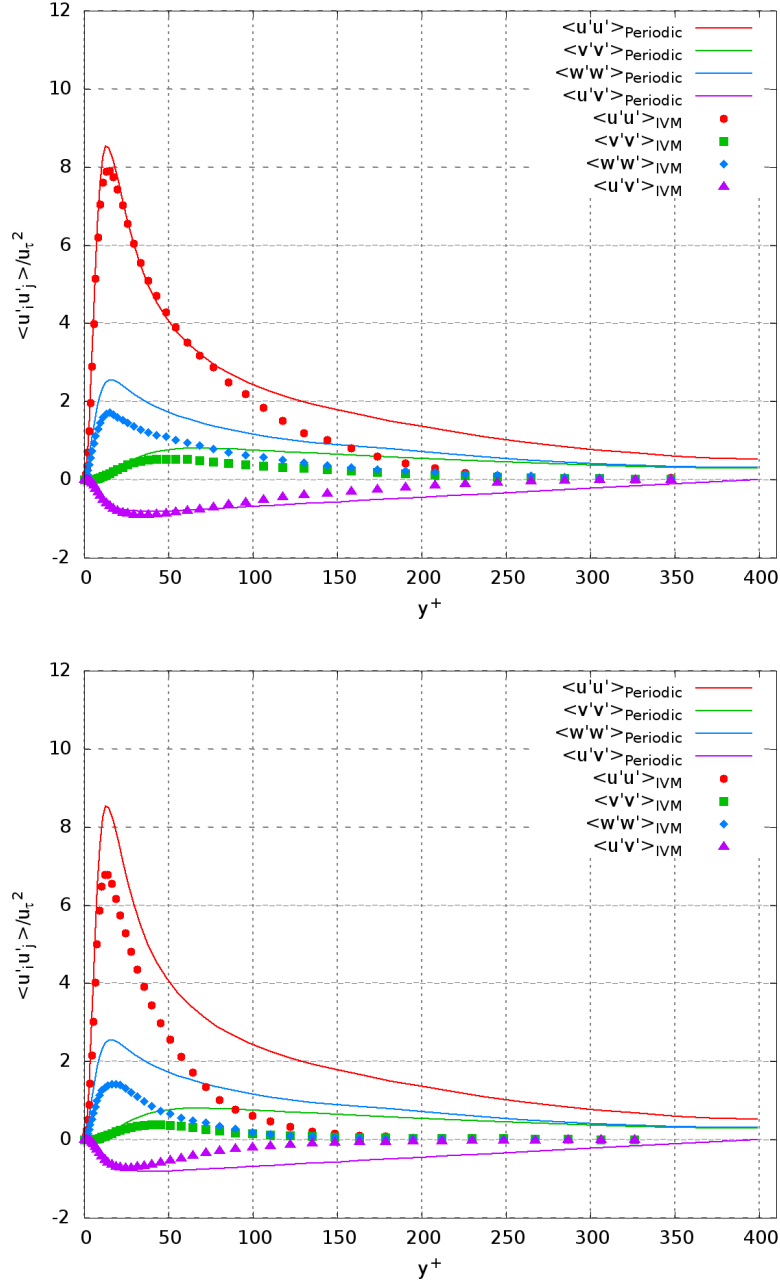
Figure 3.11: Reynolds stresses at inlet $x/h = 0$ of PO3 (top) and PO3+ (bottom): symbol, LES with improved vortex method; line, reference periodic LES
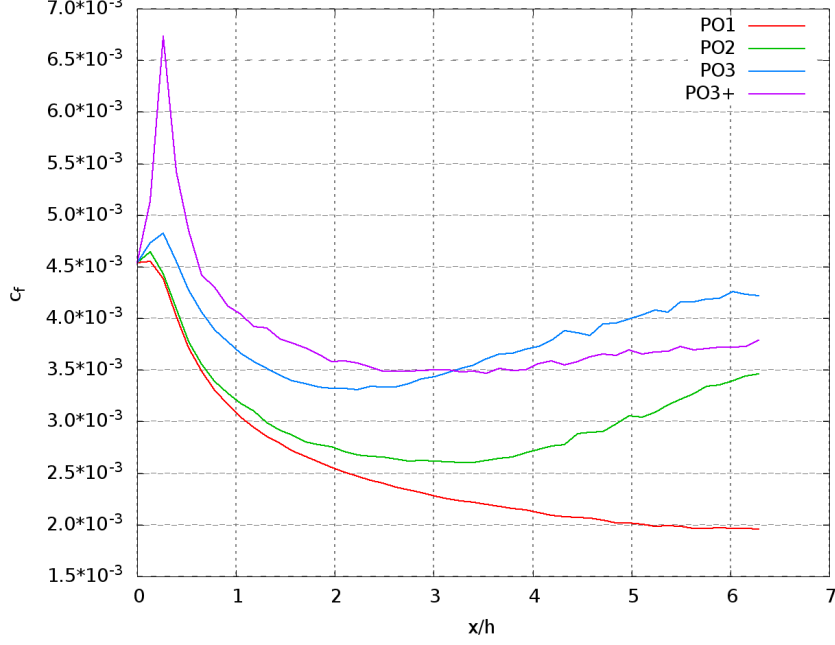
Figure 3.12: Evolution of friction coefficient c_f of PO1, PO2, PO3 and PO3+

velocity profile is. The friction coefficient c_f is defined as

$$c_f = 2(u_\tau/U_0)^2 \tag{3.4}$$

Where $U_0 = 11.25 m/s$ is the centreline velocity of the reference periodic LES. For the case PO1, the friction coefficient drops continuously from inlet to outlet, which means that the flow relaminarize. Similar result is obtained by PO3+, of which the radius sizes are the smallest. Therefore, too big or too small vortices are unfavourable to generate turbulence. For the other two cases PO2 and PO3, the friction coefficient drops till about half the channel length, and then recover back. The case with small vortices (PO3) which corresponds better to the energy-containing scale, achieve a better recovery of the friction coefficient at outlet.

The mean velocity profiles can be scrutinized in Fig. 3.13 and Fig. 3.14. The best prediction is obtained by PO3. For PO1 and PO2, the bigger the vortices are imposed at inlet, the larger the errors are observed at outlet. For PO3+, with the smallest vortices imposed, error is more pronounced in comparison with result of PO3.
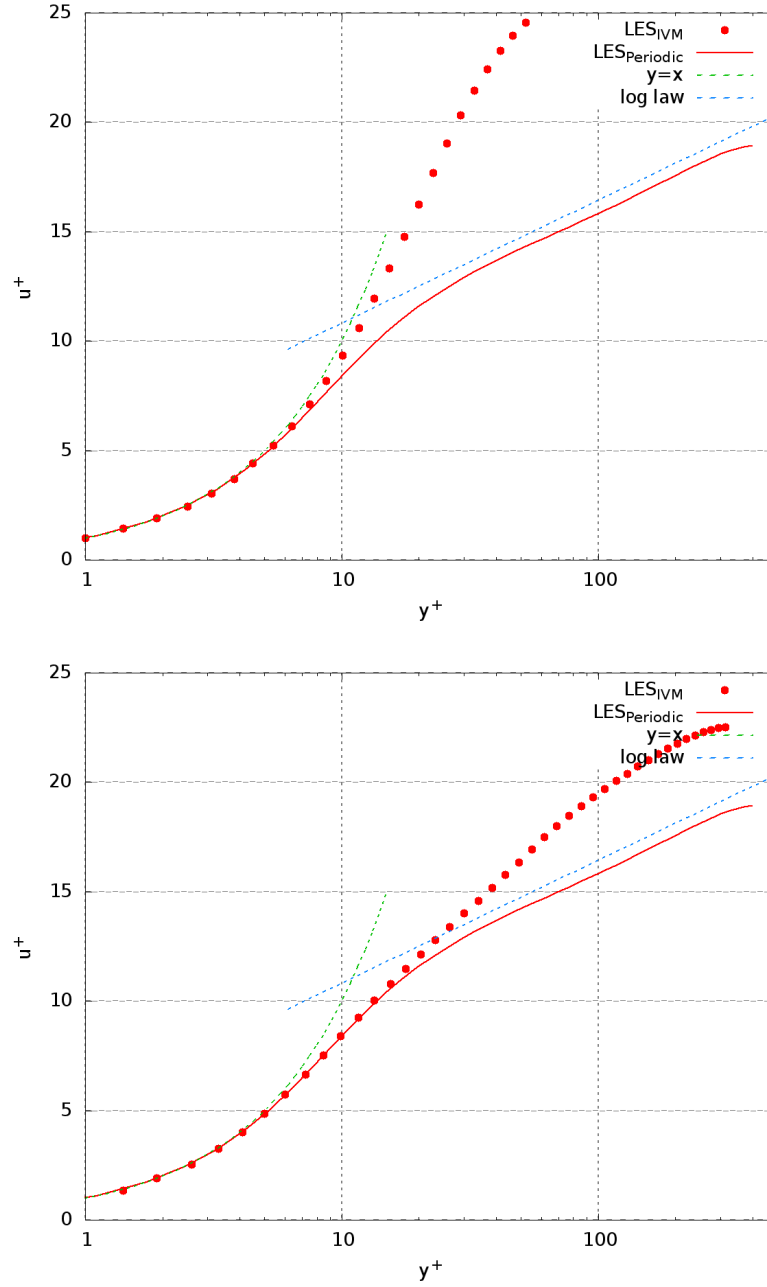
Figure 3.13: Mean velocity profiles at outlet $x/h = 2\pi$ of PO1 (top) and PO2 (bottom): symbol, LES with improved vortex method; line, reference periodic LES
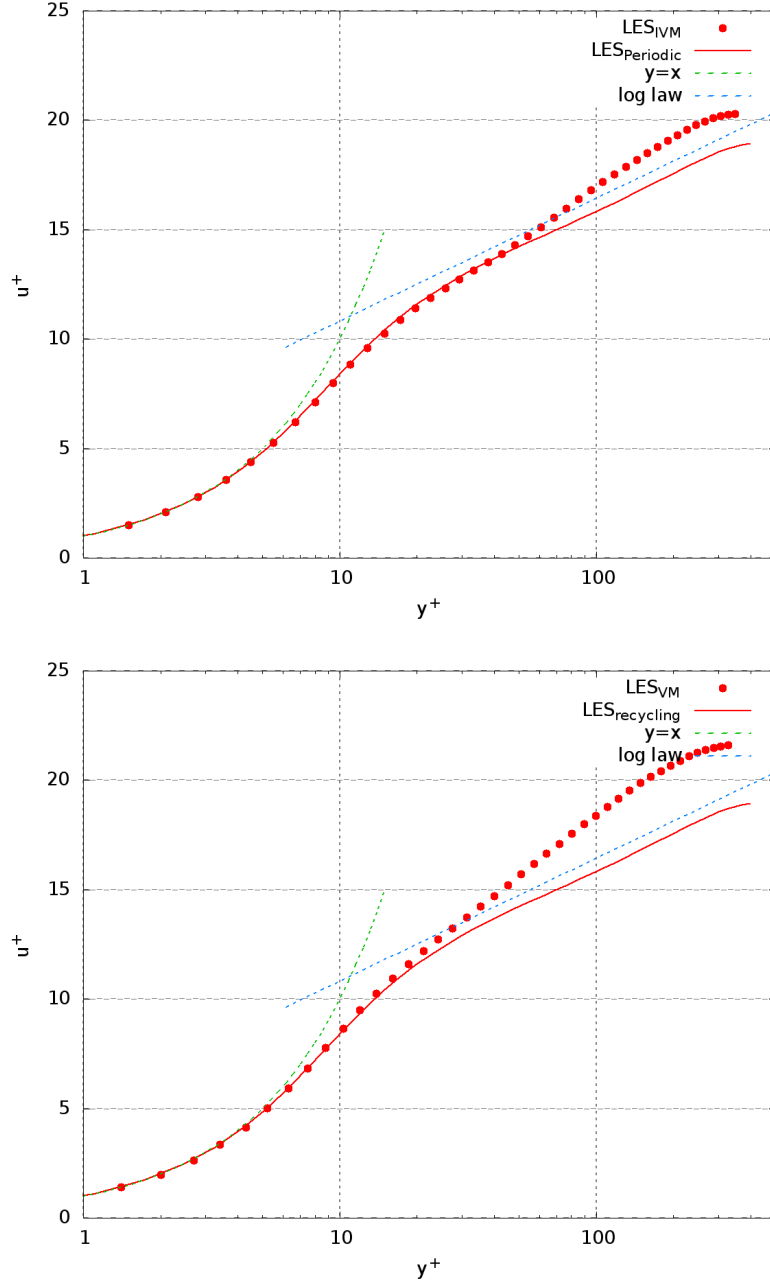
Figure 3.14: Mean velocity profiles at outlet $x/h = 2\pi$ of PO3 (top) and PO3+ (bottom): symbol, LES with improved vortex method; line, reference periodic LES

Figure 3.15: Reynolds stresses at outlet $x/h = 2\pi$ of PO1 (top) and PO2 (bottom): symbol, LES with improved vortex method; line, reference periodic LES
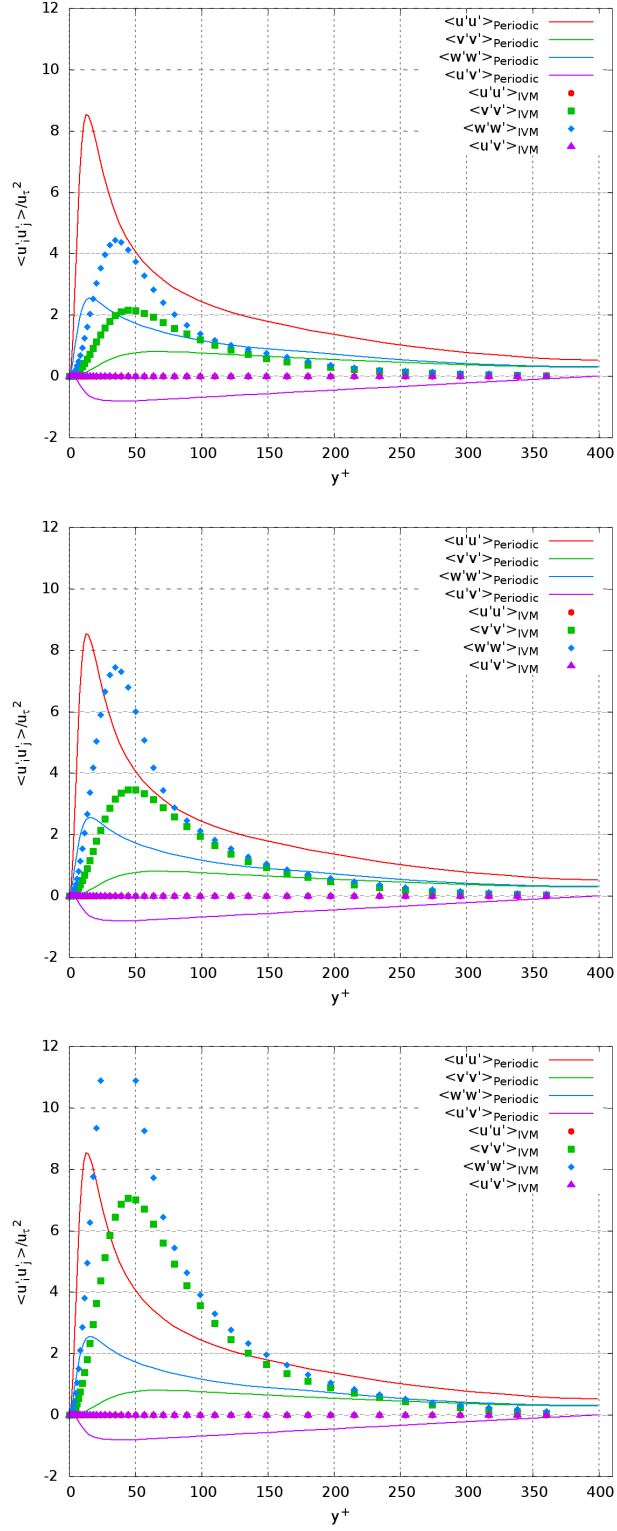
Figure 3.16: Reynolds stresses at outlet $x/h = 2\pi$ of PO3 (top) and PO3+ (bottom): symbol, LES with improved vortex method; line, reference periodic LES
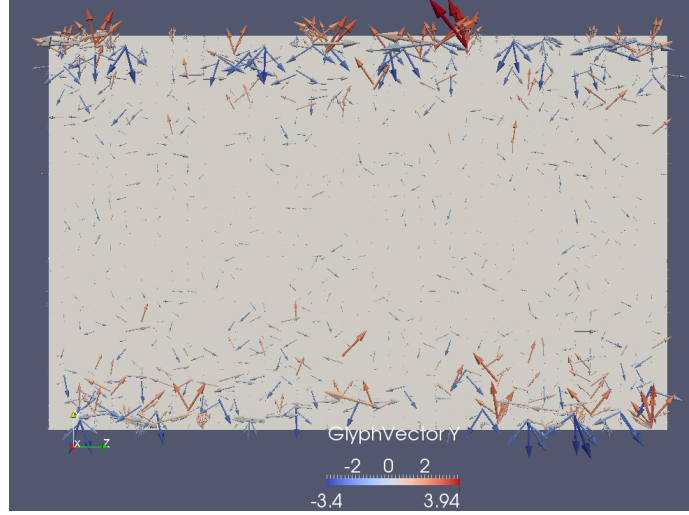
Figure 3.17: 2D instantaneous velocity field obtained at inlet with $C_1 = 1/40$

The comparison of Reynolds stresses at outlet are drawn in Fig. 3.15 and Fig. 3.16. Again, the case PO3 achieves the best prediction of the Reynolds stresses than the cases with appropriate sizes of vortices, although some discrepancies are observed.

One major difference between original vortex method of Sergent [2002] and improved vortex method is that Sergent [2002] uses a separate equation to generate the streamwise direction fluctuations which are uncorrelated with other components generated by vortex, while improved vortex method generates only the 2D components (normal to streamwise direction) by vortices and the streamwise fluctuating component is induced naturally through the mechanism of N-S equations. Thus all three fluctuating components are correlated, but the development to real turbulence is expected to be effective which is the aim of parameters vortex lifetime and displacement, and will be studied with test cases later.

Further tests are also carried out by further decreasing the size of vortex radius, but very small vortex (e.g., $C_1 = 1/40$) can hardly be resolved, resulting in inappropriate structured fluctuations, as shown in Fig. 3.17.

To conclude, the case PO3 achieves best prediction in terms of the mean velocity profiles and Reynolds stress at outlet. Thus, the first vortex parameter, radius coefficient C_1 is fixed at 1/4. The size of the vortices should be comparable

to the energy-containing scale. According to our tests in channel flow $Re_\tau = 395$, the acceptable range of C_1 is about $1/8 < C_1 < 1/3$. But the vortices cannot be too small, since very small vortices can hardly be resolved and may generate exceed fluctuations.

Circulation

The test cases concerning the vortex circulation are PO3, PO4 and PO5 in Tab. 3.2. The circulation coefficient C_2 increases gradually from PO3 to PO5, suggesting that the circulation is more and more amplified from PO3 to PO5. The velocity fluctuations prescribed by different circulation coefficient are different at inlet, as plotted in Fig. 3.18. 2D perturbations are clearly obtained for all these three cases. For PO3, the $\langle v'v' \rangle$ peak location lies at $y^+ = 45.0$, which is nearer to the wall compared with the reference periodic LES ($y^+ = 84.6$). Its peak value (2.2) is about 2.4 times of the reference periodic LES result (0.9). The $\langle w'w' \rangle$ peak location lies at $y^+ = 35.9$, which is further away from the wall compared with the reference periodic LES ($y^+ = 22.4$). Its peak value (4.5) is about 2.3 of the reference periodic LES result (2.0). As amplifying the circulation by 1.2 (PO4), the peak locations of $\langle v'v' \rangle$ and $\langle w'w' \rangle$ stay the same as PO3. But the peak value of $\langle v'v' \rangle$ is 3.5, about 3.9 times of the reference periodic LES result. The peak value of $\langle w'w' \rangle$ is 7.5, about 3.8 times of the reference periodic LES result. More amplifying the circulation by 1.6 (PO5). The peak value of $\langle v'v' \rangle$ is 7.1, growing to 7.9 times of the reference periodic LES result, while a peak value of 13.7 is obtained for $\langle w'w' \rangle$ (6.9 times of the reference periodic LES result).

Fig. 3.19 shows the evolution of friction coefficient for all the three cases. A common behaviour is shared by all the three cases: the friction coefficient increase then drops initially and recover to a value at outlet. The drop and recovery rate of PO4 is faster then that of PO3, while is slower than that of PO5. But at outlet, the friction coefficient of PO4 can recover back to its initial value of inlet, while the the friction coefficient of PO5 is overestimated and underestimation is observed for PO3, compared with each initial value at inlet.

The mean velocity profiles are shown in Fig. 3.20. The better predictions are obtained by PO4 and PO5. For PO3, without any amplification of the circula-

Figure 3.18: Reynolds stresses at inlet $x/h = 0$ of PO3 (top), PO4(mid), PO5 (bottom): symbol, LES with improved vortex method; line, reference periodic LES
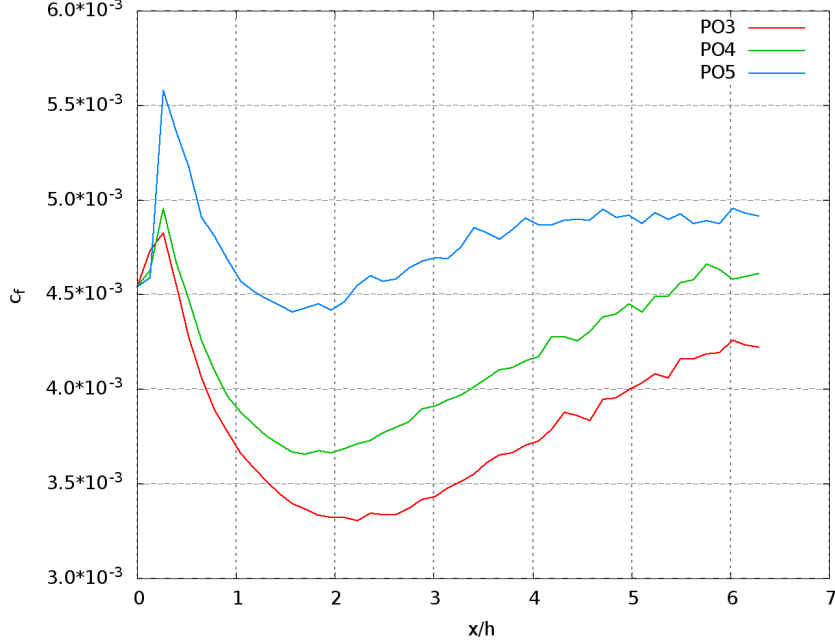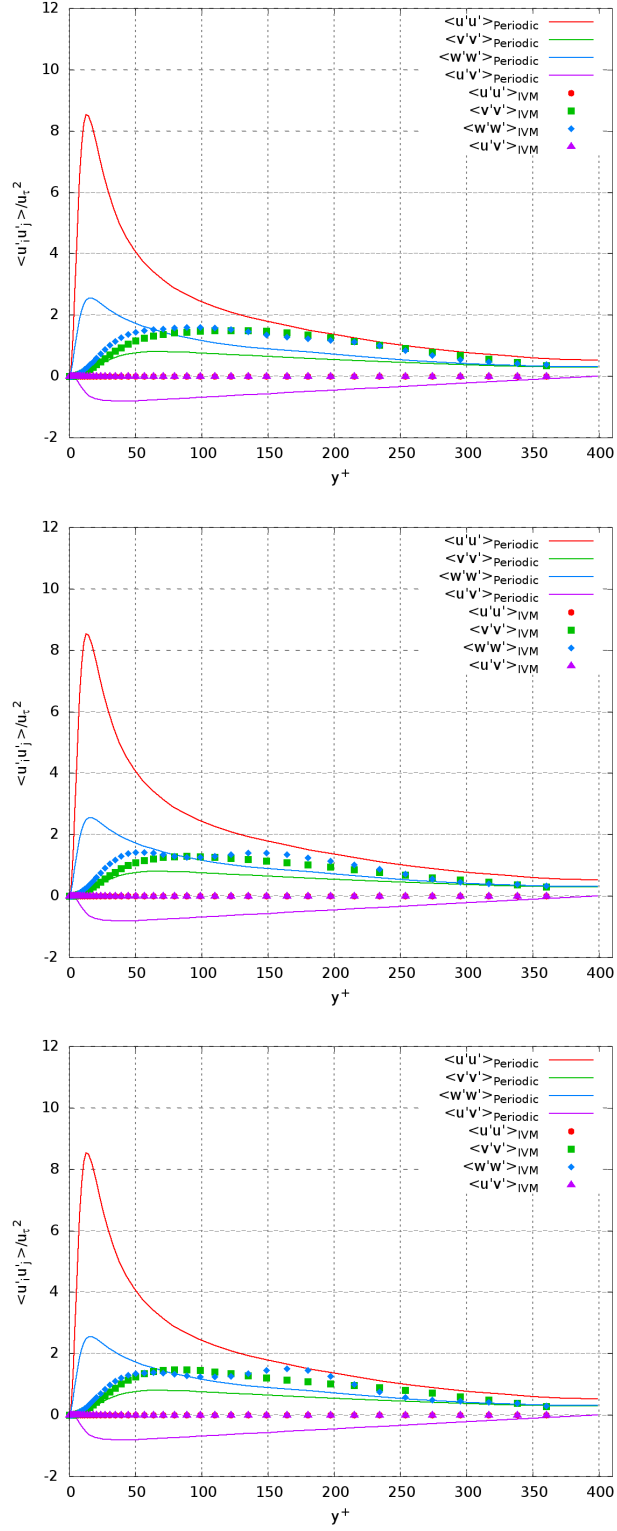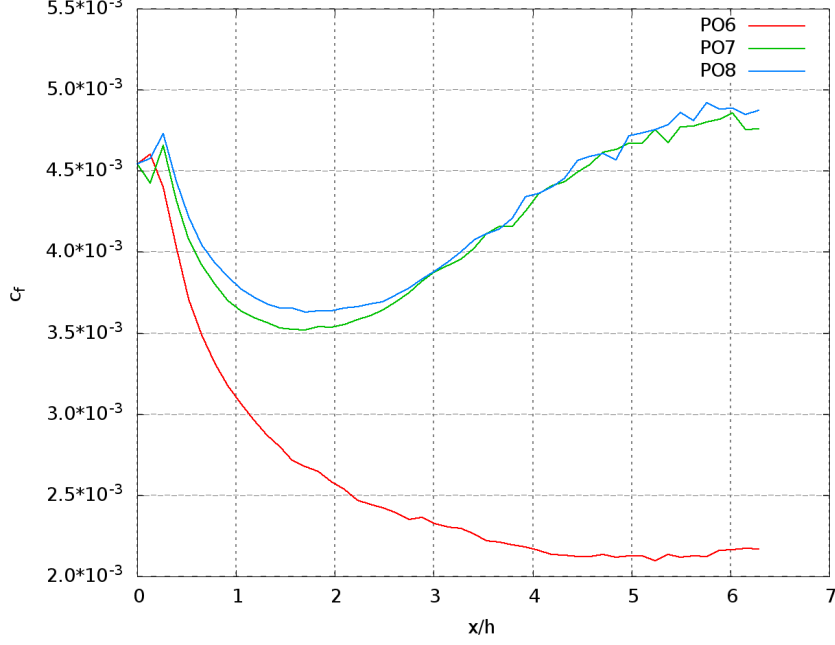
Figure 3.19: Evolution of friction coefficient c_f of PO3, PO4 and PO5

tion, larger error is predicted in the center of the channel. While PO4 slightly overestimates the mean velocity in the center of the channel and PO5 slightly underestimates it. The comparison of Reynolds stresses are drawn in Fig. 3.21. The cases PO5 and PO4 give best prediction of the Reynolds stresses than the case without any amplification (PO3).

In conclusion, the case PO4 achieve best prediction in terms of the friction coefficient, the mean velocity profiles and Reynolds stress at outlet. Even though the case PO5 seems to achieve best result, but, again, to avoid exceed fluctuations generated, the amplification factor for circulation cannot be chosen too big. Thus, the second vortex parameter, circulation coefficient C_2 is fixed at 1.2. The energy of generated fluctuations should be comparable to local turbulent kinetic energy.

Lifetime

The test cases concerning the vortex lifetime are PO6, PO7 and PO8 in Tab. 3.2. The lifetime coefficient C_3 increases gradually from PO6 to PO8, meaning that lifetime of vortex is longer from PO6 to PO8. The velocity fluctuations prescribed
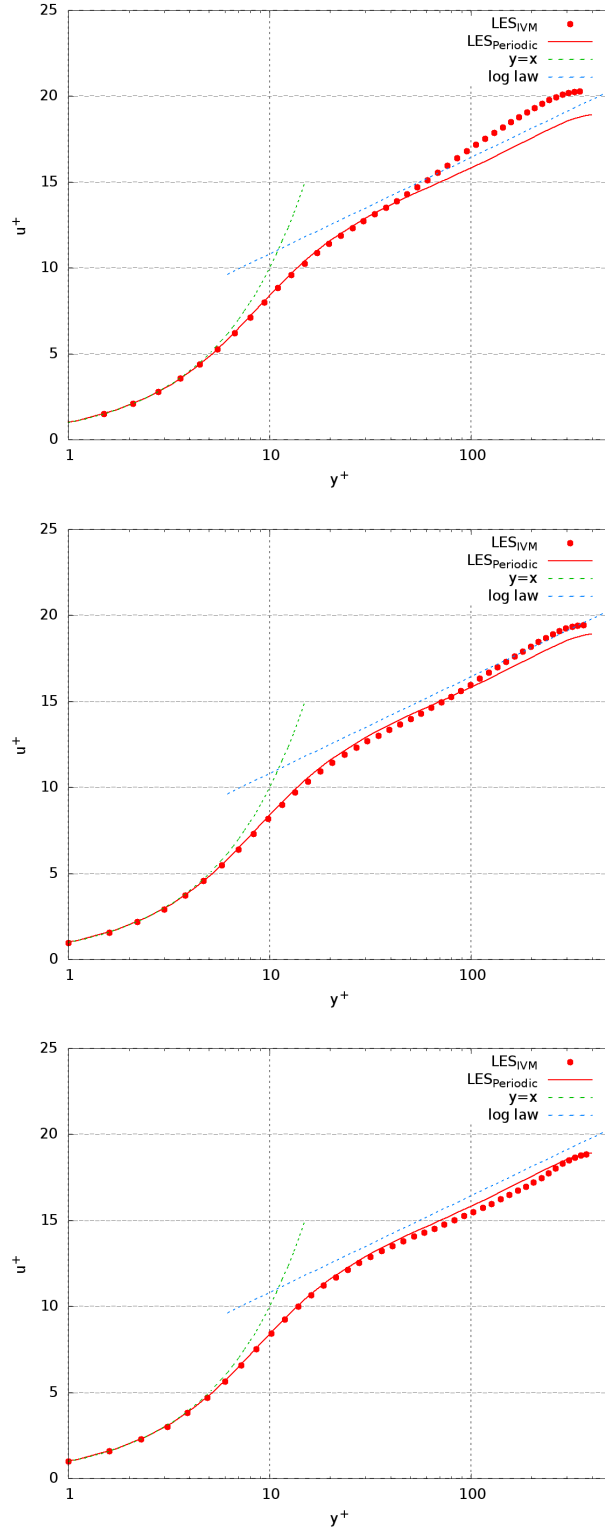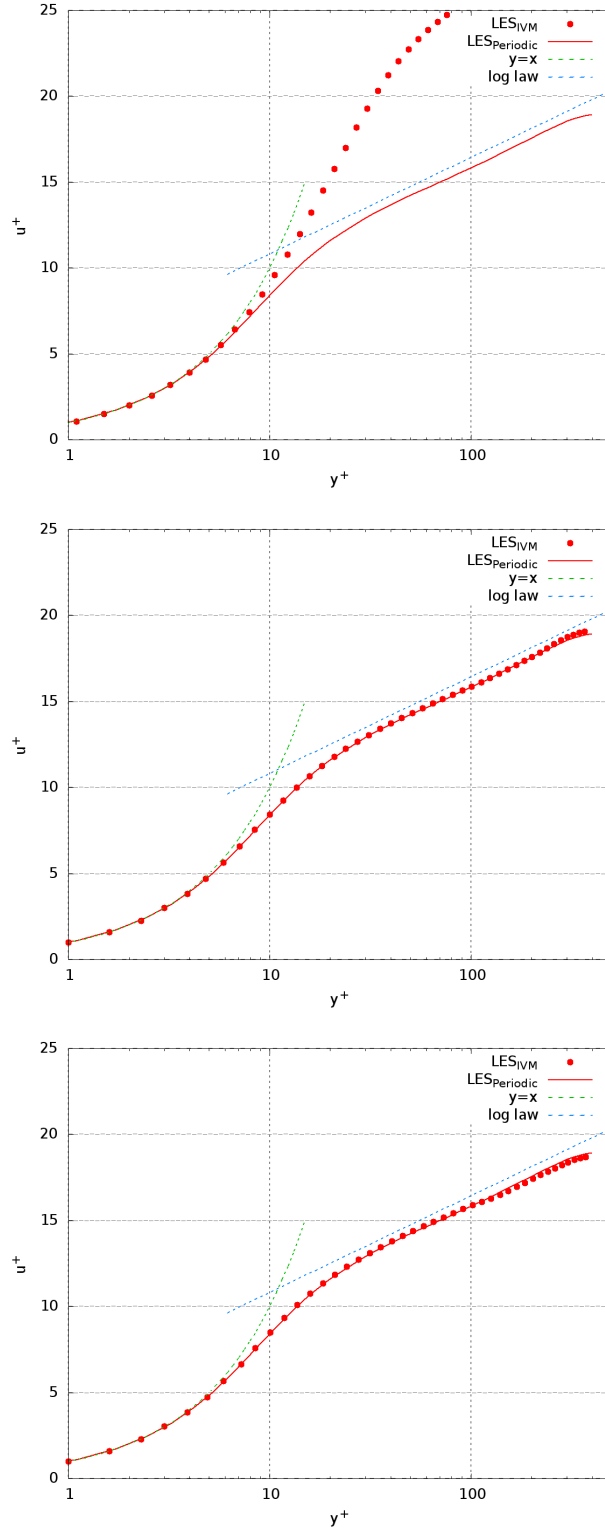
Figure 3.20: Mean velocity profiles at outlet $x/h = 2\pi$ of PO3 (top), PO4(mid), PO5 (bottom): symbol, LES with improved vortex method; line, reference periodic LES
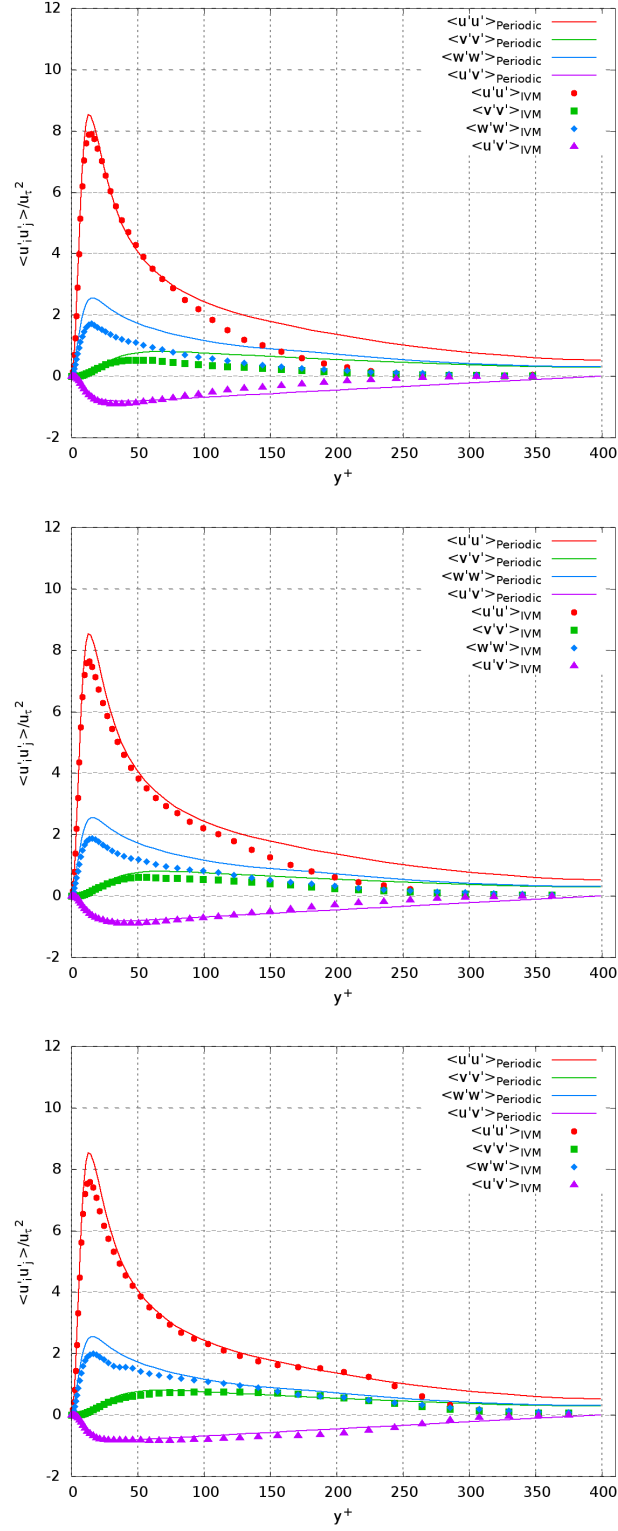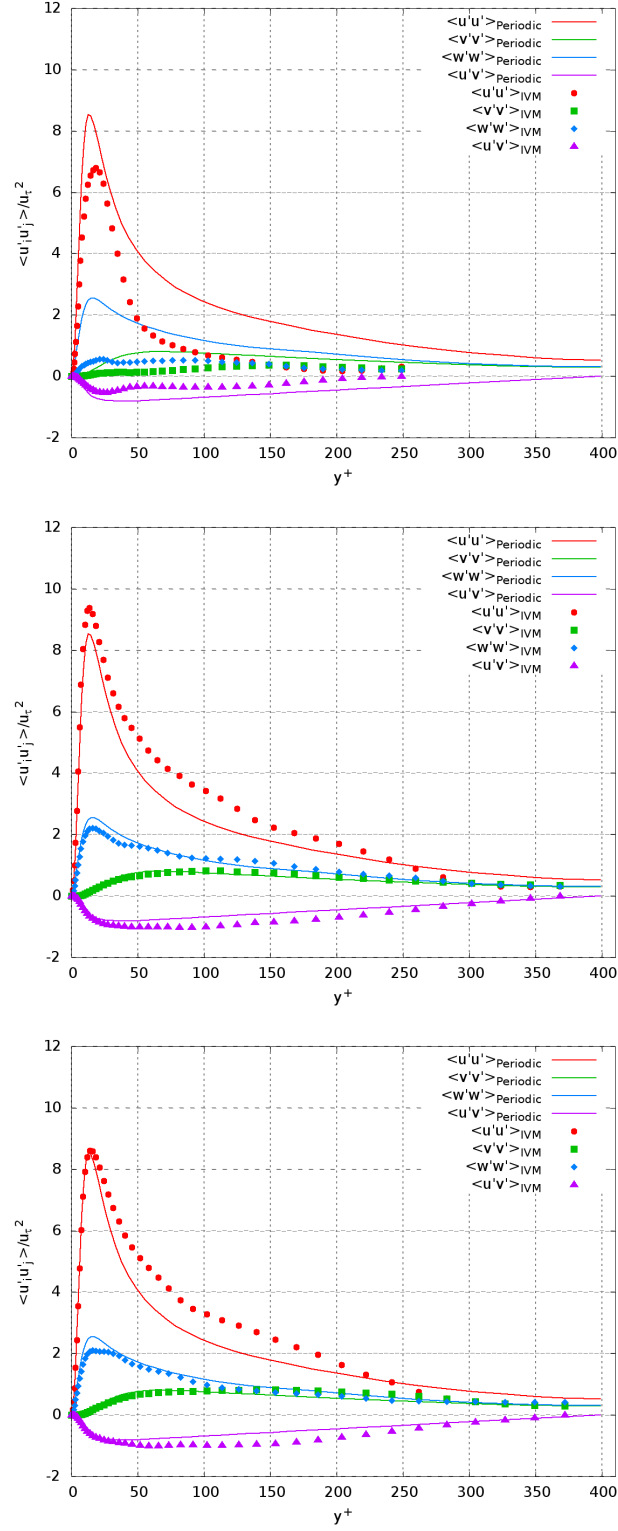
Figure 3.21: Reynolds stresses at outlet $x/h = 2\pi$ of PO3 (top), PO4(mid), PO5 (bottom): symbol, LES with improved vortex method; line, reference periodic LES

Figure 3.22: Reynolds stresses at inlet $x/h = 0$ of PO6 (top), PO7(mid), PO8 (bottom): symbol, LES with improved vortex method; line, reference periodic LES

Figure 3.23: Evolution of friction coefficient c_f of PO6, PO7 and PO8

at inlet are shown in Fig. 3.22. A general behaviour is shared by all the three cases, the profile of $\langle v'v' \rangle$ and the one of $\langle w'w' \rangle$ superposes with each other, suggesting that the velocity fluctuations are 2D isotropic which is compatible with Eq. (2.7). The peak value is about 1.6 and locates at $y^+ = 88.5$. No big differences are observed of the Reynolds stress profiles at inlet for all the three cases.

Fig. 3.23 plots the evolution of friction coefficient. For the case PO6, the friction coefficient drops continuously downstream from inlet, and the flow become totally laminar at outlet. Therefore, too small lifetime coefficient is unfavorable to generate turbulence. For the other two cases, the friction coefficients drop initially and reach to a minimum value ($\simeq 3.6 \times 10^{-3}$) at about $x/h = 1.8$, then it increase to a value which is almost the same level as the inlet $\simeq 4.7 \times 10^{-3}$, suggesting that a development from laminar flow to turbulent flow.

The mean velocity profiles are shown in Fig. 3.24. Better predictions are obtained by PO7 and PO8. For PO6, the lifetime coefficient is the lowest, flow become totally laminar, leading to larger error of the mean velocity at outlet.

Figure 3.24: Mean velocity profiles at outlet $x/h = 2\pi$ of PO6 (top), PO7(mid), PO8 (bottom): symbol, LES with improved vortex method; line, reference periodic LES

Figure 3.25: Reynolds stresses at outlet $x/h = 2\pi$ of PO6 (top), PO7(mid), PO8 (bottom): symbol, LES with improved vortex method; line, reference periodic LES

The comparison of Reynolds stresses are drawn in Fig. 3.25. The cases PO7 and PO8 achieve better prediction of the Reynolds stresses than the cases with shorter vortex lifetime. Even though some discrepancies are observed at center of the channel.

In conclusion, the results of PO6 suggest that the vortex lifetime cannot be so short. The results of PO7 and PO8 are quite satisfied. The flow field obtained at outlet is almost fully developed. This is also due to the employment of enhanced random walk for these three cases, since the lifetime and enhanced random walk are implemented into the improved vortex method at the same time. While the parametric optimization is separated. As for the vortex lifetime, it is recommended to chose a value larger than the local turbulent time scale k/ϵ ($\tau \simeq 10k/\epsilon$ according to our tests). Here, the third vortex parameter, lifetime coefficient is fixed at 10.

Enhanced random walk

The test cases concerning the vortex enhanced random walk are PO9, PO10 and PO11 in Tab. 3.2. The enhanced random walk coefficient C_4 decreases from PO9 to PO11, meaning that the walking step length decreases from PO9 to PO11. The velocity fluctuations prescribed at inlet are shown in Fig. 3.26. The Reynolds stress profiles are almost the same at inlet. Perturbations are 2D, and $\langle v'v' \rangle$ superposes with $\langle w'w' \rangle$. The peak value is about 1.4 and locates at $y^+ = 99.0$. The humps are smooth, similar to the $\langle v'v' \rangle$ of the reference periodic LES.

Fig. 3.27 plots the evolution of friction coefficient for all the three cases studied. For all the three cases, the friction coefficient drops first from inlet, then increases and almost stabilize at some value at outlet. For PO9, with longer walking step length, the initial drop is deeper and the recovery is slower. At outlet, the friction coefficient is underestimated, compared with its inlet value. While for PO10 and PO11, with smaller walking step length, the drop reaches to a minimum value of about 3.15×10^{-3} at $x/h = 2$, and the recovery to the steady value of about 4.70×10^{-3} at about $x/h = 6$. This suggest that the flow become fully developed before reaching the outlet.

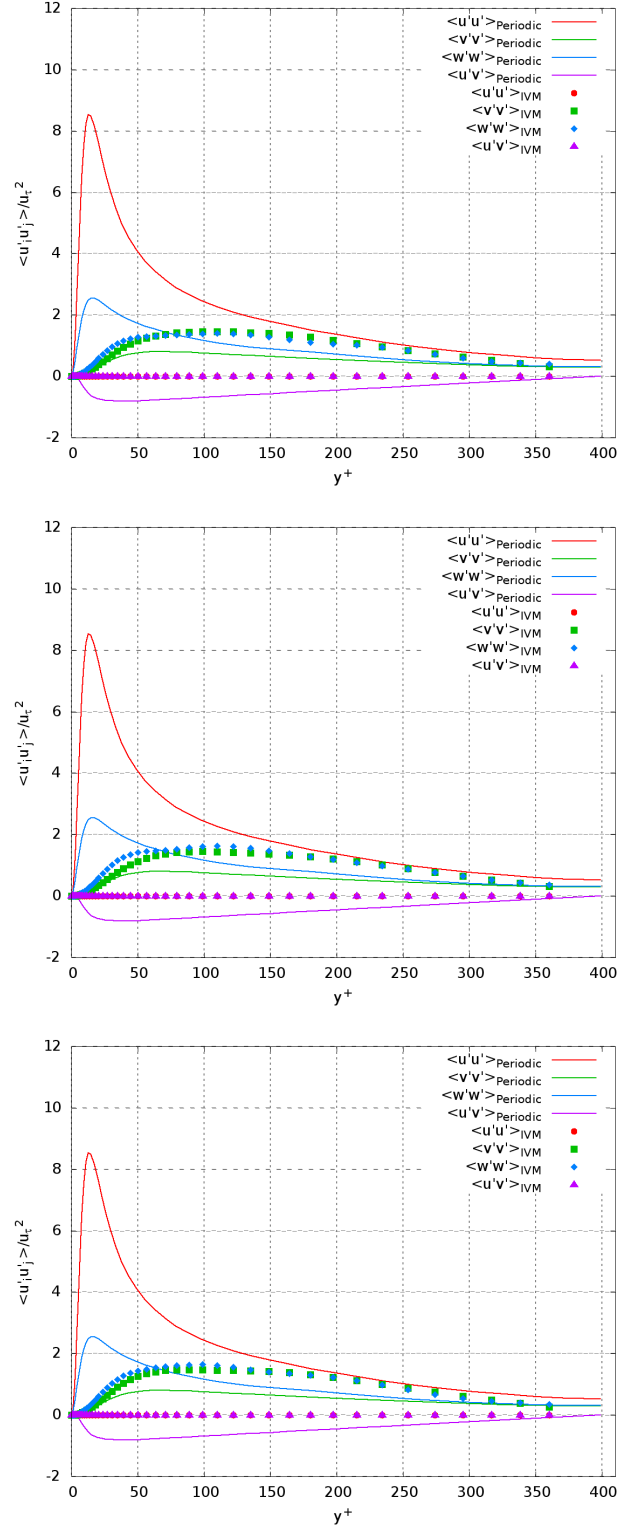The mean velocity profiles at outlet are shown in Fig. 3.28. Better predictions

Figure 3.26: Reynolds stresses at inlet $x/h = 0$ of PO9 (top), PO10(mid), PO11 (bottom): symbol, LES with improved vortex method; line, reference periodic LES
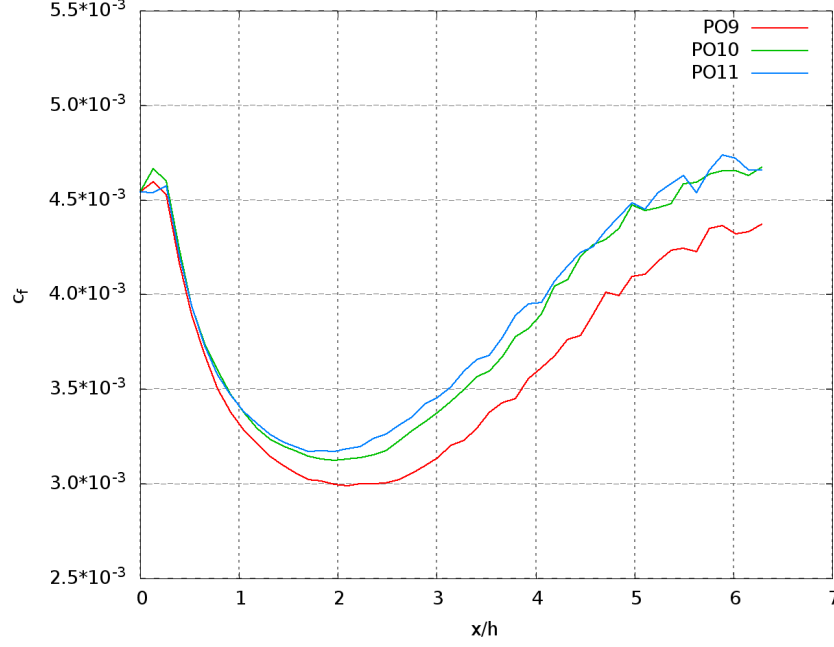
Figure 3.27: Evolution of friction coefficient c_f of PO9, PO10 and PO11

are obtained by PO10 and PO11. For PO9, the walking step length is longer. Larger discrepancy of the mean velocity profile is observed in the center of the channel, compared with the reference periodic LES mean velocity profile. While for PO10 and PO11, shorter walking step length are imposed, the mean velocity at outlet is only slightly overestimated in the center of the channel (less than 5%). The comparison of Reynolds stresses at outlet are drawn in Fig. 3.29. Again, better predictions are obtained with cases PO10 and PO11. Near the wall, the behaviour of velocity fluctuations are very well predicted, compared with the reference periodic LES results. While in the center of the channel, small discrepancies are observed.

To conclude, the cases PO10 and PO11 achieve better predictions in terms of the friction coefficient, the mean and Reynolds stress profiles at outlet. Thus, the walking step length are suggested to be set small. It is based on the vortex radius, while the latter is comparable to a energy-containing lengthscale. Numerical experiments performed here recommend to chose a walking step length as 1/16 of the vortex radius. Thus, the fourth vortex parameter, enhanced random walk
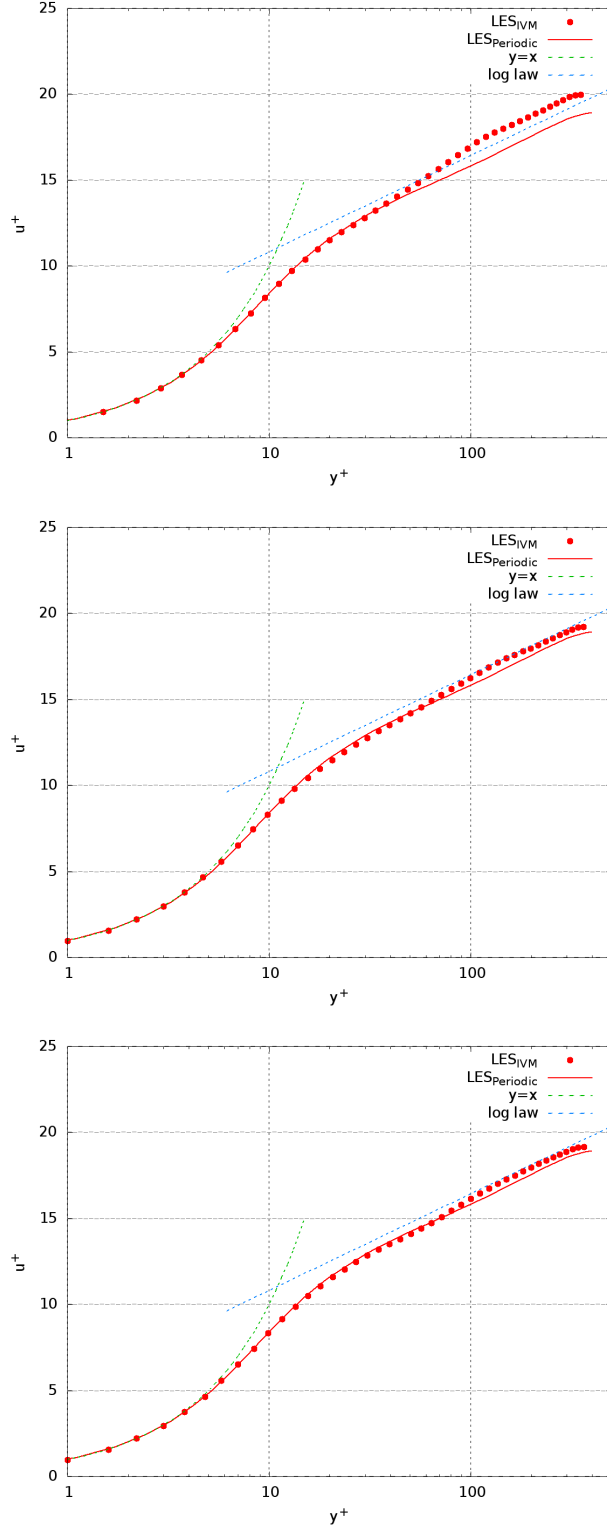
Figure 3.28: Mean velocity profiles at outlet $x/h = 2\pi$ of PO9 (top), PO10(mid), PO11 (bottom): symbol, LES with improved vortex method; line, reference periodic LES
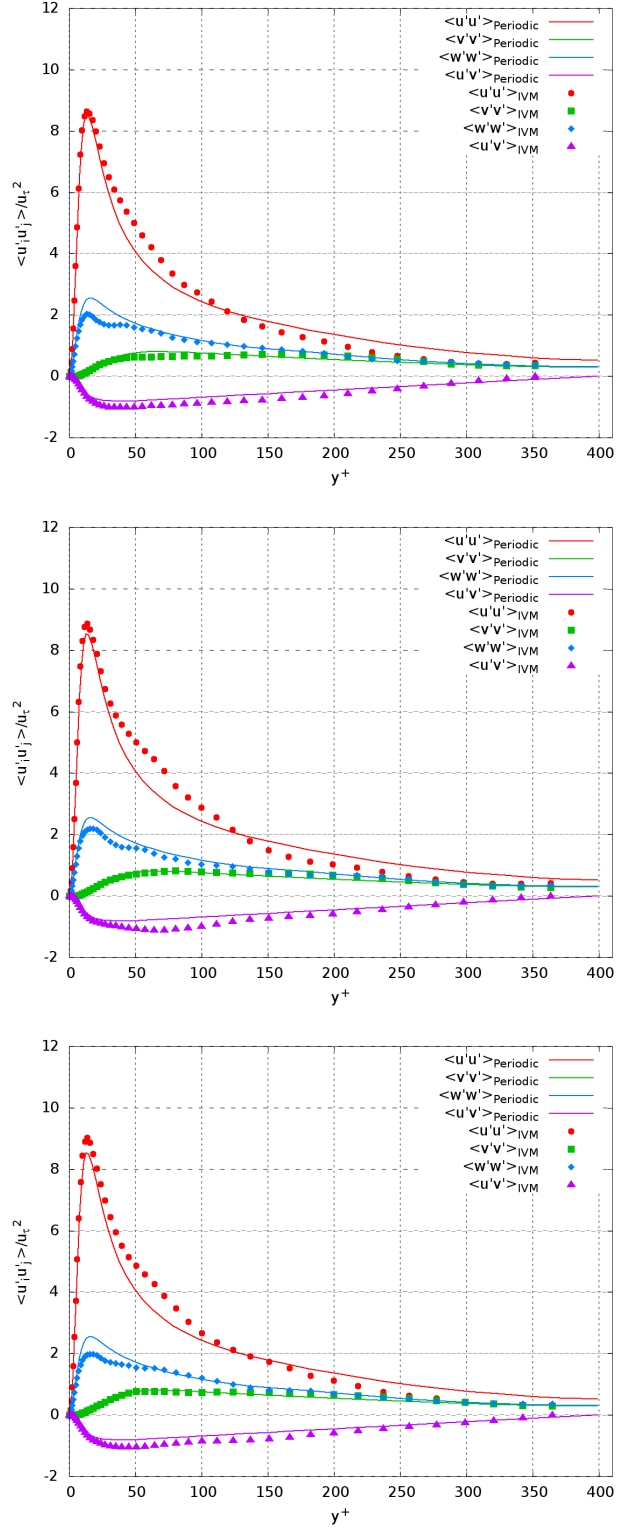
Figure 3.29: Reynolds stresses at outlet $x/h = 2\pi$ of PO9 (top), PO10(mid), PO11 (bottom): symbol, LES with improved vortex method; line, reference periodic LES

coefficient C_4 is fixed at $\frac{1}{16}$.

Stochastic walk

The test cases concerning the vortex stochastic walk are PO12, PO13 and PO14 in Tab. 3.2. The model coefficient C_5 increases from PO12 to PO14, meaning that the ratio between σ^2 (random part) and T_L (integral timescale) increases, as shown in Eq. (2.30). The 2D velocity fluctuations generated at inlet are shown in Fig. 3.30. For PO12, model coefficient C_5 is the smallest, the profile of $\langle v'v' \rangle$ almost superposes with the profile of $\langle w'w' \rangle$, which are still underestimated compared with the reference periodic LES $\langle v'v' \rangle$. As increasing C_5, the peak values of $\langle w'w' \rangle$ and $\langle v'v' \rangle$ increase, the two profiles separate with each other. This result is more pronounced in PO14.

Fig. 3.31 plots the evolution of friction coefficient for all the three cases. A general behaviour is observed, friction coefficient drops and increase to the fully developed value at about $x/h = 6$. For PO12, the model coefficient C_5 is the smallest, the drop is the deepest, with a minimum value of about 3.1×10^{-3} at $x/h = 2.3$. Until the flow get further developed, it cannot recover to its initial value at inlet ($\simeq 4.55 \times 10^{-3}$), with a value of 4.2×10^{-3} at $x/h = 6$. While for PO13, the drop is faster and smaller, with a minimum value of 3.4×10^{-3} at $x/h = 1.8$. Until the flow become turbulent, at $x/h = 6$, c_f reaches to its initial value at inlet (4.55×10^{-3}). While this value is overestimated by PO14, with $c_f \simeq 4.9 \times 10^{-3}$ at $x/h = 6$.

The mean velocity profiles at outlet are shown in Fig. 3.32. Better predictions are obtained by PO13 and PO14. For PO12, the smallest model coefficient C_5 is imposed, larger error is observed in the center of the channel. While results of PO13 and PO14 agree well with the reference periodic LES one. The comparison of Reynolds stresses are drawn in Fig. 3.33. In terms of $\langle v'v' \rangle$, $\langle w'w' \rangle$ and $\langle u'v' \rangle$, PO13 and PO14 give better predictions. While $\langle u'u' \rangle$ of PO13 and PO14 is overestimated by about 20%, compared with the reference periodic LES result.

To conclude, the test cases with larger model coefficient C_5 can achieve better results at outlet. Thus, the model coefficient C_5 of stochastic walk is suggested to be chosen large ones. Here, this fifth vortex parameter, which is independent
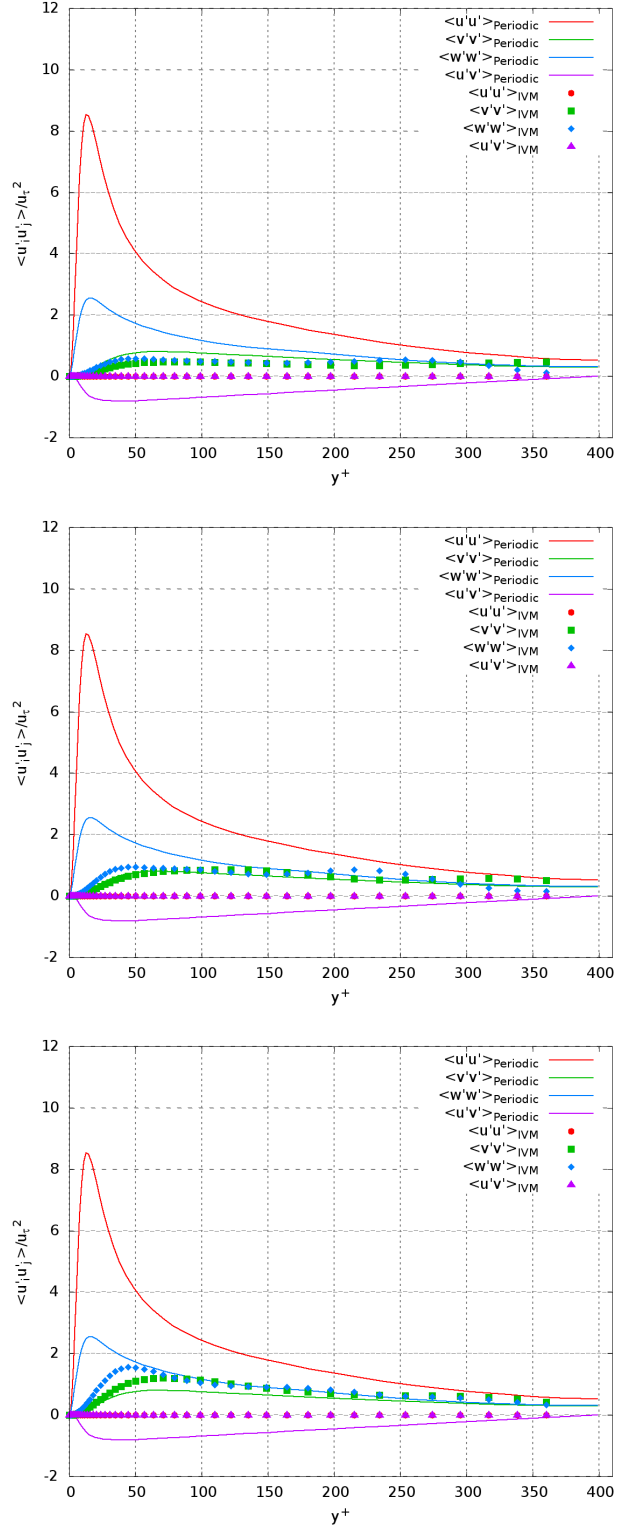
Figure 3.30: Reynolds stresses at inlet $x/h = 0$ of PO12 (top), PO13(mid), PO14 (bottom): symbol, LES with improved vortex method; line, reference periodic LES
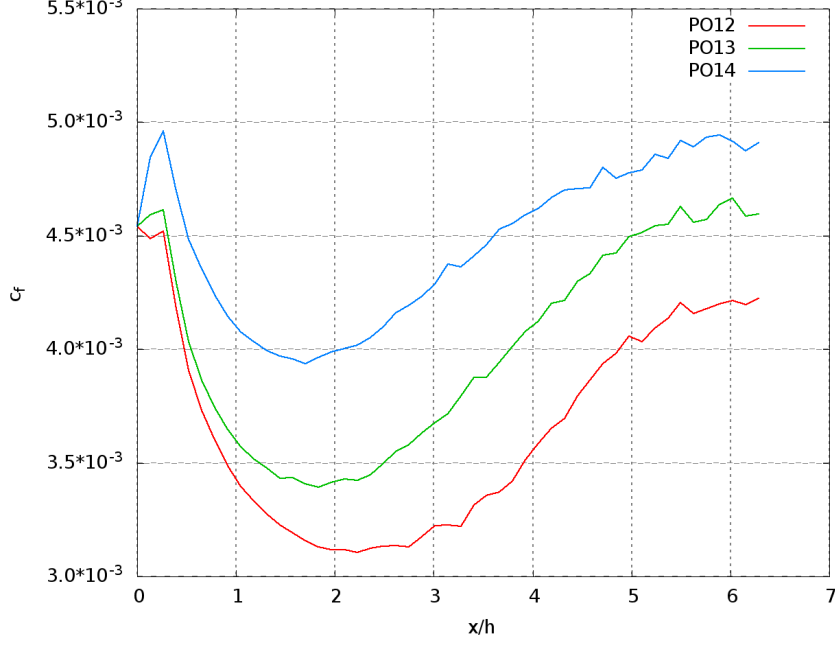
Figure 3.31: Evolution of friction coefficient c_f of PO12, PO13 and PO14

of the fourth one, C_5 is set to 5. This value could be modifiable in a large range.

However, it should be noticed that the value of c_f is sensitive to C_5, as shown in Fig. 3.31. Compared to the ERW method, no improvement of the results is observed. Thus we recommend to use ERW method for practical computation.

3.1.4 Analysis of velocity-derivative skewness

To measure development of the turbulence in the channel, the velocity derivative skewness along the streamwise direction S_u is used as an indicator. S_u is defined as

$$S_u = S(\frac{\partial u}{\partial x}) = \frac{\langle (\partial u/\partial x)^3 \rangle}{[\langle (\partial u/\partial x)^2 \rangle]^{3/2}} \tag{3.5}$$

In fully developed turbulence, S_u should be a negative constant, which indicates that 1) Globally, the energy transfer is from large scale motions to small scale motions; 2) energy transfer is balanced with the dissipation.

Fig. 3.34 plots the evolution of S_u for selected cases PO1, PO7, PO10 and PO13 and evolution of friction coefficient is shown in Fig. 3.35. The velocity-
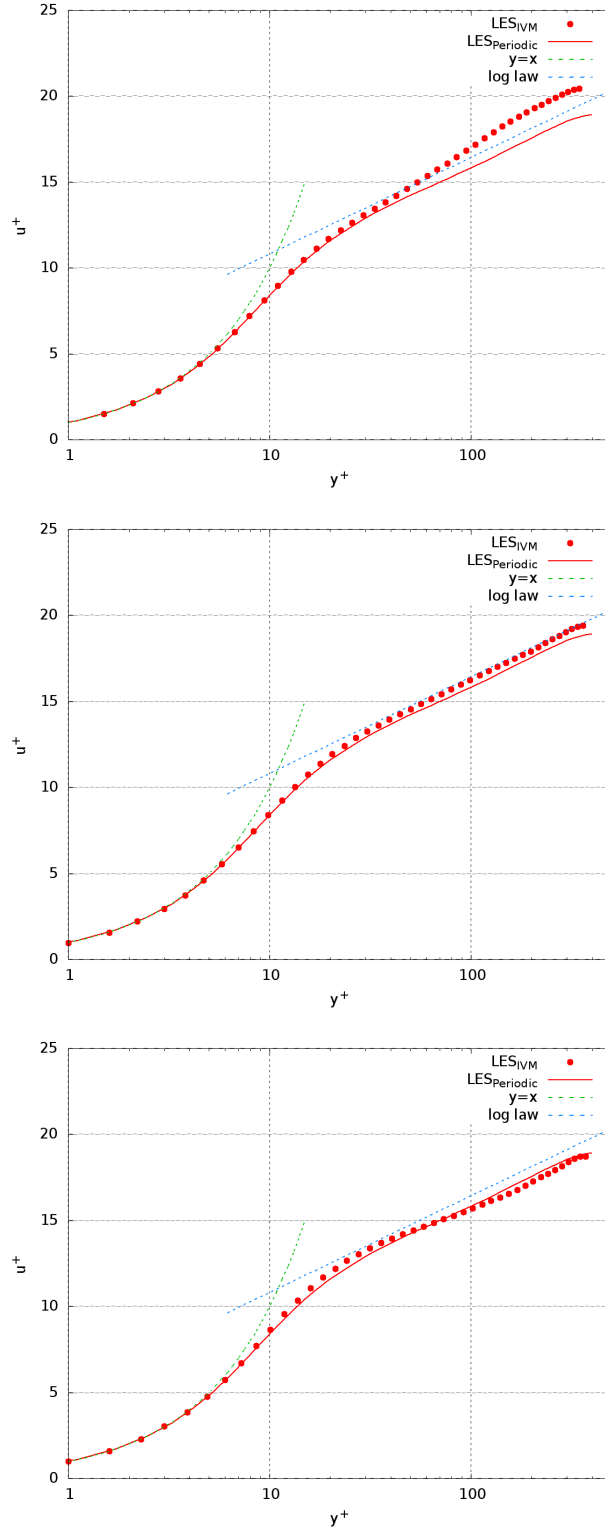
Figure 3.32: Mean velocity profiles at outlet $x/h = 2\pi$ of PO12 (top), PO13(mid), PO14 (bottom): symbol, LES with improved vortex method; line, reference periodic LES
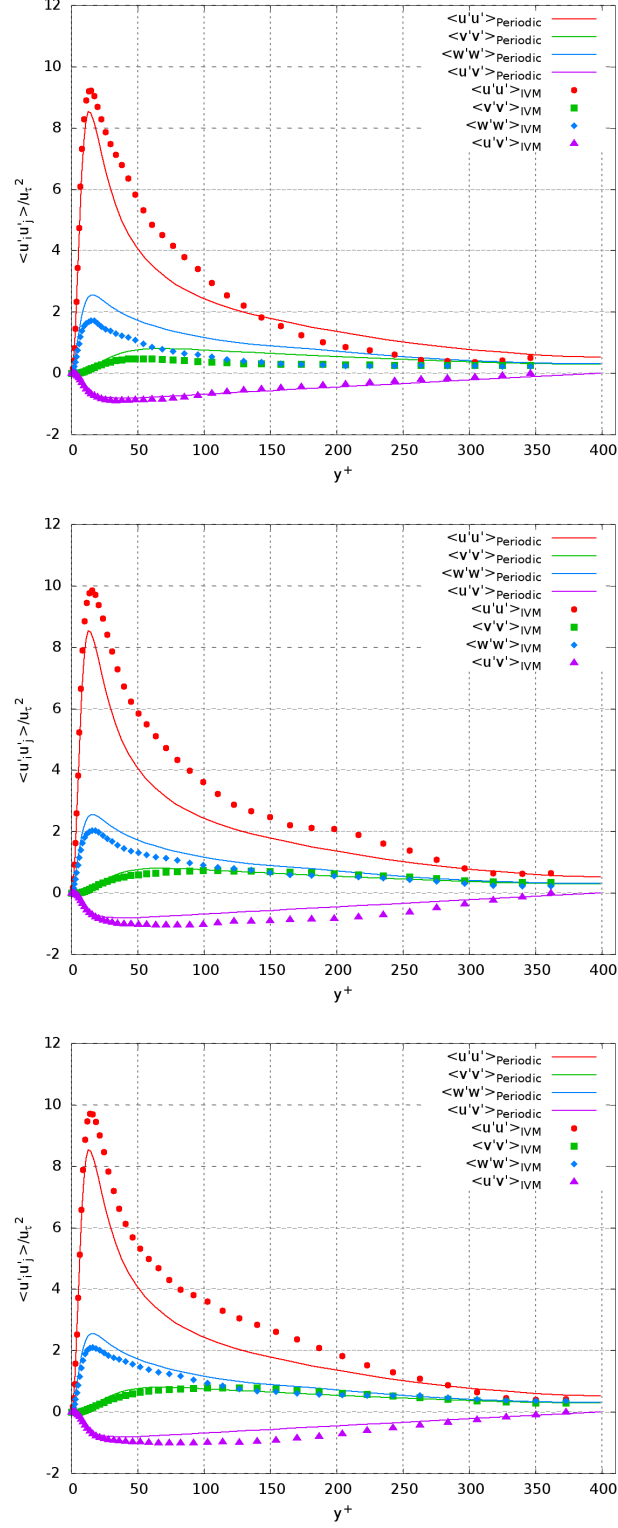
Figure 3.33: Reynolds stresses at outlet $x/h = 2\pi$ of PO12 (top), PO13(mid), PO14 (bottom): symbol, LES with improved vortex method; line, reference periodic LES
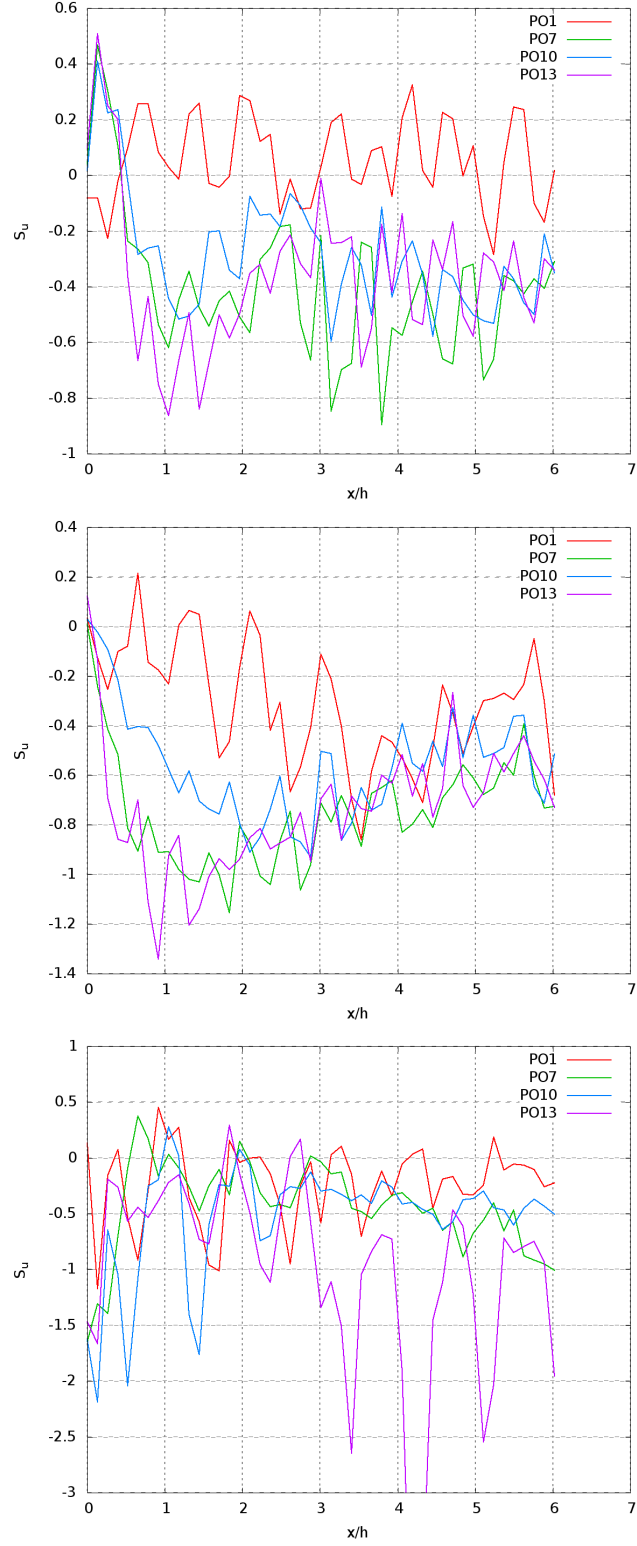
Figure 3.34: Evolution of velocity-derivative skewness: $y^+ = 10$(top), $y^+ = 100$(mid), $y^+ = 200$(bottom)

derivative skewness is measured at different y^+, from 10 to 200. A general behavior is observed for all three cases PO7, PO10 and PO13, S_u for low y^+ ($y^+ = 10$ and $y^+ = 100$) starts from 0 at inlet, drops downstream, then increase and stabilize at some value near the outlet. Results are very scattering at the beginning ($x/h = 0$ to $x/h = 5$) and convergence is obtained from about $x/h = 5$.

For PO1, S_u is very scattering and oscillates around 0, suggesting that the turbulence is poorly developed. Also, Its friction coefficient drops continuously, indicating that the flow relaminarizes.

For cases PO7 and PO10, S_u with high y^+ ($y^+ = 200$) starts from about -1.5 at inlet, oscillate downstream till it finally stabilize around some value. While for PO13, S_u with high y^+ ($y^+ = 200$) cannot reach to a convergent value.

For PO7, S_u at $y^+ = 10$ converge to -0.5 at $x/h \simeq 5$, while the convergent value is about -0.6 for $y^+ = 100$ and -0.7 for $y^+ = 200$. For PO10, S_u converge to a value around -0.4 at $x/h = 5$ for all three y^+. And for PO13, S_u at $y^+ = 10$ converge to -0.4 at about $x/h = 5$, which is -0.6 for $y^+ = 100$.

Results of S_u suggest that the turbulence get well developed after experiencing a transition region ($x/h = 0$ to $x/h = 5$), which is usually observed in fractal-generated turbulence [Hearst and Lavoie, 2015][Valente and Vassilicos, 2014]. Measurement of Hearst and Lavoie [2015] shows that after a sufficient decay period ($x/M = 20$ where M is the mesh length), S_u takes a near constant value of about -0.43.

Considering the evolution of friction coefficient, as plotted in Fig. 3.35. Except for PO1, the friction coefficient c_f drops continuously from inlet to outlet, the other three cases PO7, PO10 and PO13, their friction coefficients drop from inlet and gradually return back to a steady value at about $x/h = 6$, indicating that the turbulence transition region is between $x/h = 0$ and $x/h = 6$ and flows get fully developed at about $x/h = 6$. The evolution of friction coefficient c_f is in company with the development of velocity-derivative skewness along the streamwise direction S_u.
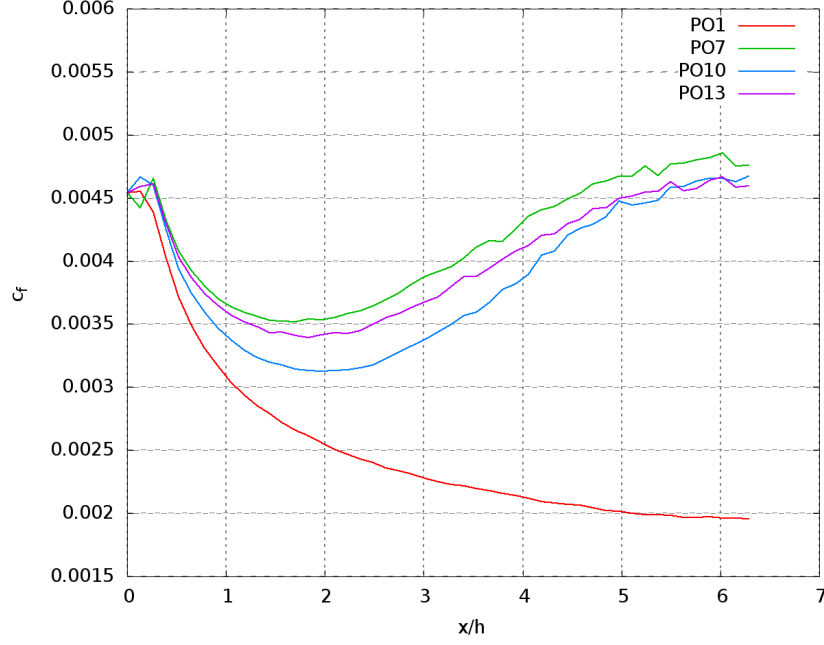
Figure 3.35: Evolution of friction coefficient c_f of PO1, PO7, PO10 and PO13

3.1.5 Adaptation distance

In order to check these assessments, i.e., at $x/h \simeq 6$, a fully developed turbulent flow is established. Computation (PO7+) with longer box $L_x = 3\pi h$ is performed. Flow configurations and vortex parameters of PO7+ are the same as those of PO7, as summarized in Tab. 3.3.

Fig. 3.36 plot the evolution of the friction coefficient c_f (top) and the velocity-derivative skewness S_u (bottom) for both calculations. Either the friction coefficient or the velocity-derivative skewness of PO7 correspond well with those

Test Cases	Domain size $L_x \times L_y \times L_z$	Radius σ C_1	Circulation Γ C_2	Lifetime τ C_3	Displacement C_4	C_5
PO7	$2\pi h \times 2h \times \pi h$	1/4	1.2	10	1/16	-
PO7+	$3\pi h \times 2h \times \pi h$	1/4	1.2	10	1/16	-

Table 3.3: Parameters of PO7+
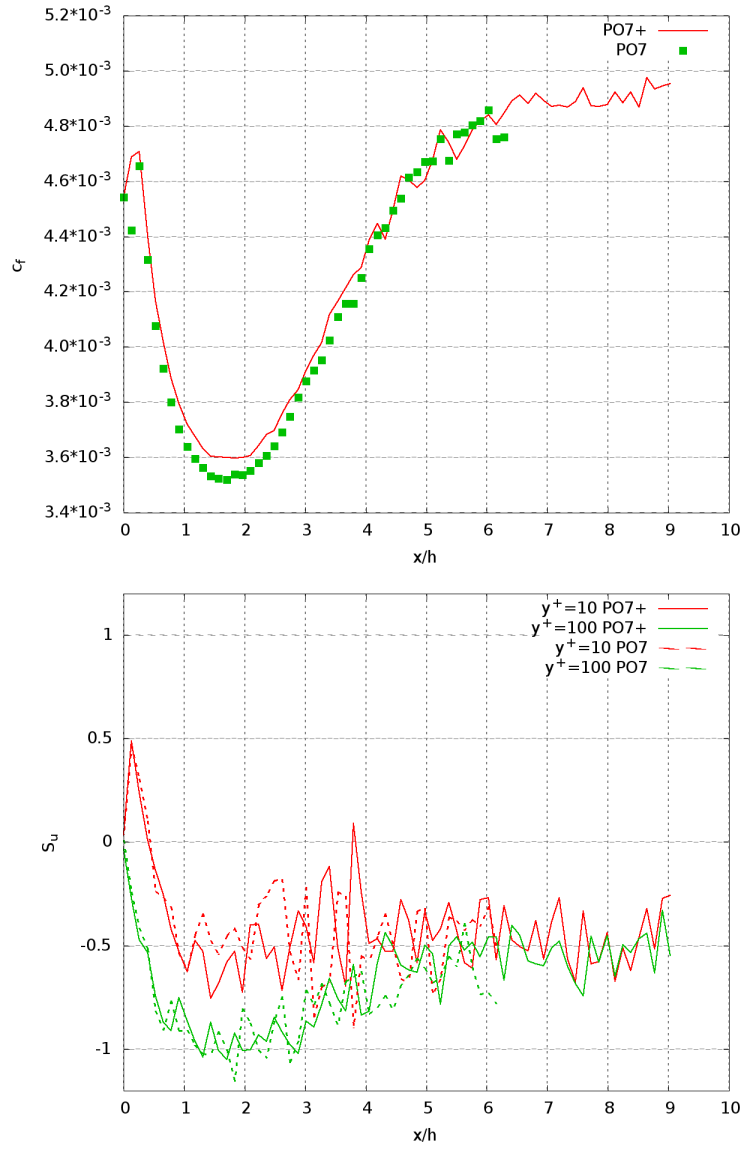
Figure 3.36: Evolution of the friction coefficient (top) and the velocity-derivative skewness S_u (bottom): dashed line, PO7; line, PO7+
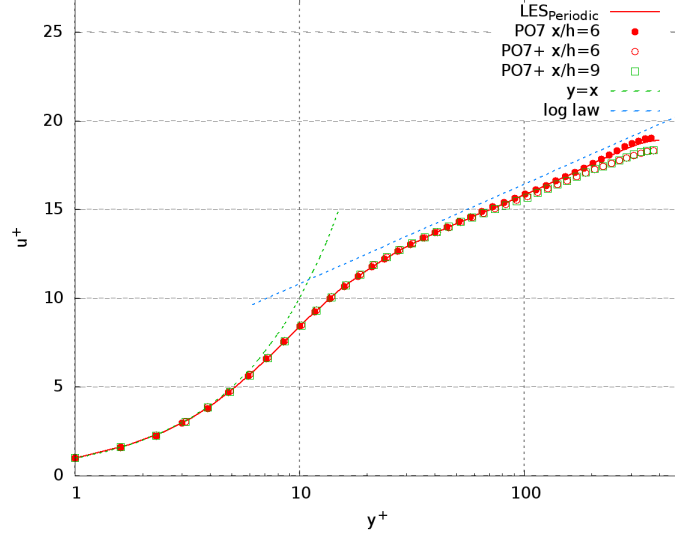
Figure 3.37: Mean velocity profile of PO7 (at $x/h = 6$), PO7+ (at $x/h = 6$ and $x/h = 9$): symbol, LES with improved vortex method; line, reference periodic LES

of PO7+. Friction coefficient c_f of PO7+ reaches to fully developed value at $x/h \simeq 6$, and from $x/h \simeq 6$, c_f stabilize around a value of about 4.9×10^{-3}. It is slightly higher than which of PO7 at $x/h = 6$ ($\sim 4\%$). Similar behavior is displayed with the velocity-derivative skewness S_u. At both $y^+ = 10$ and $y^+ = 100$, S_u shows less scattering from $x/h \simeq 6$, and oscillate around a value of about -0.5. The evolution of friction coefficient is linked to the development of mean velocity and the evolution of skewness correspond to the development of turbulence or the development of fluctuating velocity. Thus, results of the friction coefficient and the velocity-derivative skewness demonstrate that the flow become fully developed from $x/h \simeq 6$, giving an adaptation distance of about $6h$.

Results of the mean velocity and Reynolds stress profiles of PO7 (at $x/h = 6$) and PO7+ (at $x/h = 6$) are shown in Fig. 3.37, in comparison with profiles of PO7+ (at $x/h = 9$) and reference periodic LES results. Mean velocity profile of PO7 at $x/h = 6$ and PO7+ at $x/h = 6$ agrees well with the one of PO7+ at $x/h = 9$. Very small discrepancy is obtained between profiles at $x/h = 6$ and profiles at $x/h = 9$. Similar features are obtained with the Reynolds stress profiles of the two calculations. Compared with data of reference periodic LES,
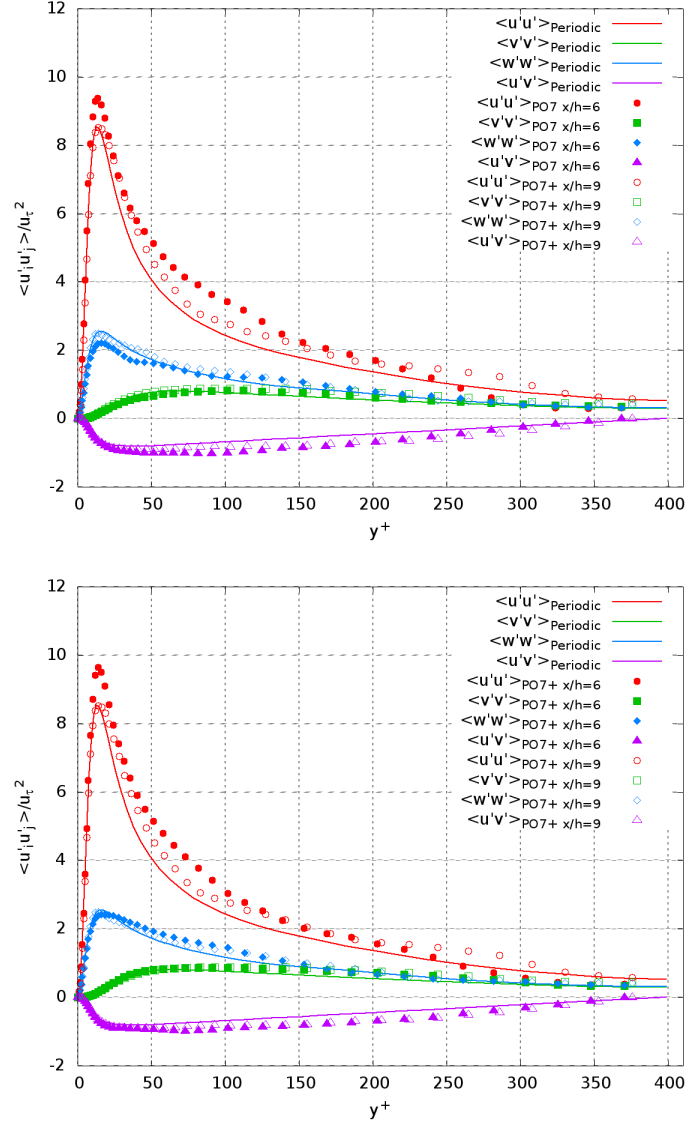
Figure 3.38: Reynolds stresses of PO7 (at $x/h = 6$ top), PO7+(at $x/h = 6$ bottom), in comparison with $PO7+$ (at $x/h = 9$): symbol, LES with improved vortex method; line, reference periodic LES
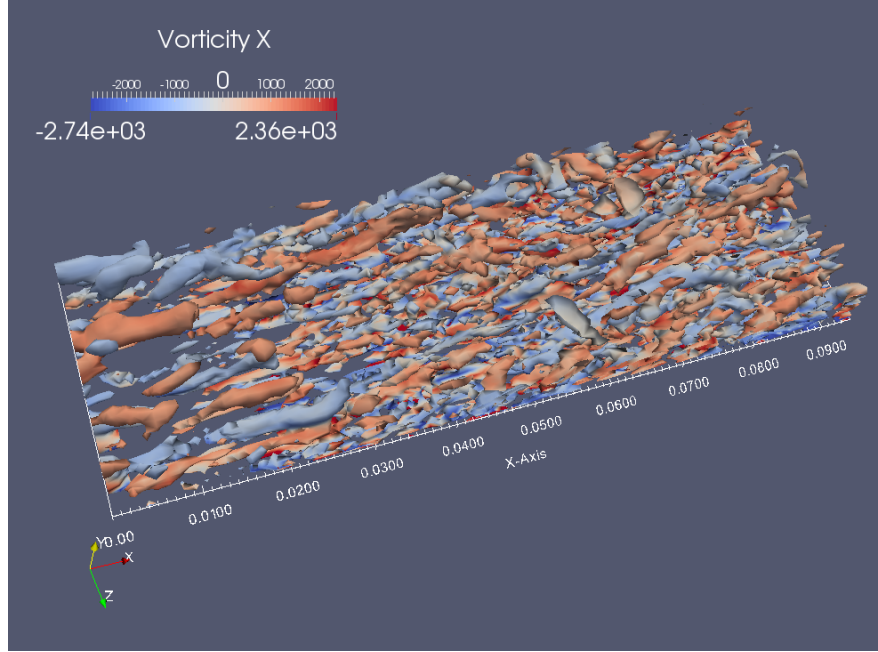
Figure 3.39: Isosurface of Q-criterion (Q=200000) colored by the streamwise vorticity of PO7+

results are quite satisfied. Although some discrepancies are pronounced for the Reynolds stress profiles.

Results of the mean velocity and Reynolds stress profiles of PO7 (at $x/h = 6$), PO7+ (at $x/h = 6$) and PO7+ (at $x/h = 9$) further confirm that fully developed turbulent flow gets established from $x/h \simeq 6$. Following the original method of Sergent [2002], Benhamadouche et al. [2006] shows that RMS profiles have an appropriate behavior from $x/h = 12$. A synthetic-eddy method developed by Jarrin et al. [2009] requires at least $10h$ distance in the streamwise direction to achieve fully developed channel flows. Later, this approach is applied by Poletto et al. [2013] and results of friction coefficient indicate that at least $10h$ is needed for redevelopment.

More characteristics of the instantaneous flow filed can be presented by the Q-criterion, as shown in Fig. 3.39. A general phenomena is observed: as flow passes downstream, structures of turbulence tends to be smaller. From $x/h \simeq 6$, both large and small structures are present, similar to what usually observed in fully developed turbulent channel flow [Jeong et al., 1997].

Test Cases	Radius σ C_1	Circulation Γ C_2	Lifetime τ C_3	Dispalcement ERW C_4	SW C_5
CPVM	1/4	1.2	10	1/16	-
PO7	1/4	1.2	10	1/16	-

Table 3.4: Parameters of CPVM

3.2 Application to channel flow at $Re_\tau = 590$

3.2.1 Numerical configuration

3.2.1.1 Mesh configuration

The calculation is performed in a channel of $2\pi h \times 2h \times \pi h$ using a grid of $73 \times 131 \times 61$ points. Here, $h = 0.01m$ is the half height of the channel. The mesh is uniform in the streamwise direction (x-direction) and in the spanwise direction (z-direction), and follow a tanh form distribution in the wall-normal direction (y-direction). The grid resolutions in wall units are $\Delta x^+ = 52$, $\Delta y^+ = 0.5$, $\Delta z^+ = 31$ in the streamwise, wall-normal and spanwise direction, respectively.

3.2.1.2 Initial and Boundary conditions

The calculation is initialized with a RANS results ($Re_\tau = 590$). The improved vortex method is used at inlet to generate an unsteady boundary condition. The mixed non-reflection pressure outlet condition is employed on the outlet boundary. A periodic boundary condition is applied to the spanswise boundaries. The end-walls on the top and bottom sides of the channel are set as non-slip adiabatic walls.

The vortex method's parameter coefficients for CPVM are shown in Tab. 3.4, which is the same set-up as the calculation PO7. The number of vortices injected at inlet is also 800.
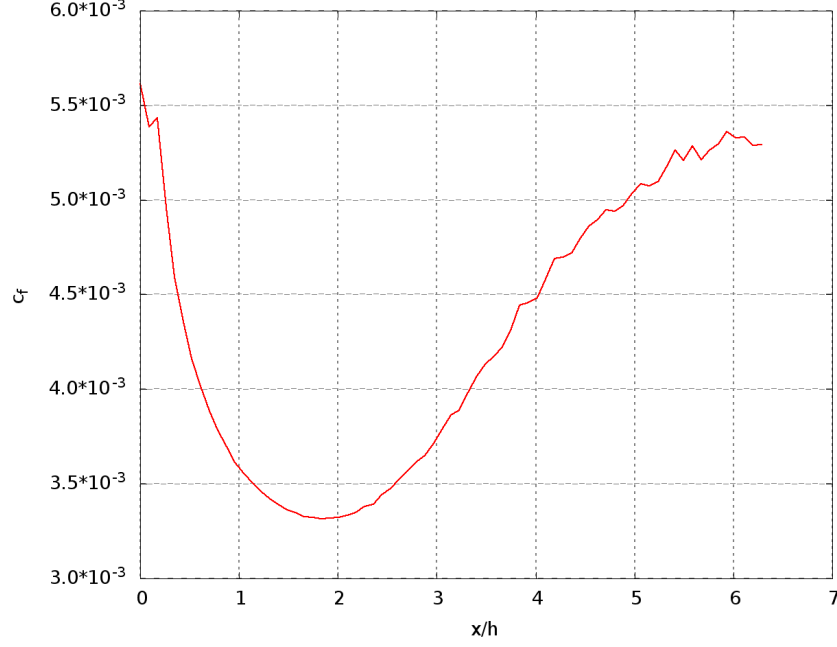
Figure 3.40: Evolution of the friction coefficient c_f

3.2.2 Results

3.2.2.1 Friction coefficient evolution

The evolution of the friction coefficient is shown in Fig. 3.40. Results are similar to PO7. The friction coefficient drops from inlet, and reaches to the minimum value 0.0033 at $x/h = 1.8$. Then it increase, and from $x/h = 6$, c_f oscillates around a value of 0.0053. It is slightly underestimated in comparison with its value at inlet ($c_f = 0.0056$).

3.2.2.2 Velocity-derivative skewness

Statistical results of velocity derivative skewness S_u along the streamwise direction is given in Fig. 3.41. At $y^+ = 18.4$, S_u starts around 0 near the inlet, and drops downstream. It reaches to a minimum value at about $x/h = 1.8$. Going further downstream, it increases and oscillates. From about $x/h = 4.5h$, the oscillations stabilize around $S_u = -0.5$, suggesting that the exchange of energy between large- and small-scale motions is balanced. Considering the evolution of
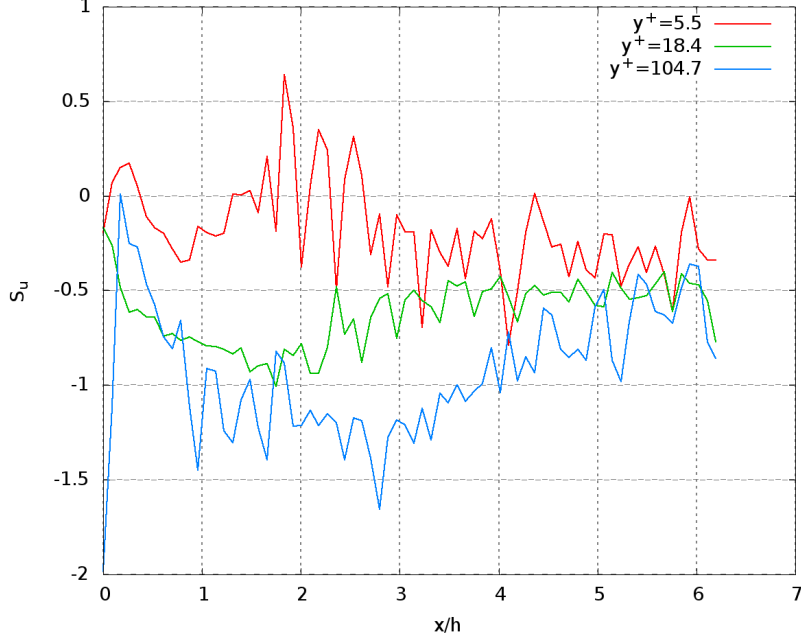
Figure 3.41: Evolutions of the velocity-derivative skewness along the streamwise direction S_u at $y^+ = 5.5$, $y^+ = 18.4$ and $y^+ = 104.3$

the friction coefficient, it can conclude that real turbulence is established from about $x/h = 6h$. Similar observations are found at both the position $y^+ = 5.5$ and $y^+ = 104.3$. The velocity-derivative skewness of the fully developed turbulence at $y^+ = 5.5$ oscillates at about -0.32. This mean value is -0.67 for $y^+ = 104.3$.

Further characteristics of the instantaneous flow filed is presented by the Q-criterion ([Hunt et al., 1988]), as shown in Fig. 3.42. As flow passes downstream, structures of turbulence tends to be smaller. From $x/h \simeq 5$, both large and small structures are present, similar to what usually observed in fully developed turbulent channel flow [Jeong et al., 1997].

3.2.2.3 Mean velocity and Reynolds stresses

The generated 2D fluctuating velocity field at inlet is illustrated in Fig. 3.43. The vortex structure can be observed clearly, with big structure in the center of the channel while fine structure near the wall boundary.

The Reynolds stresses at inlet $x/h = 0$ is shown in Fig. 3.44. Curve of $\langle w'w' \rangle$
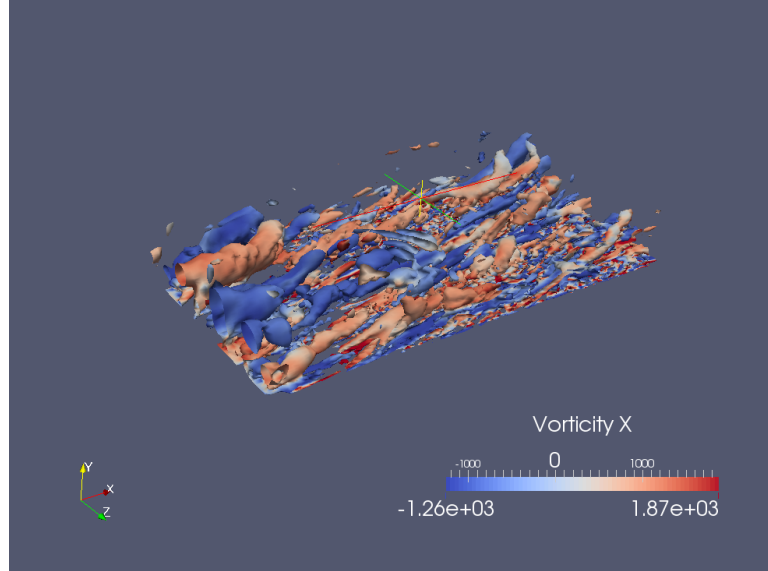
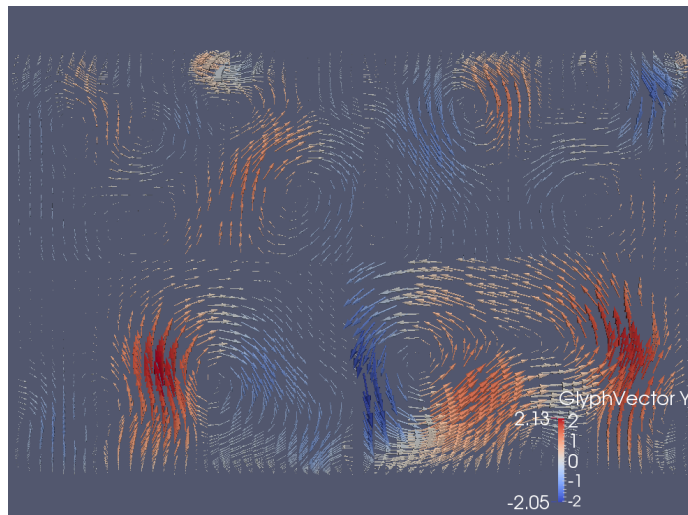Figure 3.42: Isosurface of Q-criterion (Q=200000) colored by the streamwise vorticity

Figure 3.43: 2D velocity field at inlet $x/h = 0$, case of channel flow with $Re_\tau = 590$
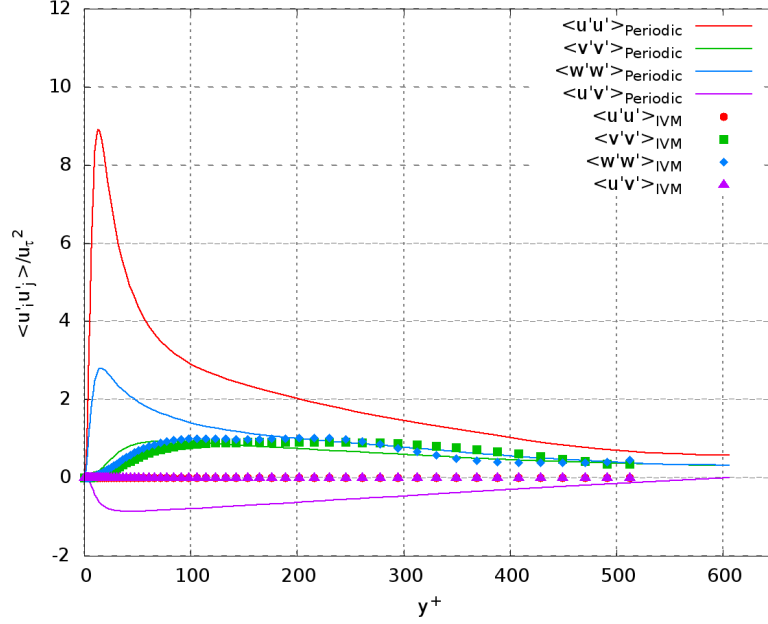
100

Figure 3.44: Reynolds stress at inlet $x/h = 0$ of CPVM: symbol, LES with improved vortex method; line, reference periodic LES

superpose on the one of $\langle v'v' \rangle$, suggesting that the generated fluctuations are isotropic (2D) at inlet plane.

The profiles of the mean velocity and Reynolds stresses at $x/h = 6$ are shown in Fig. 3.45 and Fig. 3.46. Results of periodic LES ($Re_\tau = 590$) are used as reference data.

The mean velocity profile is very well predicted by the CPVM. Results of CPVM agree well with the reference periodic LES. Both near-wall region and log-law region are satisfactorily captured. Concerning the Reynolds stresses, the results are acceptable. The inner peak of $\langle u'u' \rangle$ is about 9.3, locating at $y^+ = 13.8$. While the reference periodic LES inner peak of $\langle u'u' \rangle$ is about 8.8 at $y^+ = 13.3$. Profiles of $\langle w'w' \rangle$, $\langle v'v' \rangle$ and $\langle u'v' \rangle$ agree well with the reference periodic LES, suggesting that the channel flow get fully developed at about $x/h = 6$.
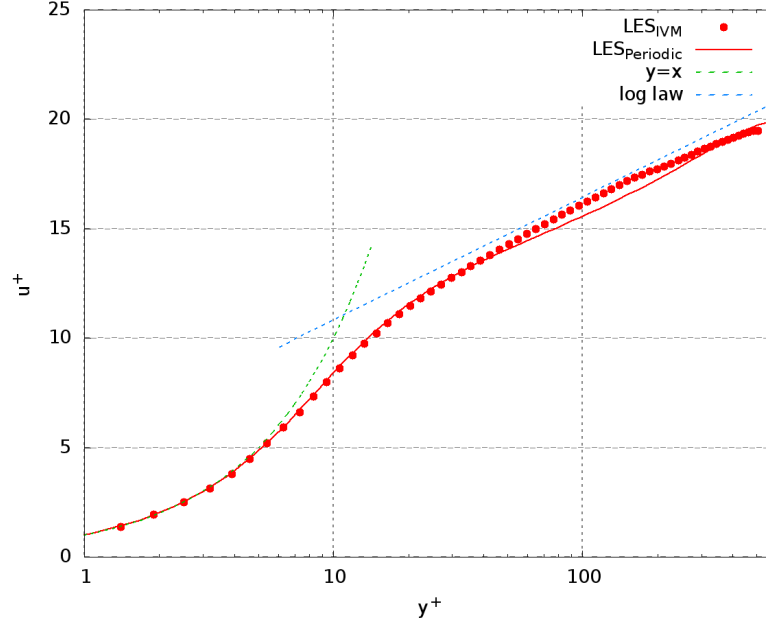
Figure 3.45: Mean velocity profiles at $x/h = 6$ of CPVM: symbol, LES with improved vortex method; line, reference periodic LES
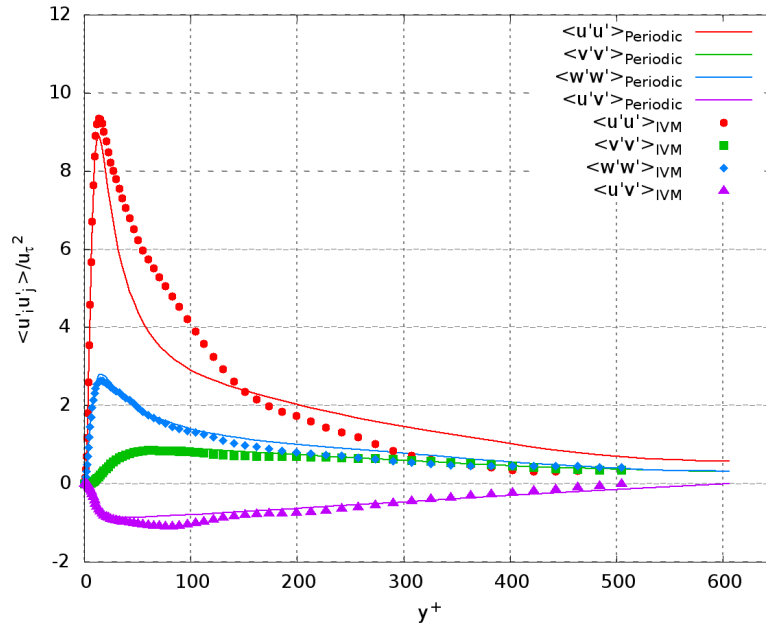

Figure 3.46: Reynolds stresses at $x/h = 6$ of CPVM: symbol, LES with improved vortex method; line, reference periodic LES

Chapter 4

Flat-plate boundary layer

4.1 Introduction

A flat-plate boundary layer is used to validate the improved vortex method. Generally, turbulent boundary layers are often used as inlet to feed the main calculation downstream. The main issue is how to force the turbulence transition. In practice, in order to force the transition from laminar flow, a trip or step is usually used in DNS or LES, thus an unsteady turbulent boundary layer can be obtained. In this chapter, first, a LES of flat-plate turbulent boundary layer [Boudet et al., 2015] inducing the transition process is reproduced. Then, the results are used as reference data for the application of improved vortex method. An unsteady fluctuating velocity field is generated by the improved vortex method on the flat-plate and superimposes on an extracted mean velocity profile. Then the flow field develops as real turbulence downstream.

4.2 Reference flat-plate boundary layer LES

The process of tripping the transition in LES is not just a numerical attempt, it is based on a physical mechanism. In the experimental aerodynamic context, transition to turbulence is often triggered by using a roughness element on the wall. With enough distance downstream, the boundary layer can finally become turbulent. Following the work of Boudet et al. [2015], instead of using a roughness

Test Cases	Domain size $L_x \times L_y \times L_z$	Trip	SGS model
CLPP	$0.31m \times 11.7mm \times 5.86mm$	source term	WALE

Table 4.1: Main set-up of reference LES - CLPP

element to force the transition as usual way, a volume drag force term is used here to yield the transition to turbulence. A simulation based on this approach is carried out in this section.

4.2.1 Numerical set-up

Numerical implementation of trip and computation set-up comes from [Boudet et al., 2015]. LES is carried out with the $Turb'Flow$ solver. The SGS model for LES used in this work is the WALE model.

Main set-up of the reference LES tripping case CLPP is summarized in Tab. 4.1. The computational domain is $L_x = 0.3108m$ long in the streamwise direction, $L_y = 11.7mm$ high at the outlet and $L_z = 5.88mm$ wide in the spanwise direction. The height L_y is about $2\delta(x = L_x)$. Here, δ is the boundary-layer thickness defined as the value of y at which $\langle U(x,y) \rangle$ equals 99% of the free-stream velocity $U_\infty(x)$ and the value of δ is estimated from the $1/7^{th}$ power-law velocity-profile model [Schlichting and Gersten, 2003] and $\delta(x = L_x) = 5.88mm$ [Boudet et al., 2015]. A $-0.5°$ angle is imposed on the upper boundary to force an outlet boundary condition. The mesh is composed by $841 \times 39 \times 43$ points in the streamwise, wall-normal and spanwise directions, respectively. This yields a wall resolution of about $\Delta x^+ < 80$, $\Delta y^+ < 2$, $\Delta z^+ < 30$. The computational domain and mesh configuration are shown in Fig. 4.1. The trip is achieved by adding a source term within a subdomain on the wall in the present computation at $x = 0.0659m$ which will be explained later.

4.2.1.1 Flow configuration

An airflow with a free-stream velocity $U_\infty = 70m/s$ is addressed over the flat-plate in atmospheric conditions ($\rho_\infty = 1.177kg/m^3$, $T_\infty = 300K$, $\mu_\infty = 1.81 \times$
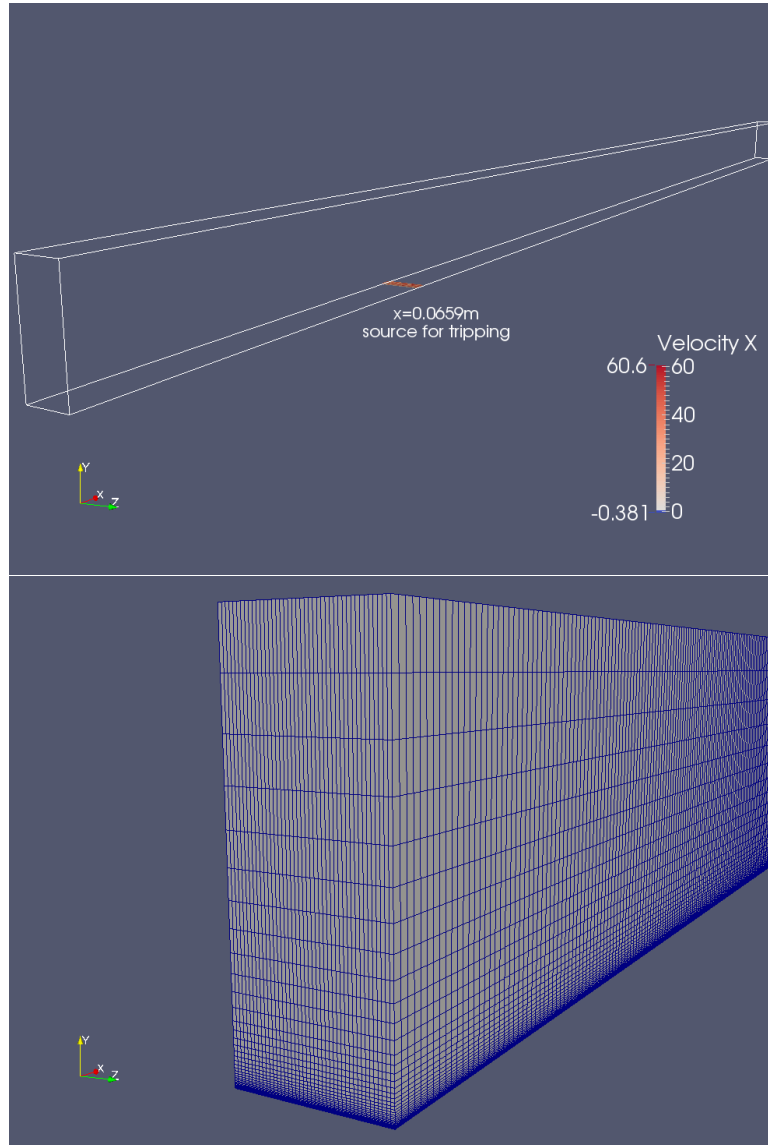
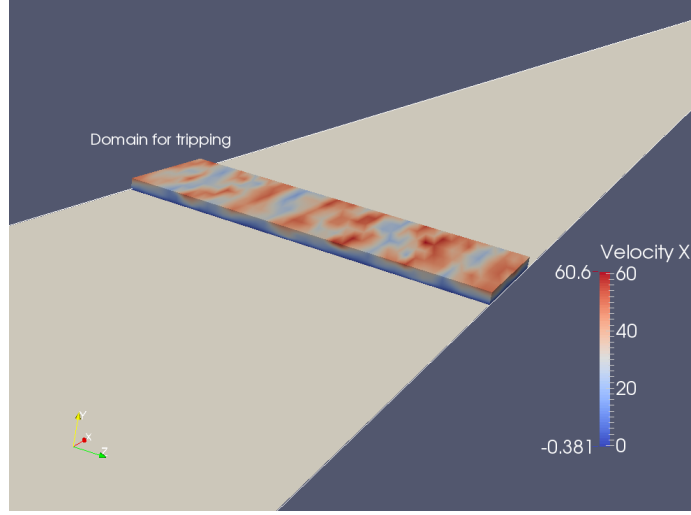Figure 4.1: Computation domain and mesh configuration of reference LES - CLPP

Figure 4.2: Domain for tripping of reference LES - CLPP

$10^{-5} kg/(m \cdot s)$). The Reynolds number at the outlet is about $Re_x = 1.3 \times 10^6$.

Fig. 4.2 shows the domain for tripping. The trip is set at $x = 0.0659m$ [Boudet et al., 2015] on the wall. The height of the trip, according to the work reviewed in [Dryden, 2012], should be $0.78\delta^*_{trip}$, where δ^*_{trip} is the laminar boundary layer displacement thickness without roughness at the position of the roughness element. Here, the roughness element is represented by a source term. Total size of the trip domain is $l_x = 1.85mm$ long, $l_y = 0.16mm$ high, and $l_z = 5.86mm$ wide above the flat-plate. The corresponding source term induced in this domain is

$$f_{trip} = \frac{1}{2}\rho l_y l_z C_D u_x^2 \tag{4.1}$$

Where C_D is a drag coefficient of the order 1.

This approach to implement the trip can have a few advantages: it is more adjustable and easy to be set up. The smooth-wall grid need not to be modified.

4.2.2 Results

The characteristic length and velocity chosen for normalization are the boundary-layer thickness at outlet $\delta(x = L_x)$, which is estimated through the work of [Schlichting and Gersten, 2003] and the friction velocity u_τ.
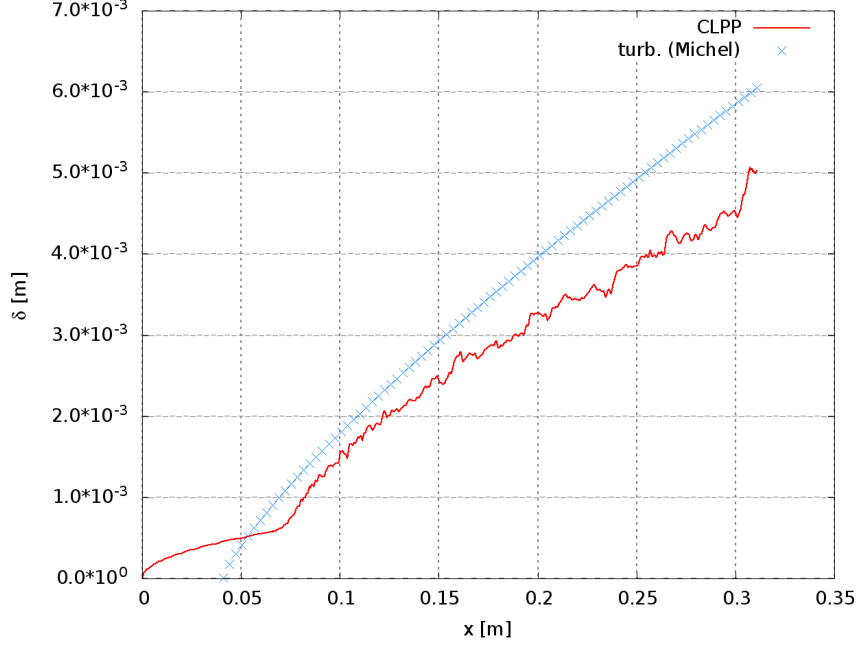
Figure 4.3: Evolution of boundary layer thickness δ of reference LES - CLPP

4.2.2.1 Boundary layer evolution

The evolution of the boundary layer thickness δ, displacement thickness δ^* and momentum thickness θ are illustrated in Fig. 4.3, Fig. 4.4 and Fig. 4.5, respectively. Displacement thickness and momentum thickness are defined as:

$$\delta^*(x) \equiv \int_0^\infty (1 - \frac{\langle U \rangle}{U_\infty})dy \tag{4.2}$$

$$\theta(x) \equiv \int_0^\infty \frac{\langle U \rangle}{U_\infty}(1 - \frac{\langle U \rangle}{U_\infty})dy \tag{4.3}$$

Concerning the momentum thickness θ, LES results agree with the analytic solution of Blasius in the laminar stage. But the LES underestimates the momentum thickness by about 10% in the turbulent region, in comparison with the law of Michel (which uses the power form derived from the hypothesis of a $1/7^{th}$ power law velocity profile [Schlichting and Gersten, 2003]). Similar behaviors are found with the results of boundary layer thickness δ and displacement thickness δ^*.
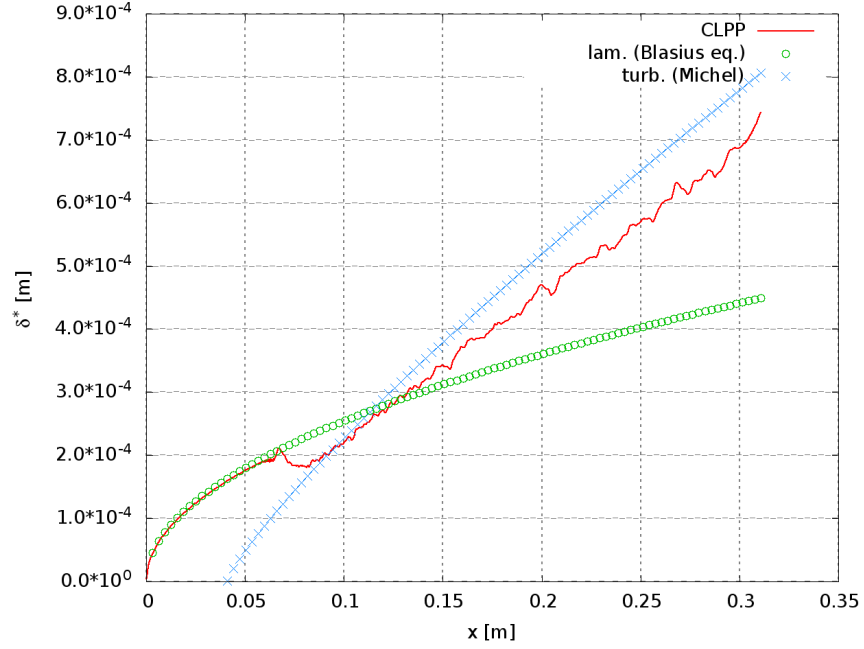
Figure 4.4: Evolution of displacement thickness δ^* of reference LES - CLPP
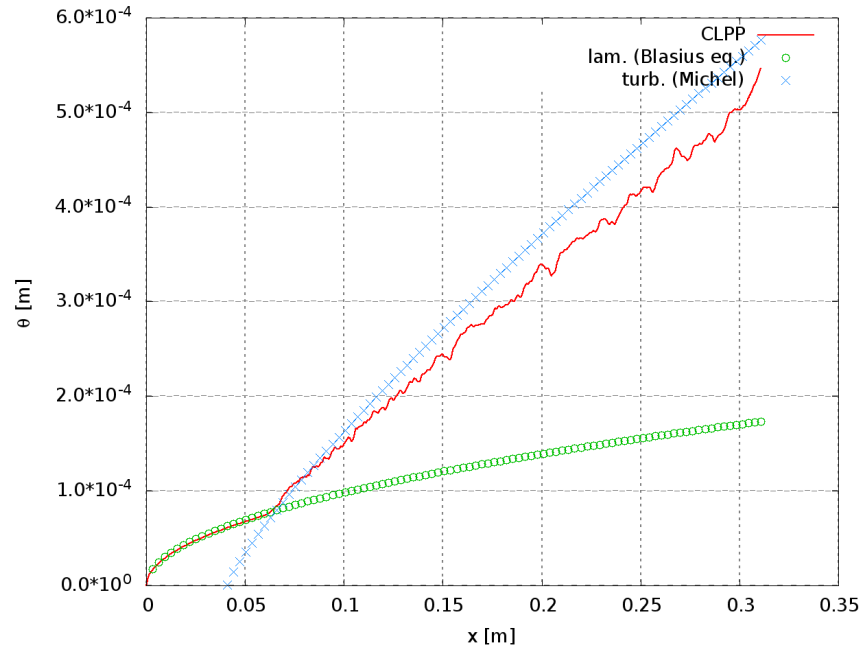
Figure 4.5: Evolution of momentum thickness θ of reference LES - CLPP
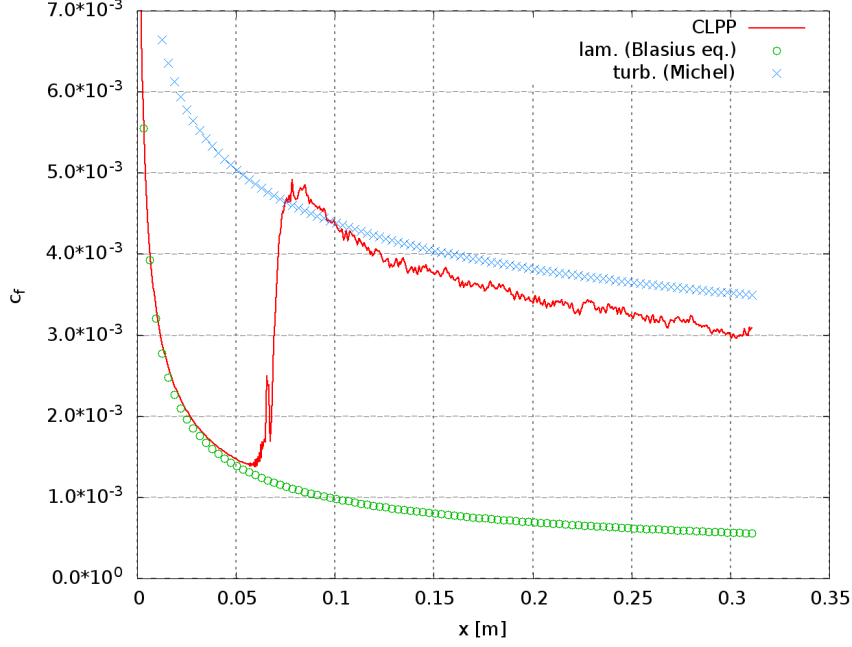
Figure 4.6: Evolution of friction coefficient c_f of reference LES - CLPP

Fig. 4.6 plots the evolution of the friction coefficient c_f defined as

$$c_f = 2(u_\tau/U_\infty)^2 \tag{4.4}$$

Concerning the friction coefficient, the LES achieves good agreement with the law of Blasius in the laminar region and gives an underestimate of about 10% in the turbulent region.

4.2.2.2 Mean velocity profile

The mean velocity profile in the turbulent region at $x = 0.232m$ ($Re_\theta = 1968$ according to law of Michel) is shown in Fig. 4.7. In comparison with the DNS data, the u^+ is well predicted in the wall region, while it is more pronounced in the free stream. The overestimation is about 10% which may be due to the underestimation of the friction velocity.
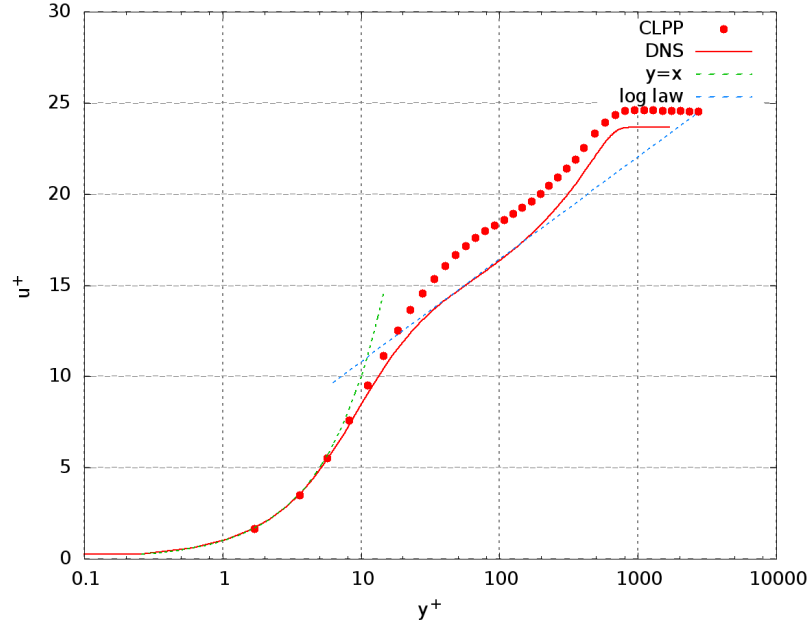
Figure 4.7: Mean velocity profiles at $x = 0.232m$ ($Re_\theta = 1968$): symbol, reference LES - CLPP; line, DNS data
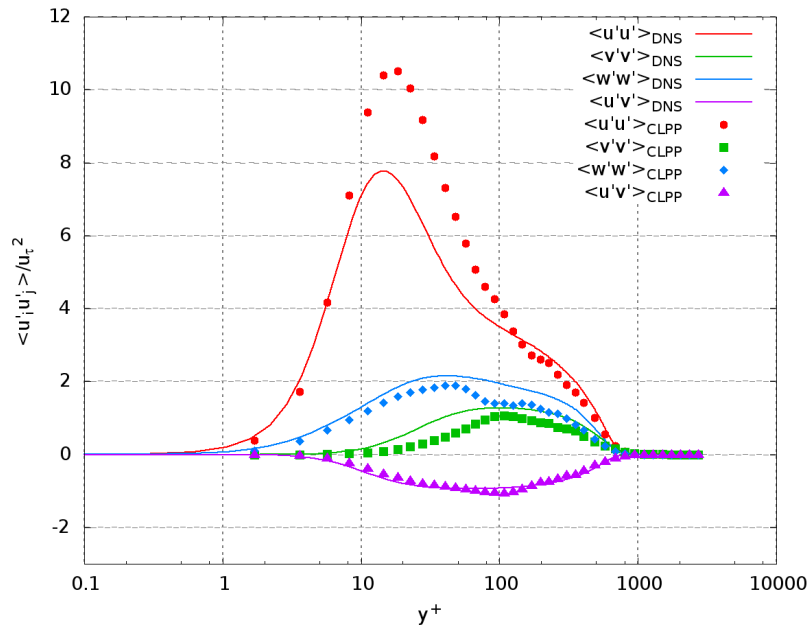

Figure 4.8: Reynolds Stresses at $x = 0.232m$ ($Re_\theta = 1968$): symbol, reference LES - CLPP; line, DNS data

4.2.2.3 Reynolds stresses

The Reynolds stress profiles at $Re_\theta = 1968$ are shown in Fig. 4.8. The DNS inner peak of $\langle u'u' \rangle$ is located at $y^+ = 20$, with a peak value of about 7.6. In comparison, LES shows a higher peak value of about 11.2, with a location at $y^+ = 30$. The profiles of $\langle w'w' \rangle$ and $\langle v'v' \rangle$ are acceptable, and $\langle u'v' \rangle$ agrees well with the DNS data.

4.2.2.4 Velocity-derivative skewness

The velocity-derivative skewness is an indicator of fully developed turbulence. The evolution of velocity-derivative sknewness along the streamwise direction is plotted in Fig. 4.9. S_u is calculated at 3 different positions away from the flat plate: $y^+ = 3.4$, $y^+ = 26.7$ and $y^+ = 140.5$. A common feature is observed for all the three positions. In the laminar flow region ($0 \leq x \leq 0.066m$). S_u oscillates around zero. Then the turbulent transition is forced by the trip around $x = 0.066m$. In this zone ($0.066m \leq x \leq 0.07m$), the oscillation of S_u is more pronounced. The transition to fully developed turbulence is accomplished at about $x = 0.11m$. From this position ($x \geq 0.11m$), S_u converges to some value. For $y^+ = 3.4$, convergent value of S_u is about -0.5. -0.6 is for $y^+ = 26.7$ and -0.4 correspond to $y^+ = 140.5$. The boundary layer get fully developed at about $x = 0.11m$.

4.3 Improved Vortex method on boundary layer

In this section, the application of the improved vortex method on the boundary layer will be presented. The results of the previous LES are used as reference data. A mean velocity profile is extracted from the reference LES (CLPP) at a position located in the fully turbulent region $x = 0.1243m$ ($Re_\theta = 988$ according to law of Michel). The improved vortex method is used to generate a 2D fluctuating velocity field with the statistically averaged turbulent kinetic energy and dissipation profiles (at $x = 0.1243m$) provided by the previous tripping LES simulation. This fluctuating velocity field is then imposed on the extracted mean velocity profile. Turbulence redevelops as the flow passes downstream. It
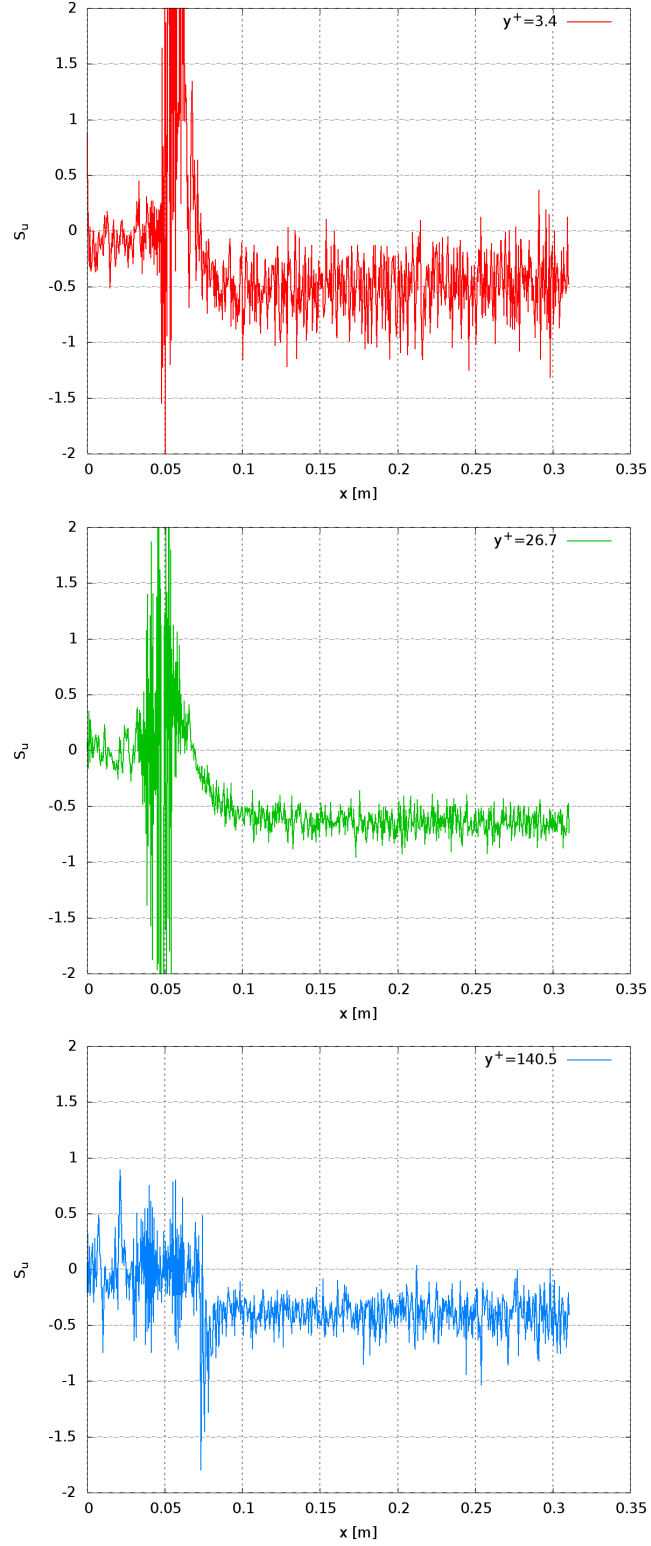
Figure 4.9: Evolution of velocity-derivative skewness along the streamwise direction S_u of reference LES - CLPP at three wall-normal positions

is expected to recover real turbulence as soon as possible.

Since all injected vortices move on the inlet plane, and may inverse every life-time, thus the generated velocity fluctuations are unsteady. The unsteady fluctuating velocity field excites the evolution of turbulence downstream. To examine the development of turbulence and to investigate the effect of the improved vortex method, statistics are extracted at different streamwise positions. The evolution of turbulence are measured by the friction coefficient, boundary layer thickness and further by the velocity-derivative skewness along the streamwise direction.

There are 2 main points which need to be specified when applying the improved vortex method on the boundary layer. First, mean velocity, mean turbulent kinetic energy and mean dissipation rate profiles need to be extracted to initialize the vortex method's parameters. Second, the coefficients in Tab. 3.2 need to be optimized.

4.3.1 Numerical methods

LES is carried out with the Turb'Flow solver. The SGS model for LES used in this work is the WALE model. Numerical set-up is the same as the LES reference case 4.2.

4.3.1.1 Numerical configuration

Extracted mean profiles

Mean Profiles need to be extracted are the mean velocity, turbulent kinetic energy and dissipation rate. The position to extract those quantities is located at $x = 0.1243m$ ($Re_\theta = 988$), as shown in Fig. 4.10. According to the result of reference LES, until $x = 0.11$, the flow become fully developed. The extracting position is just located in the developed turbulent region. Fig. 4.11, Fig. 4.12 and Fig. 4.13 plot the extracted profiles ($Re_\theta = 988$), results agree well with the DNS data ($Re_\theta = 1968$).
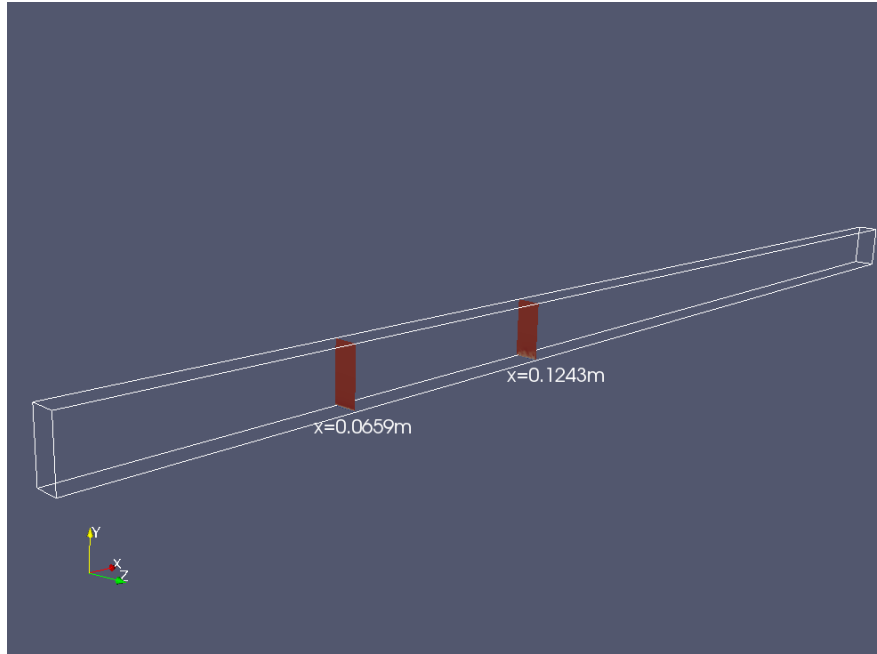
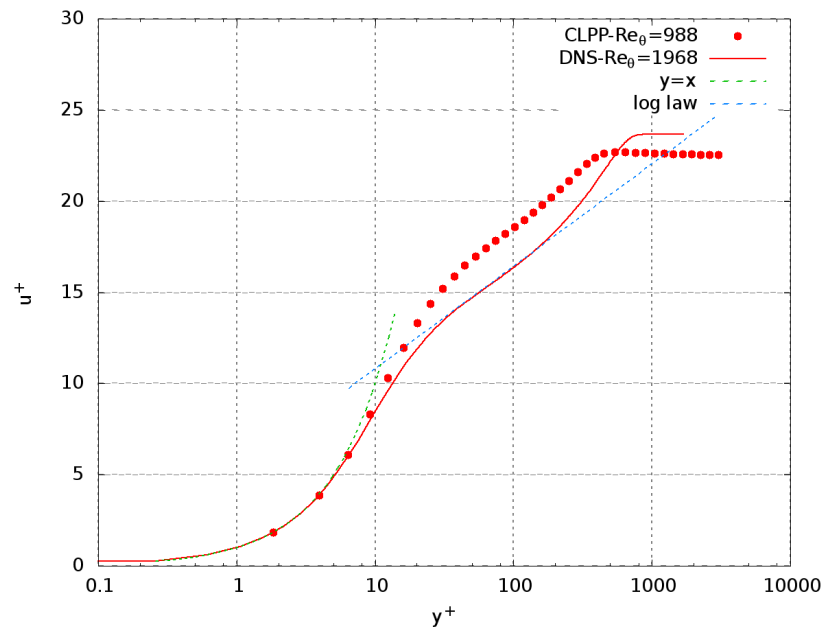Figure 4.10: Position to extract mean profiles: $x = 0.1243m$ ($Re_\theta = 988$)

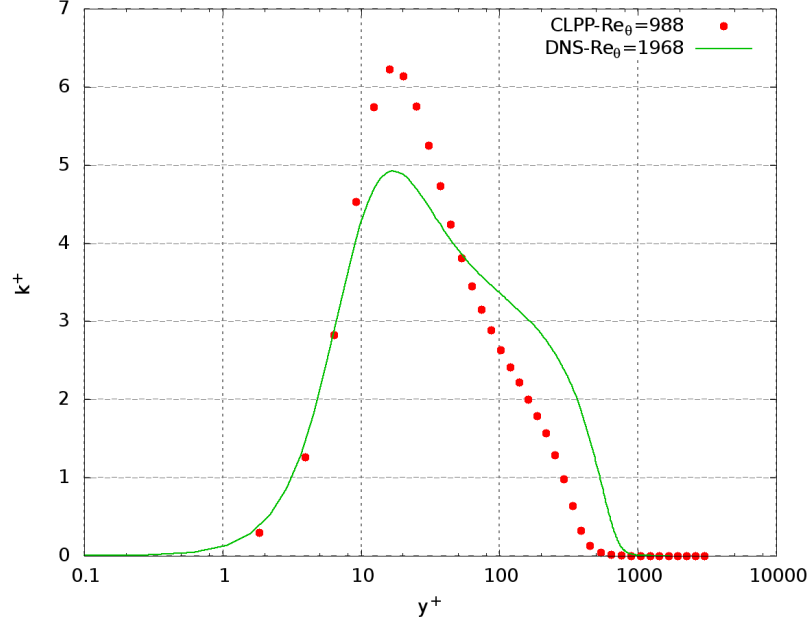Figure 4.11: Mean velocity profile at $x = 0.1243m$

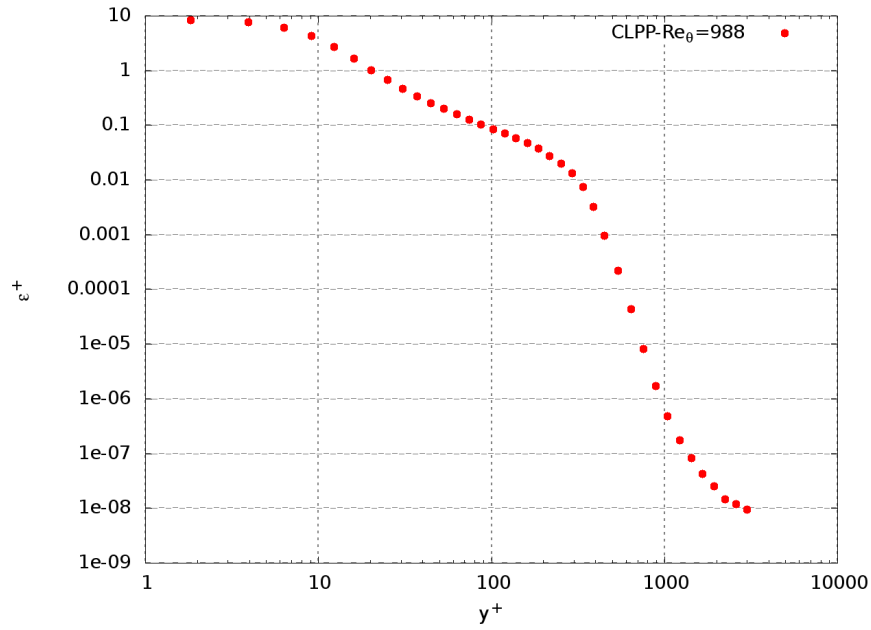Figure 4.12: Turbulent kinetic energy profile $(k^+ = k/u_\tau^2)$ at $x = 0.1243m$

Figure 4.13: Dissipation rate profile $(\epsilon^+ = \frac{\epsilon}{U_\infty^3/\delta(x=L_x)})$ at $x = 0.1243m$
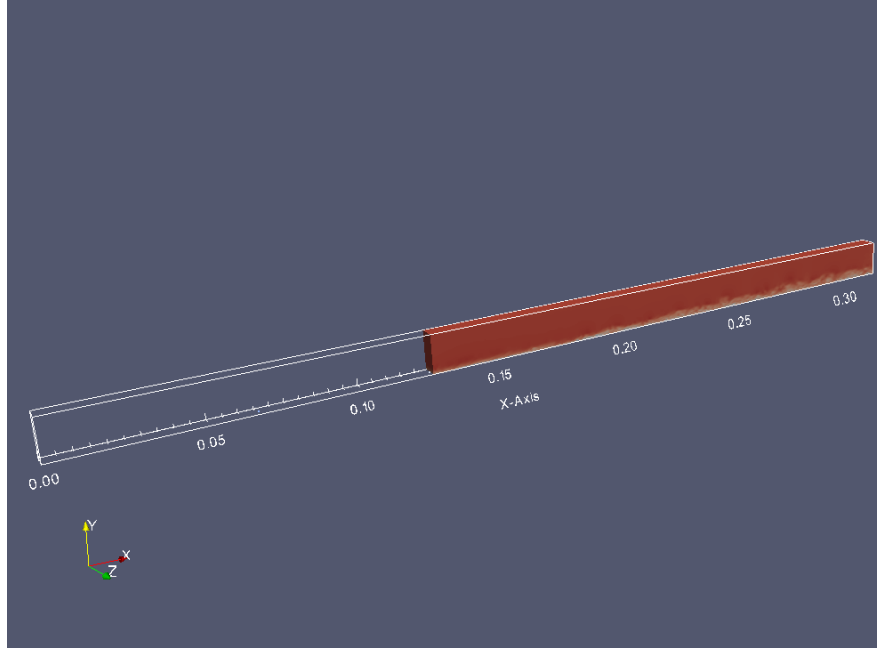
Figure 4.14: Computational domain for LES with improved vortex method - CLVM

Mesh configuration

The simulation domain for CLVM is also extracted from the reference LES (from $x = 0.1243$ to the outlet). The computational domain is $0.1865m$ long in the streamwise direction, $L_y = 11.7mm$ high at the outlet and $L_z = 5.88mm$ wide in the spanwise direction. A $-0.5°$ angle is imposed on the upper boundary, as shown in Fig. 4.14. The outline region is the computational domain for the reference LES case, while the partial domain colored by streamwise velocity is for the calculation of the improved vortex method. To facilitate the comparison of results, coordinate system remains the same as reference LES - CLPP.

The mesh is composed of $505 \times 39 \times 43$ points in the streamwise, wall-normal and spanwise direction, respectively. This yields a wall resolution of about $\Delta x^+ < 80$, $\Delta y^+ < 2$, $\Delta z^+ < 30$.

Initial and Boundary conditions

The calculation is initialized with an instantaneous flow field obtained by the reference LES.

The inlet boundary condition is generated by the improved vortex method, the vortex method's parameter coefficients are shown in Tab. 4.2. A 2D fluctuating velocity field is generated by 400 vortices on the inlet plane ($x = 0.1243m$). Then the velocity fluctuations are imposed on the extracted mean velocity profile ($x = 0.1243m$) and involve in the LES computation.

The mixed pressure outlet condition is employed on the outlet boundary. Periodic condition is used in spanswise direction and the flat-plate wall is set as non-slip adiabatic wall.

It should be noticed that the parameter coefficients for the calculation CLVM is different from those of the calculation PO7 in Chapter 3. As the flow studied is different, local Reynolds number changes, the parameter coefficients need to be re-optimized. Among all vortex method's parameters, the two parameters which correspond to the vortex radius and vortex circulation are the most basic ones and need to be specified properly. Otherwise, inappropriate fluctuations may be generated and cause numerical instability problems.

The vortex radius coefficient C_1 is set as 1/80, as shown in Fig. 4.15, so that the radius size is comparable to the energy-containing scale $L = \frac{k^{1.5}}{\epsilon}$

$$\sigma = C_1 Re_{CL}^{3/4}(\nu^3/\epsilon)^{1/4} \sim L \qquad (4.5)$$

Where $Re_{CL} = \frac{U_\infty \delta(x=L_x)}{\nu}$ is the characteristic Reynolds number for boundary layer flows. Here, the characteristic length is chosen the boundary layer thickness δ at outlet ($U_\infty = 70m/s$ and $\delta(x = L_x) = 5.88mm$).

The vortex sizes of CLVM are much smaller than those of PO7. To make sure that the computation will not blow up, the circulation coefficient C_2 is set as 0.5 to weaken the exceed fluctuations generated with the smaller size vortex . C_3 and C_4 which correspond to the lifetime and the walking step length (ERW) are the same as for the case PO7 in Chapter 3.

Test Cases	Radius C_1	Circulation C_2	Lifetime C_3	Displacement ERW C_4	SW C_5
CLVM	1/80	0.5	10	1/16	-
PO7	1/4	1.2	10	1/16	-

Table 4.2: Parameter comparison between CLVM and PO7
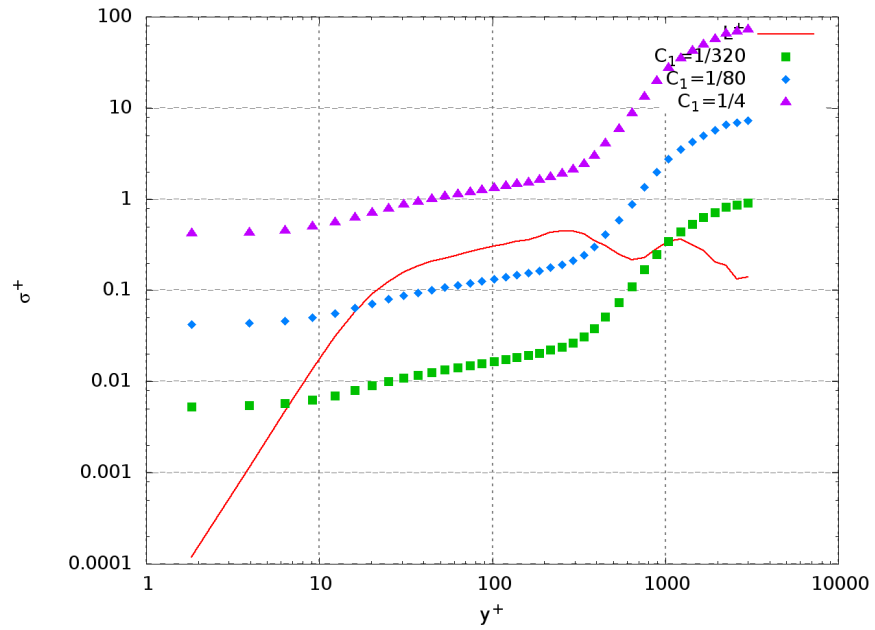
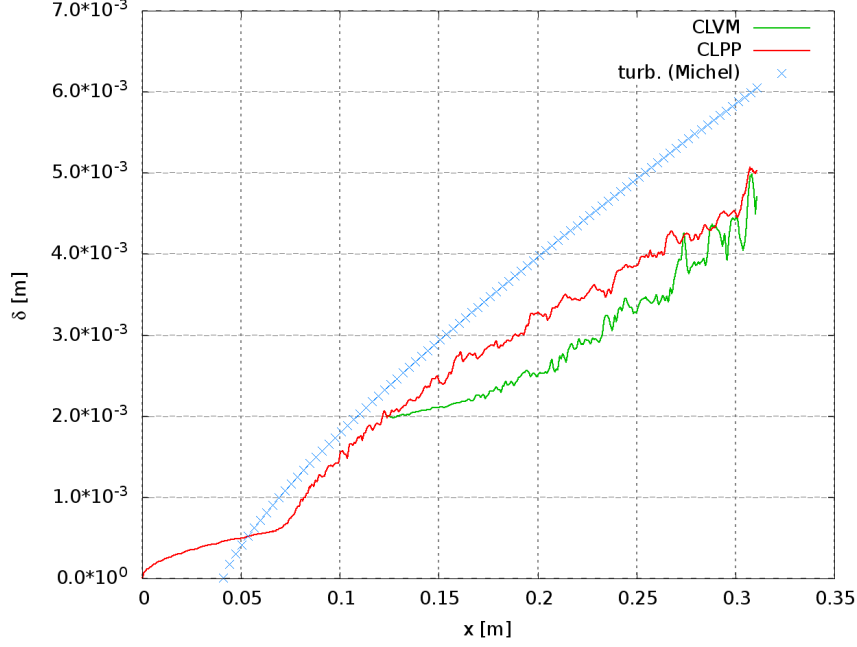Figure 4.15: Vortex radius σ along the wall-normal direction

Figure 4.16: Boundary layer thickness δ of LES with improved vortex method - CLVM

4.3.2 Results

4.3.2.1 Boundary layer evolution

The evolution of the boundary layer thickness δ, displacement thickness δ^* and momentum thickness θ are illustrated in Fig. 4.16, Fig. 4.17 and Fig. 4.18, respectively. Compared with the reference LES, CLVM underestimates the momentum thickness by about 10%. Similar behaviors are found with the results of boundary layer thickness δ and displacement thickness δ^*.

Fig. 4.19 plots the evolution of friction coefficient c_f defined as

$$c_f = 2(u_\tau/U_\infty)^2 \tag{4.6}$$

The unsteady velocity fluctuations generated by improved vortex method have a notable influence on the evolution of the friction coefficient. The friction coefficient decreases to the lowest value of 2.0×10^{-3} at about $x = 0.14m$, and then it increases. From the location $x = 0.175m$, it recovers to fully developed value
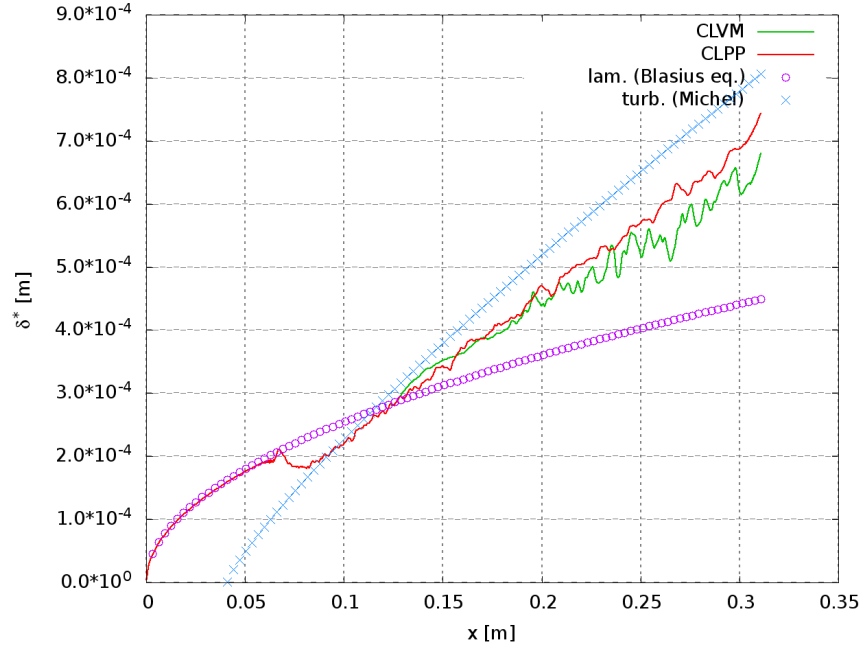
119

Figure 4.17: Displacement thickness δ^* of LES with improved vortex method - CLVM
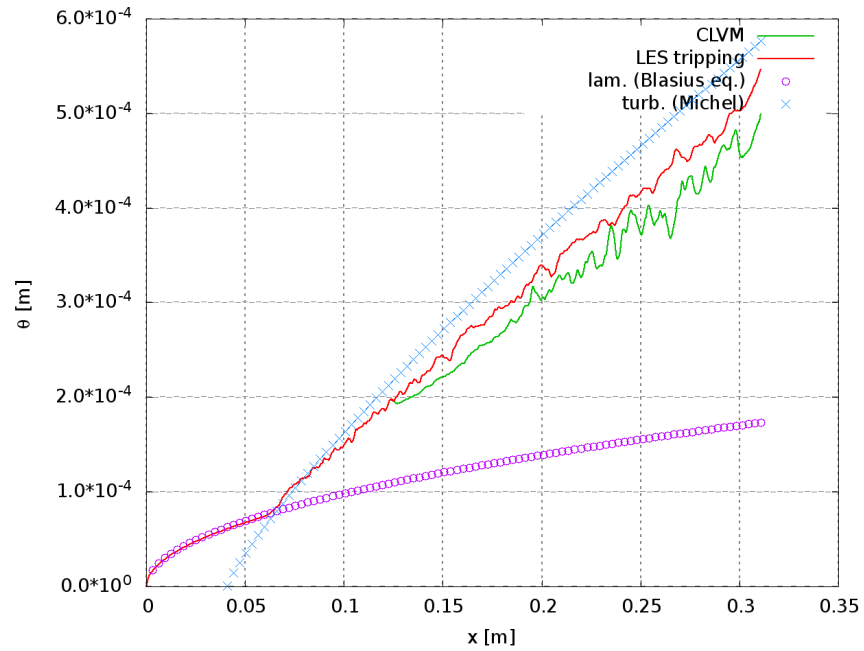

Figure 4.18: Momentum thickness θ of LES with improved vortex method - CLVM
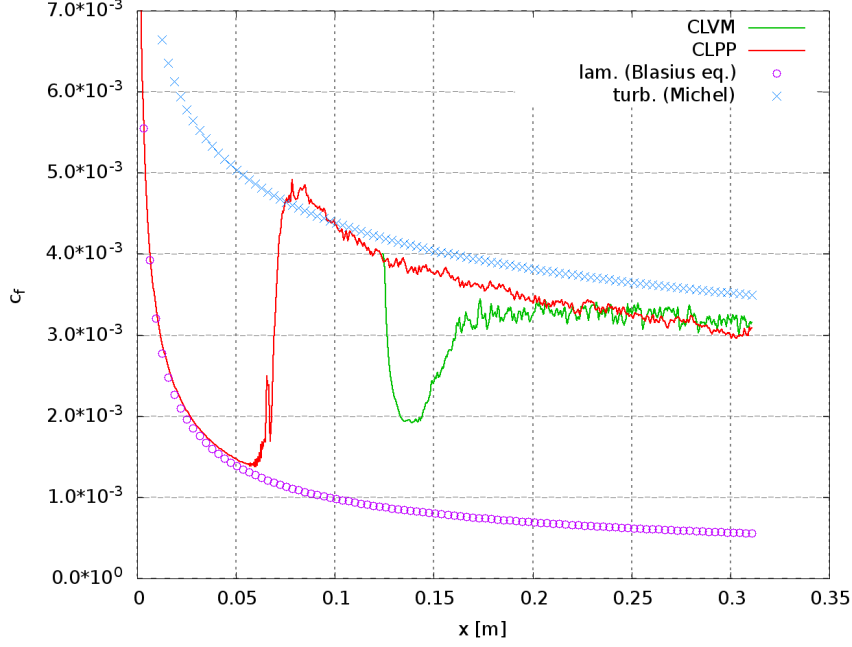
Figure 4.19: Friction coefficient c_f of LES with improved vortex method - CLVM

which agrees well with results of reference LES. Compared with law of Michel, CLVM underestimates the friction coefficient by about 12% in the fully developed region between $x = 0.175m$ and $x = 0.31m$.

4.3.2.2 Velocity-derivative skewness

Velocity-derivative skewness along the streamwise direction S_u is given in Fig. 4.20. At $y^+ = 3.4$, S_u initially oscillates around 0 near the inlet. Following the development downstream, S_u decreases. Then more pronounced oscillations are observed around $x = 0.14m$, indicating that the synthetic turbulence is in transition to real turbulence. Going further downstream, from about $x = 0.16m$, the oscillations stabilize around $S_u = -0.5$, suggesting that the exchange of energy between large- and small-scale motions is balanced with the dissipation. Fully developed boundary layer is established from this streamwise position ($x = 0.16m$). Similar behaviours are found at both the position $y^+ = 26.7$ and $y^+ = 140.5$. The velocity-derivative skewness S_u of fully developed turbulence at $y^+ = 26.7$ oscillates around -0.7 from the location $x = 0.175m$. This mean value is -0.3 for $y^+ = 140.5$

from $x = 0.18m$. The results also suggest that redevelopment to real turbulence is slower for flow further away from the flat-plate. The adaptation distance (from inlet $x = 0.1243m$ to $x = 0.175m$,which is about $0.05m$) is about 21 times the boundary layer thickness at inlet $x = 0.1243m$ ($\delta(x = 0.1243m) = 2.35mm$), the corresponding Reynolds number is $Re_\theta = 1593$.

4.3.2.3   Mean velocity and Reynolds stresses

The profiles of the mean velocity and Reynolds stresses are shown at three streamwise positions. They are drawn in Fig. 4.21 and Fig. 4.23 in comparison with the reference LES results.

At inlet, the mean velocity is directly extracted from the reference at $x = 0.1243m$, as shown in Fig. 4.21 (top). Velocity fluctuations within the inlet plane are shown in Fig. 4.23 (top). They are generated by improved vortex method, with 2D components in the spanwise direction (w'_{rms}) and the wall-normal direction (v'_{rms}). The generated 2D fluctuating velocity field at inlet is also illustrated in Fig. 4.22. Large vortex structures are viewed in the free stream while small structures show near the wall.

In the region from inlet ($x = 0.1243m$) to $x = 0.175m$, turbulence evolves and develops. At about $x = 0.175m$, the flow field gets fully developed. The mean velocity profile is well predicted in the near-wall region, and is overestimated by about 15% in the free stream.

Concerning the Reynolds stresses, the results are quite acceptable. The inner peak of $\langle u'u' \rangle$ is about 10.8, locating at $y^+ = 17.1$, which agree well with results of the reference LES. Compared with the reference LES results, $\langle w'w' \rangle$ is overestimated in the free stream by about 30% to 40%. The curves of $\langle v'v' \rangle$ and $\langle u'v' \rangle$ are well predicted by CLVM. Results of mean velocity and Reynolds profiles further confirm that the boundary layer flow get fully developed from about $x = 0.175m$.

Characteristics of the instantaneous flow field is illustrated by the Q-criterion, as shown in Fig. 4.24. As flow passes downstream, structures of turbulence tends to be smaller. From about $x = 0.175m$, both large and small structures are present, similar to what usually observed in fully developed turbulent boundary layer flows [Hall, 1982].
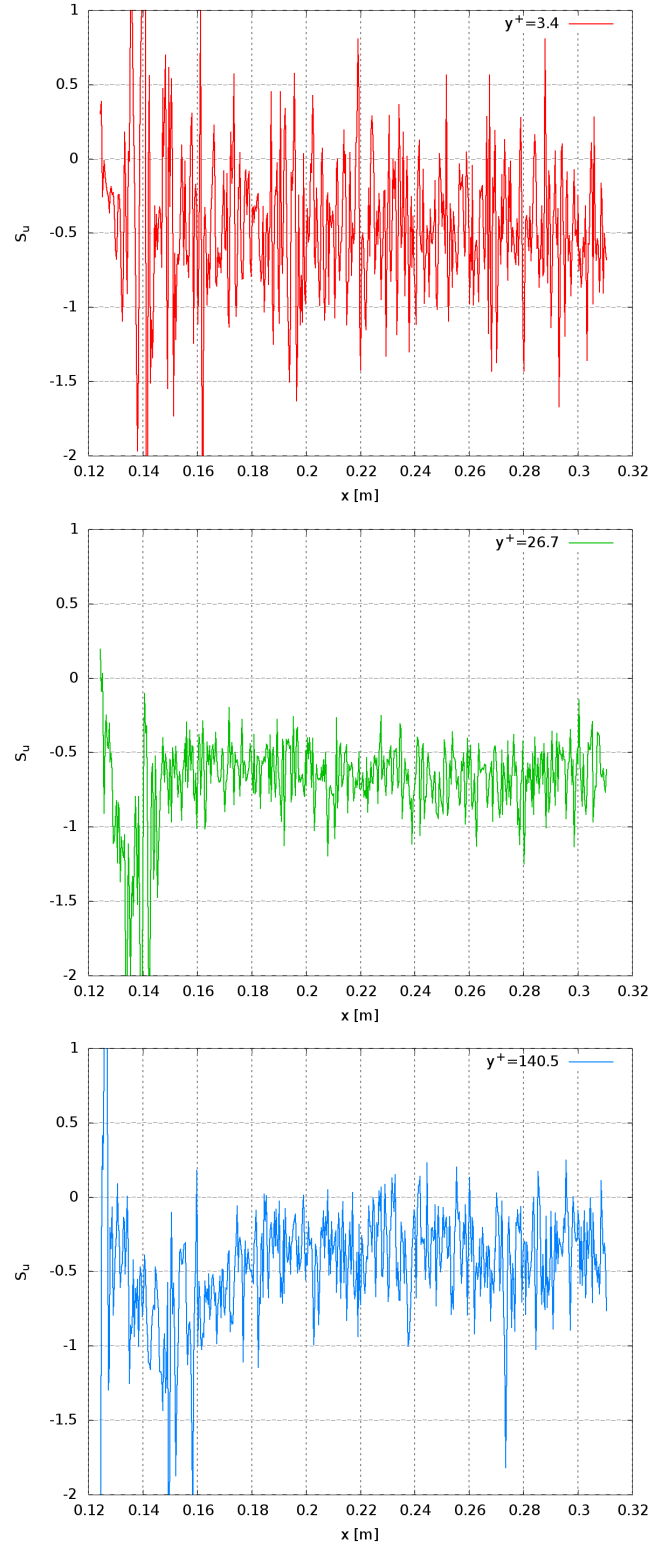
Figure 4.20: velocity-derivative skewness S_u along the streamwise direction of LES with improved vortex method - CLVM at three wall-normal positions
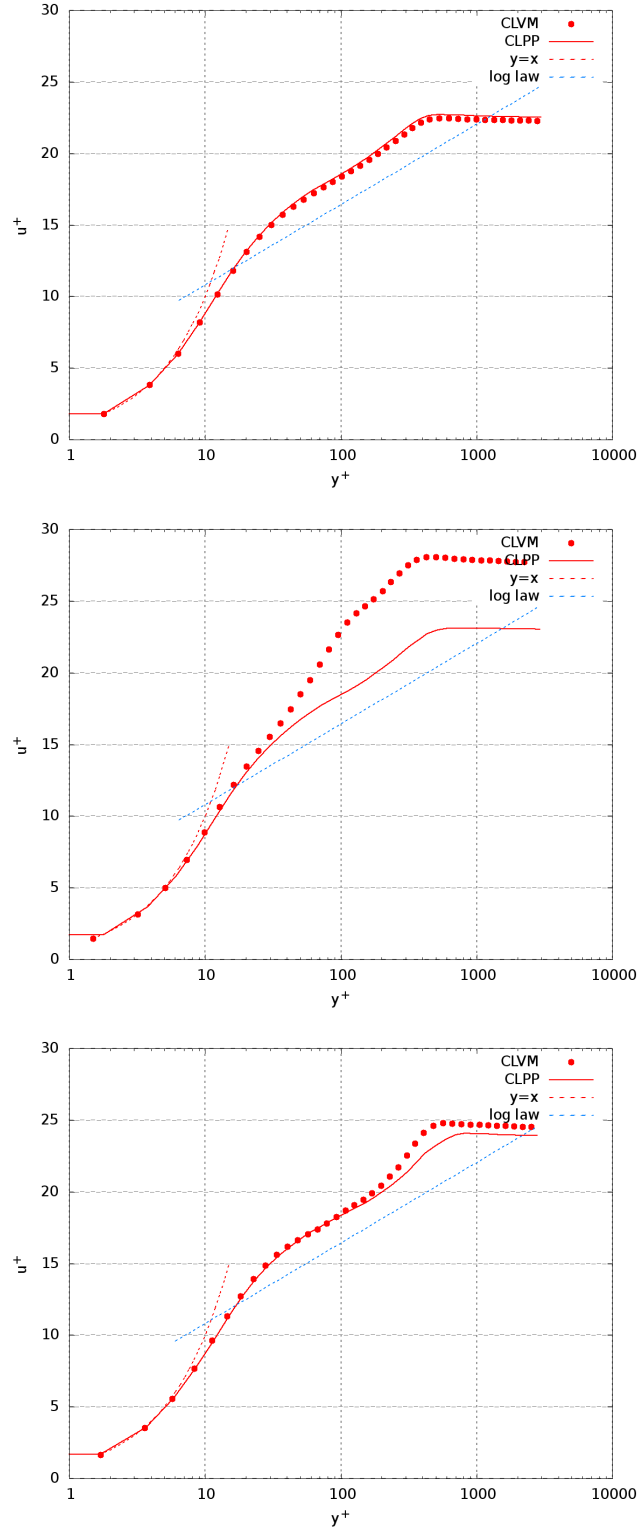
Figure 4.21: Mean velocity profile at $x = 0.1243$(top), $x = 0.1543m$(mid) and $x = 0.175m$(bottom): symbol, LES with improved vortex method - CLVM; line, reference LES - CLPP
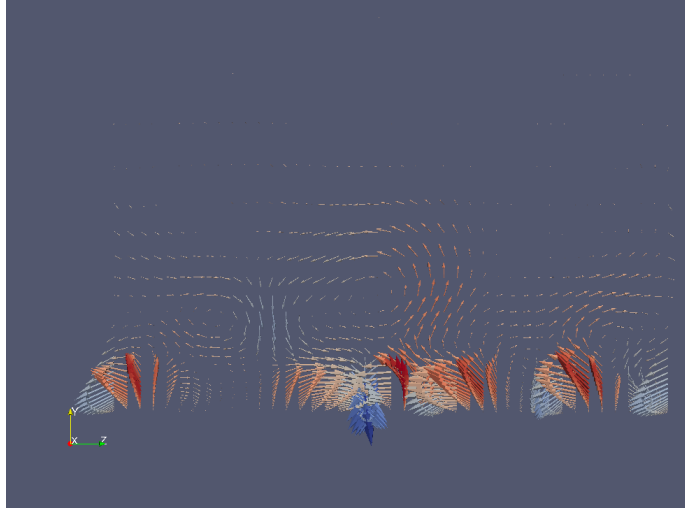
Figure 4.22: 2D velocity field at inlet $x = 0$ of LES with improved vortex method - CLVM

4.3.2.4 Conclusion

A LES of flat-plate turbulent boundary layer toward $Re_\theta = 1968$, including transition forced by a trip, has been conducted as a reference computation. Profiles of mean velocity, turbulent kinetic energy and dissipation rate are extracted at $Re_\theta = 1593$ from the reference LES to apply the improved vortex method. The evolution of the friction coefficient and velocity-derivative skewness indicate a very effective transition process (a very short adaptation distance, 21δ) from synthetic turbulence to real turbulence. Especially, the velocity-derivative skewness suggests that the exchange of energy between large- and small-scale motions are quickly rebalanced in the fully developed zone. Good agreement with the reference data further confirms that the improved vortex method is effective for boundary layer simulations.

Figure 4.23: Reynolds stress at $x = 0.1243$(top), $x = 0.1543m$(mid) and $x = 0.175m$(bottom): symbol, LES with improved vortex method - CLVM; line, reference LES - CLPP
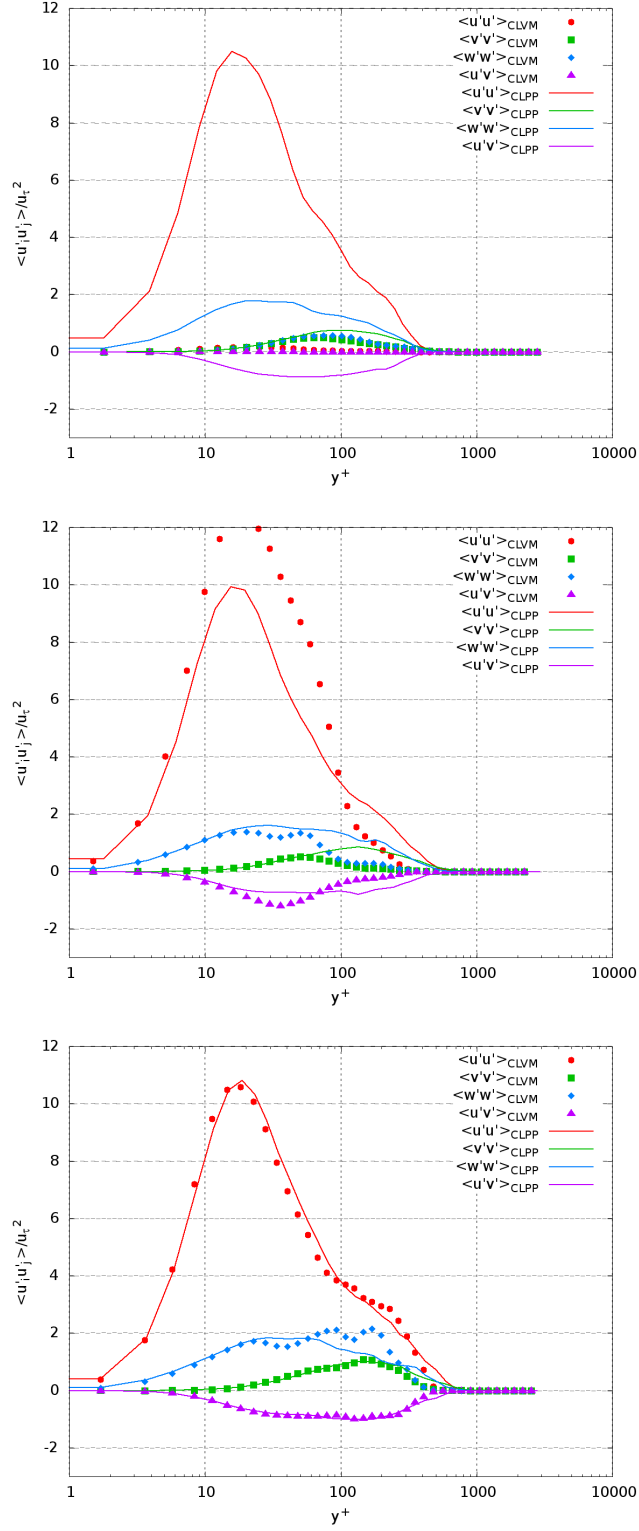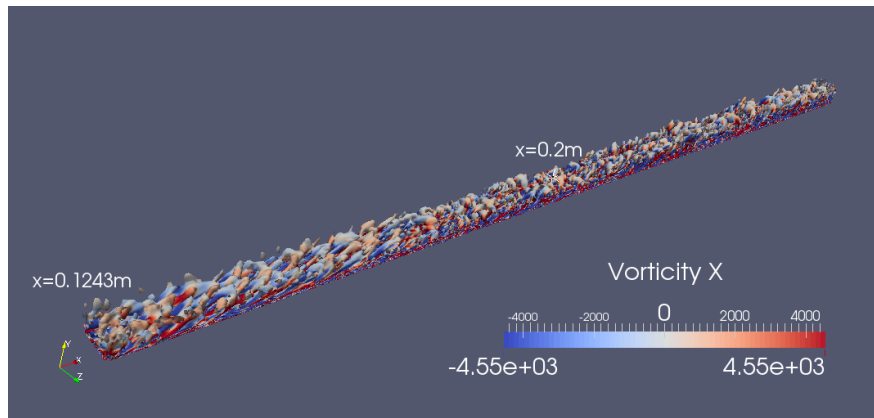
Figure 4.24: Isosurface of Q criterion (Q=200000) colored by the streamwise vorticity of LES with improved vortex method - CLVM

Chapter 5

Conclusions and Perspectives

The present thesis study and improves the vortex method used in LES for generating inflow conditions which is one of the most important issues for industrial application of LES. Tremendous numerical experiments, in channel and flat-plate flows, have been performed. In both cases, with the aim to provide reference data for present study, classic LES are conducted first and well compared to DNS. Using the same flow configurations, results of spatially developing LES with improved vortex method are then checked against these reference data. In order to better qualify the results of LES, we also introduce a new criterion which is based on velocity derivative skewness.

Parameter optimization and its validation on an academic channel flow $Re_\tau = 395$ has demonstrated that the improved vortex method can significantly decrease the required adaption distance. Within a development length of about $6h$ (h being the half channel height) downstream of the inlet, the friction coefficient, mean velocity and the Reynolds stress profiles achieve excellent agreement with those of reference computation. We recall that with the original vortex method proposed by Sergent [2002], Benhamadouche et al. [2006] shows that RMS profiles have an appropriate behavior from $x/h = 12$. In comparison, the synthetic-eddy method developed by Jarrin et al. [2009] and used by Poletto et al. [2013], requires at least $10h$ adaptation distance to correctly achieve fully developed channel flows.

The development of turbulence is further confirmed by checking the behaviour of the velocity-derivative skewness. Similar to what usually observed in experiments of grid turbulence or DNS, downstream of inlet, calculations with the inflow

conditions generated by the improved vortex method show that the development of turbulence is closely linked with the velocity-derivative skewness. Within the adaptation distance, the value of derivative skewness originates from 0, then decreases and increases to certain negative level. Finally, after the adaptation distance, it stabilizes around a negative value about -0.5 in the fully developed turbulence region. It indicates that the energy transfer between different scales is balanced with the turbulent dissipation. Meanwhile, it is observed that the friction coefficient behaves in a similar way and recovers to the expected value. Thus we propose to use the velocity-derivative skewness as a new criterion to qualify LES results.

In summary, the improved vortex method considers five parameters: 1) vortex radius, 2) vortex circulation, 3) vortex lifetime, and 4) enhanced random walk or 5) stochastic walk.

Among those parameters:

1. Vortex radius is based on local energy-containing scale which is related to local dissipation rate. Too large vortex radius sizes lead to relaminarization of the flow, while too small vortex radius sizes can hardly be resolved. A practical method which uses the dimensionless local dissipation rate is proposed in this thesis to optimize the coefficient of radius.

2. Vortex circulation is modelled according to the turbulent kinetic energy. Its magnitude can be tuned with an amplification factor. So generated turbulent kinetic energy should present a level comparable to what expected.

3. Vortex lifetime is related to the period for a vortex to inverse its direction. The vortex lifetime should be comparable with or larger than the turbulent time scale.

4. Enhanced random walk refers to the movement type of a vortex. Its step length is comparable with, but smaller than, the vortex radius. Present study shows that 1/16 of the vortex radius is adequate.

5. Stochastic walk. This is an alternative of the enhanced random walk. The displacement velocity is generated by Langevin equations. However, we

don't recommend this method because the enhanced random walk is simpler and gives similar good results.

Success of the improved vortex method used in LES of both channel flow and flat plate boundary layer flow, demonstrate that this method is able to be applied to both internal and external flows. With the improved vortex method imposed at inlet, both test cases show very good results in comparison with the reference data. The establishment of turbulence is faster compared to other existed methods. The improved vortex method has a great potential to be applied in more complex geometries.

A. Velocity-derivative skewness and inter-scale energy transfer

Following Batchelor [1953]Lumley et al. [2007]Tavoularis et al. [1978] and Bos et al. [2012], relation between the nonlinear transfer and the third-order longitudinal velocity structure function D_{LLL} will be given in this appendix. Therefore, the relation between velocity-derivative skewness and transfer of energy between different scales can be draw clearly.

Derivation of the Lin-equation

Starting from the velocity fluctuation N-S equations for incompressible flow,

$$\frac{\partial u_i(\boldsymbol{x})}{\partial t} + u_j(\boldsymbol{x})\frac{\partial u_i(\boldsymbol{x})}{\partial x_j} = -\frac{1}{\rho}\frac{\partial p(\boldsymbol{x})}{\partial x_i} + \nu\frac{\partial^2 u_i(\boldsymbol{x})}{\partial x_j \partial x_j} \tag{1}$$

The three-dimensional Fourrier transfer is

$$u_i(\boldsymbol{\kappa}) = \frac{1}{(2\pi)^3}\int u_i(\boldsymbol{x})e^{-i\boldsymbol{\kappa}\cdot\boldsymbol{x}}d\boldsymbol{x} \tag{2}$$

In Fourrier space, the N-S equations can be written

$$\frac{\partial u_i(\boldsymbol{\kappa})}{\partial t} + \nu\kappa^2 u_i(\boldsymbol{\kappa}) = -\frac{i}{2}P_{ijm}(\boldsymbol{\kappa})\int\int u_j(\boldsymbol{p})u_m(\boldsymbol{q})\delta(\boldsymbol{\kappa}-\boldsymbol{p}-\boldsymbol{q})d\boldsymbol{p}d\boldsymbol{q} \tag{3}$$

Where

$$P_{ijm}(\boldsymbol{\kappa}) = \kappa_j P_{im}(\boldsymbol{\kappa}) + \kappa_m P_{ij}(\boldsymbol{\kappa}) \tag{4}$$

$$P_{ij}(\boldsymbol{\kappa}) = \delta_{ij} - \frac{\kappa_i \kappa_j}{\kappa^2} \tag{5}$$

In isotropic turbulence, the energy spectrum is

$$E(\kappa) = 2\pi\kappa^2 \langle u_i(\boldsymbol{\kappa})u_i(-\boldsymbol{\kappa})\rangle \tag{6}$$

Then, the evolution for $E(\kappa)$ can be deduced from N-S equations in Fourrier space

$$[\frac{\partial}{\partial t} + 2\nu\kappa^2]E(\kappa) = i\pi\kappa^2 P_{ijm}(\boldsymbol{\kappa})[T_{ijm}(\boldsymbol{\kappa}) - T_{ijm}^*(\boldsymbol{\kappa})] = T(\kappa) \tag{7}$$

where

$$T_{ijm}(\boldsymbol{\kappa}) = \int\int \langle u_i(\boldsymbol{\kappa})u_j(\boldsymbol{p})u_m(\boldsymbol{q})\rangle\delta(\boldsymbol{\kappa}+\boldsymbol{p}+\boldsymbol{q}))d\boldsymbol{p}d\boldsymbol{q} \tag{8}$$

$$T_{ijm}^*(\boldsymbol{\kappa}) = \int\int \langle u_i(-\boldsymbol{\kappa})u_j(-\boldsymbol{p})u_m(-\boldsymbol{q})\rangle\delta(\boldsymbol{\kappa}+\boldsymbol{p}+\boldsymbol{q}))d\boldsymbol{p}d\boldsymbol{q} \tag{9}$$

For isotropic flow, $T_{ijm}^*(\boldsymbol{\kappa}) = -T_{ijm}(\boldsymbol{\kappa})$.

Relation between energy spectrum and structure function

The second order longitudinal structure function is

$$D_{LL}(r) = \langle \delta u_L^2 \rangle \tag{10}$$

where

$$\delta u_L = u_L - u_L' = \frac{r_i}{r}u_i(\boldsymbol{x}) - \frac{r_i}{r}u_i(\boldsymbol{x}+\boldsymbol{r}) \tag{11}$$

The relation between D_{LL} and energy spectrum $E(\kappa)$ is

$$D_{LL} = \int E(\kappa)f(\kappa r)d\kappa \tag{12}$$

Where

$$f(x) = 4[\frac{1}{3} - \frac{sinx - xcosx}{x^3}] \tag{13}$$

Relation between transfer spectrum and structure function

The third order longitudinal structure function in homogeneous turbulence is

$$D_{LLL}(r) = \langle \delta u_L^3 \rangle = 3(\langle u_L u_L'^2 \rangle - \langle u_L' u_L^2 \rangle) \tag{14}$$

It is related to the transfer spectrum by

$$D_{LLL}(r) = r \int_0^\infty T(\kappa)g(\kappa r)d\kappa \tag{15}$$

With

$$g(x) = 12\frac{3(sinx - xcosx) - x^2 sinx}{x^5} \tag{16}$$

Or the transfer spectrum is computed by D_{LLL} as

$$T(\kappa) = \frac{\kappa}{6\pi} \int \frac{sin(\kappa r)}{r} \frac{\partial}{\partial r}[\frac{1}{r}\frac{\partial}{\partial r}(r^4 D_{LLL}(r))]dr \tag{17}$$

Small scale behavior of structure function

When $x \to 0$, function (13) and function (16) tends to

$$f(x) = \frac{2}{15}x^2 + \mathcal{O}(x^3) \tag{18}$$

$$g(x) = \frac{4}{5} - \frac{2}{35}x^2 + \mathcal{O}(x^4) \tag{19}$$

Thus for very small r,

$$D_{LL}(r) = \frac{2}{15}r^2 \int \kappa^2 E(\kappa)d\kappa = \frac{\epsilon r^2}{15\nu} \tag{20}$$

$$D_{LLL}(r) = \frac{4}{5}r \int T(\kappa)d\kappa - \frac{2}{35}r^3 \int \kappa^2 T(\kappa)d\kappa = -\frac{2}{35}r^3 \int \kappa^2 T(\kappa)d\kappa \tag{21}$$

The velocity-derivative skewness is defined as

$$S(r) = \frac{D_{LLL}}{D_{LL}^{3/2}} \tag{22}$$

When at very small scales

$$\delta u_L \simeq r\frac{\partial u}{\partial x} \tag{23}$$

Thus, another form for the velocity-derivative skewness is

$$\lim_{r\to 0} S(r) = \frac{\langle(\partial u/\partial x)^3\rangle}{\langle(\partial u/\partial x)^2\rangle^{3/2}} \tag{24}$$

Appendix . A. Velocity-derivative skewness and inter-scale energy transfer

Using Eq. (20),Eq. (21) and Eq. (22), we have

$$\lim_{r \to 0} S(r) = \frac{\langle (\partial u/\partial x)^3 \rangle}{\langle (\partial u/\partial x)^2 \rangle^{3/2}} = -\frac{15^{3/2}}{35\sqrt{2}} \frac{\int \kappa^2 T(\kappa) d\kappa}{[\int \kappa^2 E(\kappa) d\kappa]^3} \tag{25}$$

Considering the situation when energy transfer and dissipation is balanced, we have

$$\int \kappa^2 T(\kappa) d\kappa \simeq \int 2\nu\kappa^4 E(\kappa) d\kappa \tag{26}$$

So that

$$\lim_{r \to 0} S(r) \simeq -\frac{15^{3/2}\sqrt{2}}{35} \frac{\int \kappa^4 E(\kappa) d\kappa}{[\int \kappa^2 E(\kappa) d\kappa]^3} \tag{27}$$

Since $E(\kappa)$ depends on Reynolds number, thus, the velocity-derivative skewness becomes a function of the Reynolds number. For a turbulence flow at a certain Reynolds number, when the process of energy cascade is established or when turbulence is fully developed. The transfer of energy from large scale to small scale is balanced to the dissipation rate at the smallest scale (Kolmogorov scale η), the velocity-derivative skewness should be constant. Thus it may be seen as a criterion for determining if turbulence is fully developed.

References

Knut Akselvoll and Parviz Moin. Large-eddy simulation of turbulent confined coannular jets. *Journal of Fluid Mechanics*, 315:387–411, 1996. 17

Giancarlo Alfonsi. Reynolds-averaged navier–stokes equations for turbulence modeling. *Applied Mechanics Reviews*, 62(4):040802, 2009. 3

K Alvelius. Random forcing of three-dimensional homogeneous turbulence. *Physics of Fluids (1994-present)*, 11(7):1880–1889, 1999. 32

RA Antonia, AJ Chambers, and BR Satyaprakash. Reynolds number dependence of high-order moments of the streamwise turbulent velocity derivative. *Boundary-Layer Meteorology*, 21(2):159–171, 1981. 50

Barrett Stone Baldwin and Harvard Lomax. *Thin layer approximation and algebraic model for separated turbulent flows*, volume 257. American Institute of Aeronautics and Astronautics, 1978. 14

Jorge Bardina, Joel H Ferziger, and WC Reynolds. Improved subgrid-scale models for large-eddy simulation. In *American Institute of Aeronautics and Astronautics, Fluid and Plasma Dynamics Conference, 13th, Snowmass, Colo., July 14-16, 1980, 10 p.*, volume 1, 1980. 20

George Keith Batchelor. *The theory of homogeneous turbulence*. Cambridge university press, 1953. 7, 24, 48, 133

Paul Batten, Uriel Goldberg, and Sukumar Chakravarthy. Interfacing statistical turbulence closures with large-eddy simulation. *AIAA journal*, 42(3):485–492, 2004. 6, 25

Sofiane Benhamadouche, Nicolas Jarrin, Yacine Addad, and Dominique Laurence. Synthetic turbulent inflow conditions based on a vortex method for large-eddy simulation. *Progress in Computational Fluid Dynamics, an International Journal*, 6(1-3):50–57, 2006. 5, 6, 25, 26, 29, 31, 34, 96, 129

Jean-Pierre Bertoglio. A stochastic subgrid model for sheared turbulence. In *Macroscopic modelling of turbulent flows*, pages 100–119. Springer, 1985. 44

Wouter JT Bos, Laurent Chevillard, Julian F Scott, and Robert Rubinstein. Reynolds number effect on the velocity increment skewness in isotropic turbulence. *Physics of Fluids (1994-present)*, 24(1):015108, 2012. 48, 133

Jérôme Boudet, J-F Monier, and Feng Gao. Implementation of a roughness element to trip transition in large-eddy simulation. *Journal of Thermal Science*, 24(1):30–36, 2015. 103, 104, 106

P Bradshaw. Possible origin of prandt's mixing-length theory. 1974. 13

Paolo Burattini, Philippe Lavoie, and Robert A Antonia. Velocity derivative skewness in isotropic turbulence and its measurement with hot wires. *Experiments in fluids*, 45(3):523–535, 2008. 49

Adrien Cahuzac, Jérôme Boudet, MC Jacob, and Ph Kausche. Large-eddy simulation of a rotor tip-clearance flow. *AIAA Paper*, (2011-2947), 2011. 20

Jeffrey R Chasnov. Simulation of the kolmogorov inertial subrange using an improved subgrid model. *Physics of Fluids A: Fluid Dynamics (1989-1993)*, 3 (1):188–200, 1991. 17

Kuei-Yuan Chien. Predictions of channel and boundary-layer flows with a low-reynolds-number turbulence model. *AIAA journal*, 20(1):33–38, 1982. 14

Genevieve Comte-Bellot and Stanley Corrsin. The use of a contraction to improve the isotropy of grid-generated turbulence. *Journal of Fluid Mechanics*, 25(04): 657–682, 1966. 32

Geneviève Comte-Bellot and Antoine Craya. Ecoulement turbulent entre deux parois paralleles. 1965. 49

References

James W Deardorff. A numerical study of three-dimensional turbulent channel flow at large reynolds numbers. *Journal of Fluid Mechanics*, 41(02):453–480, 1970. 17

James W Deardorff. Three-dimensional numerical study of the height and mean structure of a heated planetary boundary layer. *Boundary-Layer Meteorology*, 7(1):81–106, 1974. 17

Sébastien Deck, Pierre-Élie Weiss, Mathieu Pamies, and Eric Garnier. Zonal detached eddy simulation of a spatially developing flat plate turbulent boundary layer. *Computers & Fluids*, 48(1):1–15, 2011. 6

Hugh L Dryden. Review of published data on the effect of roughness on transition from laminar to turbulent flow. *Journal of the Aeronautical Sciences*, 2012. 106

V Eswaran and SB Pope. An examination of forcing in direct numerical simulations of turbulence. *Computers & Fluids*, 16(3):257–278, 1988. 32

Boris Galperin. *Large eddy simulation of complex engineering and geophysical flows*. Cambridge University Press, 1993. 17

Feng Gao. *Advanced numerical simulation of corner separation in a linear compressor cascade*. PhD thesis, Ecole Centrale de Lyon, 2014. 20

Feng Gao, Wei Ma, Gherardo Zambonini, Jérôme Boudet, Xavier Ottavy, Lipeng Lu, and Liang Shao. Large-eddy simulation of 3-d corner separation in a linear compressor cascade. *Physics of Fluids (1994-present)*, 27(8):085105, 2015. 17, 23

Michael J Gelb. *How to think like Leonardo da Vinci: Seven steps to genius every day*. Dell, 2009. 1

A Gylfason, S Ayyalasomayajula, and Z Warhaft. Intermittency, pressure and acceleration statistics from hot-wire measurements in wind-tunnel turbulence. *Journal of Fluid Mechanics*, 501:213–229, 2004. 49, 50

P Hall. Taylor—gortler vortices in fully developed or boundary-layer flows: linear theory. *Journal of Fluid Mechanics*, 124:475–494, 1982. 122

Fujihiro Hamba. A hybrid rans/les simulation of turbulent channel flow. *Theoretical and computational fluid dynamics*, 16(5):387–403, 2003. 4

DC Haworth and K Jansen. Large-eddy simulation on unstructured deforming meshes: towards reciprocating ic engines. *Computers & fluids*, 29(5):493–524, 2000. 17

Robert Jason Hearst and Philippe Lavoie. Velocity derivative skewness in fractal-generated, non-equilibrium grid turbulence. *Physics of Fluids (1994-present)*, 27(7):071701, 2015. 91

Reginald J Hill. Exact second-order structure-function relationships. *Journal of Fluid Mechanics*, 468:317–326, 2002. 49, 50

Julian CR Hunt, Alan A Wray, and Parviz Moin. Eddies, streams, and convergence zones in turbulent flows. *Report CTR-S88*, 1988. 99

Takashi Ishihara, Yukio Kaneda, Mitsuo Yokokawa, Ken'ichi Itakura, and Atsuya Uno. Small-scale statistics in high-resolution direct numerical simulation of turbulence: Reynolds number dependence of one-point velocity gradient statistics. *Journal of Fluid Mechanics*, 592:335–366, 2007. 49, 50

Antony Jameson. Transonic airfoil calculations using the euler equations. In *in Numerical Methods in Aeronautical Fluid Dynamics*. Citeseer, 1982. 21

N Jarrin, R Prosser, J-C Uribe, S Benhamadouche, and D Laurence. Reconstruction of turbulent fluctuations for hybrid rans/les simulations using a synthetic-eddy method. *International Journal of Heat and Fluid Flow*, 30(3):435–442, 2009. 5, 6, 25, 96, 129

Jinhee Jeong, Fazle Hussain, Wade Schoppa, and John Kim. Coherent structures near the wall in a turbulent channel flow. *Journal of Fluid Mechanics*, 332: 185–214, 1997. 96, 99

Forrester T Johnson, Edward N Tinoco, and N Jong Yu. Thirty years of development and application of cfd at boeing commercial airplanes, seattle. *Computers & Fluids*, 34(10):1115–1151, 2005. 2

References

Anthony Keating, Ugo Piomelli, Elias Balaras, and Hans-Jakob Kaltenbach. A priori and a posteriori tests of inflow conditions for large-eddy simulation. *Physics of Fluids (1994-present)*, 16(12):4696–4712, 2004. 4, 24

Andrey Nikolaevich Kolmogorov. Dissipation of energy in locally isotropic turbulence. In *Dokl. Akad. Nauk SSSR*, volume 32, pages 16–18. JSTOR, 1941. 3

Robert H Kraichnan. Kolmogorov's hypotheses and eulerian turbulence theory. *Physics of Fluids (1958-1988)*, 7(11):1723–1734, 1964. 1

Robert H Kraichnan. Eddy viscosity in two and three dimensions. *Journal of the atmospheric sciences*, 33(8):1521–1536, 1976. 17

Emmanuel Labourasse and Pierre Sagaut. Reconstruction of turbulent fluctuations using a hybrid rans/les approach. *Journal of Computational Physics*, 182 (1):301–336, 2002. 25

Romain Laraufie, Sébastien Deck, and Pierre Sagaut. A dynamic forcing method for unsteady turbulent inflow conditions. *Journal of Computational Physics*, 230(23):8647–8663, 2011. 6, 24

Brian Edward Launder and DB Spalding. The numerical computation of turbulent flows. *Computer methods in applied mechanics and engineering*, 3(2): 269–289, 1974. 16

Sangsan Lee, Sanjiva K Lele, and Parviz Moin. Simulation of spatially evolving turbulence and the applicability of taylor's hypothesis in compressible flow. *Physics of Fluids A: Fluid Dynamics (1989-1993)*, 4(7):1521–1530, 1992. 24

Anthony Leonard. Vortex methods for flow simulation. *Journal of Computational Physics*, 37(3):289–335, 1980. 6, 25

Emmanuel Lévêque, Federico Toschi, Liang Shao, and J-P Bertoglio. Shear-improved smagorinsky model for large-eddy simulation of wall-bounded turbulent flows. *Journal of Fluid Mechanics*, 570:491–502, 2007. 20

Douglas K Lilly. A proposed modification of the germano subgrid-scale closure method. *Physics of Fluids A: Fluid Dynamics (1989-1993)*, 4(3):633–635, 1992. 20

Kunlun Liu and Richard H Pletcher. Inflow conditions for the large eddy simulation of turbulent boundary layers: a dynamic recycling procedure. *Journal of Computational Physics*, 219(1):1–6, 2006. 5

John Leask Lumley et al. *Statistical fluid mechanics: mechanics of turbulence*, volume 1. Courier Corporation, 2007. 1, 48, 133

Thomas S Lund, Xiaohua Wu, and Kyle D Squires. Generation of turbulent inflow data for spatially-developing boundary layer simulations. *Journal of Computational Physics*, 140(2):233–258, 1998. 5, 24

Fabrice Mathey. Aerodynamic noise simulation of the flow past an airfoil trailing-edge using a hybrid zonal rans-les. *Computers & Fluids*, 37(7):836–843, 2008. 4, 25, 26

Fabrice Mathey, Davor Cokljat, Jean Pierre Bertoglio, and Emmanuel Sergent. Assessment of the vortex method for large eddy simulation inlet conditions. *Progress in Computational Fluid Dynamics, An International Journal*, 6(1-3): 58–67, 2006. 5, 6, 25, 34, 35

DJ Maull. An introduction to the discrete vortex method. *NASA STI/Recon Technical Report A*, 81:27614, 1980. 6, 25

Charles Meneveau, Thomas S Lund, and William H Cabot. A lagrangian dynamic subgrid-scale model of turbulence. *Journal of Fluid Mechanics*, 319:353–385, 1996. 20

Parviz Moin and John Kim. Numerical investigation of turbulent channel flow. *Journal of fluid mechanics*, 118:341–377, 1982. 17

Parviz Moin and Krishnan Mahesh. Direct numerical simulation: a tool in turbulence research. *Annual review of fluid mechanics*, 30(1):539–578, 1998. 2, 53

References

Andrea Montorfano, Federico Piscaglia, and G Ferrari. Inlet boundary conditions for incompressible les: A comparative study. *Mathematical and Computer Modelling*, 57(7):1640–1647, 2013. 7

Brandon Morgan, Johan Larsson, Soshi Kawai, and Sanjiva K Lele. Improving low-frequency characteristics of recycling/rescaling inflow turbulence generation. *AIAA journal*, 49(3):582–597, 2011. 5

Robert D Moser, John Kim, and Nagi N Mansour. Direct numerical simulation of turbulent channel flow up to re= 590. *Phys. Fluids*, 11(4):943–945, 1999. 52

Franck Nicoud and Frédéric Ducros. Subgrid-scale stress modelling based on the square of the velocity gradient tensor. *Flow, turbulence and Combustion*, 62 (3):183–200, 1999. 20

Shoiti Nisizima and Akira Yoshizawa. Turbulent channel and couette flows using an anisotropic k-epsilon model. *AIAA journal*, 25(3):414–420, 1987. 14

Steven A Orszag and GS Patterson Jr. Numerical simulation of three-dimensional homogeneous isotropic turbulence. *Physical Review Letters*, 28(2):76, 1972. 9, 10

Mathieu Pamies, Pierre-Elie Weiss, Eric Garnier, Sebastien Deck, and Pierre Sagaut. Generation of synthetic turbulent inflow data for large eddy simulation of spatially evolving wall-bounded flows. *Physics of Fluids (1994-present)*, 21 (4):045103, 2009. 5, 6

Ugo Piomelli and Jeffrey Robert Chasnov. Large-eddy simulations: theory and applications. In *Turbulence and transition modelling*, pages 269–336. Springer, 1996. 3

Ugo Piomelli, JOELH FERZIGER, and Parviz Moin. Model consistency in large eddy simulation of turbulent channel flows. *Physics of Fluids*, 31(7):1884, 1988. 17

R Poletto, T Craft, and A Revell. A new divergence free synthetic eddy method for the reproduction of inlet flow conditions for les. *Flow, turbulence and combustion*, 91(3):519–539, 2013. 96, 129

Stephen B Pope. Turbulent flows, 2001. 13, 41, 60

Osborne Reynolds. An experimental investigation of the circumstances which determine whether the motion of water shall be direct or sinuous, and of the law of resistance in parallel channels. *Proceedings of the royal society of London*, 35(224-226):84–99, 1883. 1

Robert S Rogallo and Parviz Moin. Numerical simulation of turbulent flows. *Annual Review of Fluid Mechanics*, 16(1):99–137, 1984. 2

Robert Sugden Rogallo. Numerical experiments in homogeneous turbulence. *Technical Report TM81315*, 1981. 10

L Rosenhead. The formation of vortices from a surface of discontinuity. *Proceedings of the Royal Society of London. Series A, Containing Papers of a Mathematical and Physical Character*, 134(823):170–192, 1931. 6, 25

Pierre Sagaut. *Large eddy simulation for incompressible flows: an introduction.* Springer Science & Business Media, 2006. 3

Pierre Sagaut, Eric Garnier, Eric Tromeur, Lionel Larchevêque, and Emmanuel Labourasse. Turbulent inflow conditions for les of supersonic and subsonic wall bounded flows. *AIAA Paper*, 68, 2003. 4

Pierre Sagaut, Sebastien Deck, and Marc Terracol. *Multiscale and multiresolution approaches in turbulence: LES, DES and hybrid RANS/LES methods: applications and guidelines.* World Scientific, 2013. 4

Herrmann Schlichting and Klaus Gersten. *Boundary-layer theory.* Springer Science & Business Media, 2003. 104, 106, 107

François G Schmitt. About boussinesq's turbulent viscosity hypothesis: historical remarks and a direct evaluation of its validity. *Comptes Rendus Mécanique*, 335(9):617–627, 2007. 12

Ulrich Schumann. Subgrid scale model for finite difference simulations of turbulent flows in plane channels and annuli. *Journal of computational physics*, 18 (4):376–404, 1975. 17

References

Emmanuel Sergent. *Vers une méthodologie de couplage entre la Simulation des Grandes Echelles et les modèles statistiques.* PhD thesis, Ecully, Ecole Centrale de Lyon, 2002. 6, 7, 25, 26, 29, 30, 31, 34, 38, 40, 43, 59, 62, 70, 96, 129

L Shao, S Sarkar, and C Pantano. Rapid and slow subgrid stress tensor in les of complex turbulent flow. In *APS Division of Fluid Dynamics Meeting Abstracts*, volume 1, 1998. 20

L Shao, S Sarkar, and C Pantano. On the relationship between the mean flow and subgrid stresses in large eddy simulation of turbulent shear flows. *Physics of Fluids (1994-present)*, 11(5):1229–1248, 1999. 20

Joseph Smagorinsky. General circulation experiments with the primitive equations: I. the basic experiment*. *Monthly weather review*, 91(3):99–164, 1963. 14, 17, 20

Philippe R Spalart. Direct simulation of a turbulent boundary layer up to r $\theta=$ 1410. *Journal of fluid mechanics*, 187:61–98, 1988. 10

Philippe R Spalart. Strategies for turbulence modelling and simulations. *International Journal of Heat and Fluid Flow*, 21(3):252–263, 2000. 3

Katepalli R Sreenivasan and RA Antonia. The phenomenology of small-scale turbulence. *Annual review of fluid mechanics*, 29(1):435–472, 1997. 49

S Stolz and NA Adams. Large-eddy simulation of high-reynolds-number supersonic boundary layers using the approximate deconvolution model and a rescaling and recycling technique. *Physics of Fluids (1994-present)*, 15(8):2398–2412, 2003. 7

B Mutlu Sumer, Lloyd HC Chua, N-S Cheng, and Jørgen Fredsøe. Influence of turbulence on bed load sediment transport. *Journal of Hydraulic Engineering*, 129(8):585–596, 2003. 32

GR Tabor and MH Baba-Ahmadi. Inlet conditions for large eddy simulation: a review. *Computers & Fluids*, 39(4):553–567, 2010. 4, 24

S Tavoularis, JC Bennett, and S Corrsin. Velocity-derivative skewness in small reynolds number, nearly isotropic turbulence. *Journal of Fluid Mechanics*, 88 (01):63–69, 1978. 24, 48, 133

Hendrik Tennekes and John Leask Lumley. *A first course in turbulence*. MIT press, 1972. 1

PC Valente and JC Vassilicos. The non-equilibrium region of grid-generated decaying turbulence. *Journal of Fluid Mechanics*, 744:5–37, 2014. 91

B Vremen, Bernard Geurts, and Hans Kuerten. Large-eddy simulation of the turbulent mixing layer. *Journal of Fluid Mechanics*, 339:357–390, 1997. 44

David C Wilcox. Reassessment of the scale-determining equation for advanced turbulence models. *AIAA journal*, 26(11):1299–1310, 1988. 16, 58

David C Wilcox. Formulation of the kw turbulence model revisited. *AIAA journal*, 46(11):2823–2838, 2008. 17

David C Wilcox et al. *Turbulence modeling for CFD*, volume 2. DCW industries La Canada, CA, 1998. 16, 17

PK Yeung and SB Pope. Lagrangian statistics from direct numerical simulations of isotropic turbulence. *Journal of Fluid Mechanics*, 207:531–586, 1989. 10